

UNIVERSIDADE FEDERAL DE SÃO CARLOS
CENTRO DE CIÊNCIAS EXATAS E DE TECNOLOGIA
DEPARTAMENTO DE QUÍMICA
PROGRAMA DE PÓS-GRADUAÇÃO EM QUÍMICA

**Modificação das propriedades estruturais,
morfológicas e ópticas do Ag_3PO_4 e $\text{Ag}_2\text{-}$
 $2\text{xZn}_\text{x}\text{WO}_4(0 \leq \text{x} \leq 0.25)$**

Clayane Carvalho dos Santos*

Thesis presented as part of the
requirements to obtain the title of
DOCTOR IN SCIENCES,
concentration area: Inorganic
Chemistry

Advisor: Prof. Dr. Elson Longo

***scholarship: CNPq**

**São Carlos – SP
2019**



UNIVERSIDADE FEDERAL DE SÃO CARLOS

Centro de Ciências Exatas e de Tecnologia
Programa de Pós-Graduação em Química

Folha de Aprovação

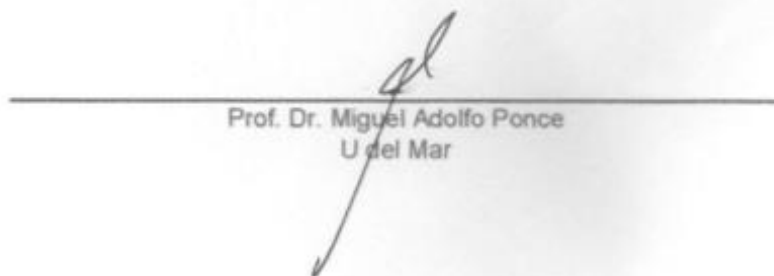
Assinaturas dos membros da comissão examinadora que avaliou e aprovou a Defesa de Tese de Doutorado da candidata Clayane Carvalho dos Santos, realizada em 06/11/2019:


Prof. Dr. Elson Longo da Silva
UFSCar


Profa. Dra. Maria Aparecida Zaghete Bertochi
UNESP


Profa. Dra. Yara Galvão Gobato
UFSCar


Profa. Dra. Adriana de Campos Pastre
UFSCar


Prof. Dr. Miguel Adolfo Ponce
U del Mar

Homenagem Especial

A minha família.

*De todas as palavras existentes no universo
não seriam suficientes para expressar meu amor
e agradecimento. Muito obrigada!*

*“Agradeço todas as dificuldades que enfrentei;
não fosse por elas, eu não teria saído do lugar. As facilidades nos impedem de
caminhar. Mesmo as críticas nos auxiliam muito”*

Por Chico Xavier

AGRADECIMENTOS

Todas as pessoas que passam pelas nossas vidas deixam as suas marcas num ir e vir infinito e com elas aprendemos realmente que fazem a diferença na nossa vida, que nos auxiliam em momentos alegres ou nas maiores dificuldades. Este trabalho é obra de várias mãos, mãos que direta ou indiretamente contribuíram para realização deste.

Os agradecimentos podem ser extensos, mas nunca serão suficientes para expressar toda a minha gratidão a todos àqueles que contribuíram com fé, amizade e amor para que pudesse ser quem sou, a todos vocês, meu sincero obrigado.

Agradeço ilimitadamente, ao meu orientador Prof. Dr. Elson Longo pelos ensinamentos, paciência e amparo na minha trajetória conquistada até hoje. Um exemplo de pessoa e profissional que é para mim.

Agradeço a minha grande família, em especial meus pais, Maria Tereza Carvalho dos Santos e Ademir Costa dos Santos pelo amor, compreensão, fé e apoio incondicional que puseram em mim para chegar até aqui.

Agradeço a todos meus amigos, sem exceção, o qual é difícil enumerá-los, pois não arrisco a esquecer de ninguém, os que estão próximos ou distantes, que demonstraram serem verdadeiros amigos evidenciados pelo companheirismo, respeito e horas descontração, nas mais diversas ocasiões, o meu singelo obrigado.

Agradeço ao Diogenes Saldanha Neto, por todo companheirismo e carinho.

Ao Laboratório Interdisciplinar de Eletroquímica e Cerâmica LIEC/UFSCar, a todos os componentes: técnicos, secretárias, professores e alunos, pelo auxílio nas análises, pela amizade e polidez com que sempre me trataram.

A minha família “Antissociais”, em especial, Domingos Sergio, Dona Ilma, Lucas, Mayara, Manoel e Tayane pela grande amizade, ‘momentos de descontrações’, conselhos, preocupações e acima de tudo muito amor.

A todos os meus professores, que me contribuíram a um nível de maturidade intelectual, e ensinamentos disponibilizados cada um de forma especial para minha formação profissional.

Ao programa de Pós-Graduação em Química da Universidade Federal de São Carlos- PPGQ-UFSCar.

Ao CNPq pelo suporte financeiro concedido durante a realização desta pesquisa.

O presente trabalho foi realizado com apoio da Coordenação de Aperfeiçoamento de Pessoal de Nível Superior – Brasil (CAPES) – Código de financiamento 001.

Ao Instituto Federal de Ciência e Tecnologia do Maranhão, Campus Açailândia, pelo apoio na finalização do doutorado.

E acima de tudo e todos, agradeço a DEUS pela oportunidade de desfrutar a convivência e ao dom da vida.

PUBLICAÇÕES

- **DOS SANTOS, CLAYANE CARVALHO**; ASSIS, M.; MACHADO, THALES RAFAEL; PEREIRA, PAULA F. S.; MINGUEZ; CORDONCILLO, E.; BELTRAN-; DONATE-; ANDRÉS, JUAN; LONGO, ELSON. Proof-of-Concept Studies Directed toward the Formation of Metallic Ag Nanostructures from Ag_3PO_4 Induced by Electron Beam and Femtosecond Laser. *Particle & Particle Systems Characterization*, p. 1800533-9, 2019.
- **DOS SANTOS, CLAYANE CARVALHO**; MOUTA, RODOLPHO; JUNIOR, MANOEL CARVALHO CASTRO; SANTANA, SIRLANE APARECIDA ABREU; SILVA, HILDO ANTONIO DOS SANTOS; BEZERRA, CÍCERO WELLINGTON BRITO. Chitosan-edible oil based materials as upgraded adsorbents for textile dyes. *CARBOHYDRATE POLYMERS*, v. 180, p. 182-191, 2018.
- TRENCH, ALINE BARRIOS; MACHADO, THALES RAFAEL; GOUVEIA, AMANDA FERNANDES; ASSIS, MARCELO; DA TRINDADE, LETÍCIA GUERREIRO; **SANTOS, CLAYANE**; PERRIN, ANDRE; PERRIN, CHRISTIANE; OLIVA, MÓNICA; ANDRÉS, JUAN; LONGO, ELSON. Connecting structural, optical, and electronic properties and photocatalytic activity of $\text{Ag}_3\text{PO}_4:\text{Mo}$ complemented by DFT calculations. *APPLIED CATALYSIS B-ENVIRONMENTAL*, v. 238, p. 198-211, 2018.
- RIBEIRO, GEYSE ADRIANA CORRÊA; SILVA, DOMINGOS SÉRGIO ARAÚJO; **SANTOS, CLAYANE CARVALHO DOS**; VIEIRA, ADRIANA PIRES; BEZERRA, CÍCERO WELLINGTON BRITO; TANAKA, AURO ATSUSHI; SANTANA, SIRLANE APARECIDA ABREU. Removal of Remazol brilliant violet textile dye by adsorption using rice hulls. *Polimeros-Ciencia e Tecnologia*, v. 27, p. 16-26, 2017.
- PEREIRA, PAULA F. S.; **SANTOS, CLAYANE C.**; GOUVEIA, AMANDA F.; FERRER, MATEUS M.; PINATTI, IVO M.; BOTELHO, GLEICE; SAMBRANO, JULIO R.; ROSA, IEDA L. V.; ANDRES, JUAN; LONGO, ELSON. $\text{Ag}_{2-2x}\text{Zn}_x\text{WO}_4$ ($0 \leq x \leq 0.25$) Solid Solutions: Structure, Morphology, and Optical Properties. *INORGANIC CHEMISTRY*, v. 1, p. 1, 2017.
- PENHA, R.S.; **SANTOS, C. C.**; CARDOSO, J. J.F.; SILVA, H. A.S.; SANTANA, S.A. A.; BEZERRA, C. W.B. Chemically Treated Rice Husk as Low-Cost Adsorbent for Metal Ions Uptake (Co and Ni). *Revista Virtual de Química*, v. 8, p. 588-604, 2016.
- **SANTOS, CLAYANE C.**; COSTA, HAWBERTT R.; BEZERRA, CÍCERO W. B. Virtual Journal for Education in Chemistry: Principles and Structure. *Revista Virtual de Química*, v. 7, p. 835-848, 2015.
- HOLANDA, CARLOS ALEXANDRE; SOUZA, JANILSON LIMA; **DOS SANTOS, CLAYANE CARVALHO**; DOS SANTOS SILVA, HILDO ANTONIO; ABREU SANTANA, SIRLANE APARECIDA; COSTA, MARIA CÉLIA PIRES ; SCHULTZ, MARIO SERGIO ; BRITO BEZERRA, CÍCERO WELLINGTON . Remoção do Corante Têxtil Turquesa de Remazol Empregando Aguapé (*Eichhornia crassipes*) como adsorvente. *Orbital: the Electronic Journal of Chemistry*, v. 7, p. 141-154, 2015

LIST OF ABBREVIATIONS

Ag_3PO_4 – Silver phosphate

Ag_2WO_4 – Silver tungstate

CB – Conduction band

CIF – Crystallographic information file

CP – Coprecipitation

DFT – Density functional theory

DOS - Densities of states

E_{gap} – Band gap energy

FE-SEM – Field-emission scanning electron microscopy

FT-IR – Fourier transform infrared

GSAS – General structure analysis system

ICSD – Inorganic crystal structure database

PL – Photoluminescence

TEM - Transmission electron microscopy

UV-Vis – Ultraviolet-visible spectroscopy

VB – Valence band

XPS - X-ray Photoelectron Spectroscopy

XRD – X-ray Diffraction

LIST OF TABLES

Proof of concept studies directed towards the formation of metallic Ag nanostructures from Ag_3PO_4 induced by electron beam and femtosecond laser

Table 1 - Rietveld refinement details obtained for Ag_3PO_4 microcrystals by the increased replacement of the complex cluster in the lattice 14

$\text{Ag}_{2-2x}\text{Zn}_x\text{WO}_4$ ($0 \leq x \leq 0.25$) Solid Solutions: Structure, Morphology and Optical Properties

Table 2 - Atomic Zn Occupation in Sites of $[\text{AgO}_y]$ a Clusters of the $\alpha\text{-Ag}_{2-2x}\text{Zn}_x\text{WO}_4$ b Microcrystals 39

Table 3 - Kinds of clusters present in the models after optimization 40

Table 4 - Optical Band Gap Energy (E_{gap}) Values to $\alpha\text{-Ag}_{2-2x}\text{Zn}_x\text{WO}_4^{\text{a}}$ Microcrystals Obtained by CP Method^b 48

LIST OF FIGURES

Introduction

Figure 1: Crystalline structure of Ag_3PO_4 with rod-ball (a) and polyhedron (b) (red, purple, and blue spheres O represent P, and Ag atoms, respectively). 4

Figure 2: Representation of the unit cell of orthorhombic $\alpha\text{-Ag}_2\text{WO}_4$ 5

Proof of concept studies directed towards the formation of metallic Ag nanostructures from Ag_3PO_4 induced by electron beam and femtosecond laser

Figure 3: A schematic representation of the experimental procedure for femtosecond laser irradiation. 12

Figure 4: XRD patterns of Ag_3PO_4 microcrystals: pure (pAP) electron irradiation (eAP) and femtosecond laser irradiation (IAP)..... 13

Figure 5: Schematic representation of the cubic body centered Ag_3PO_4 structure, illustrating $[\text{AgO}_4]$ and $[\text{PO}_4]$ clusters 15

Figure 6: Micro-Raman of Ag_3PO_4 microcrystals: pure (pAP) electron irradiation (eAP) and femtosecond laser irradiation (IAP)..... 16

Figure 7: XPS survey spectrum of the samples microcrystals (a); High-resolution XPS spectra of Ag3d region of the samples pure (b), electron irradiation (c) and femtosecond laser irradiation (d); and the ratios of peak area attributed to Ag^0 to the total area of all for these samples(e)..... 17

Figure 8: SEM images of Ag_3PO_4 microcrystals: pure (pAP) electron irradiation (eAP) and femtosecond laser irradiation (IAP). The Ag NPs are painted in red color..... 19

Figure 9: TEM of Ag_3PO_4 microcrystals: pure (pAP) electron irradiation (eAP) and femtosecond laser irradiation (IAP)..... 20

Figure 10: TEM micrographs at higher magnification of individual crystallites with: a) electron irradiation and b) femtosecond laser irradiation 21

Figure 11: Distribution the particles of Ag^0 at the Ag_3PO_4 microcrystals with: a) electron irradiation and b) femtosecond laser irradiation 22

Figure 12: Schematic illustration of the proposed growth mechanism for the formation of metallic Ag on Ag_3PO_4 microcrystals: (A) surface interaction and (B) Coulomb explosion..... 23

$\text{Ag}_{2-2x}\text{Zn}_x\text{WO}_4$ ($0 \leq x \leq 0.25$) Solid Solutions: Structure, Morphology and Optical Properties

Figure 13: XRD of the $\alpha\text{-Ag}_{2-2x}\text{Zn}_x\text{WO}_4$ (where $x =$ (a) 0, (b) 0.05, (c) 0.10, (d) 0.15, e) 0.20, and (f) 0.25) microcrystals obtained by the CP method at 80°C for 30 min. 35

Figure 14: Schematic representation of crystalline units cells of $\alpha\text{-Ag}_{2-2x}\text{Zn}_x\text{WO}_4$ ($x = 0.25$) microcrystals. 38

Figure 15: (a) Raman spectra of the $\alpha\text{-Ag}_{2-2x}\text{Zn}_x\text{WO}_4$ ($x =$ (a) 0, (b) 0.05, (c) 0.10, (d) 0.15, (e)

0.20, and (f) 0.25) microcrystals obtained by the CP method at 80 °C for 30 min and (b) comparison between the relative positions of theoretical and experimental Raman-active modes of $\alpha\text{-Ag}_{2-2x}\text{Zn}_x\text{WO}_4$ microcrystals	41
Figure 16: FE-SEM images of $\alpha\text{-Ag}_{2-2x}\text{Zn}_x\text{WO}_4$ (where (A–C) $x = 0$, (D–F) $x = 0.05$, (G–I) $x = 0.10$, (J–L) $x = 0.15$, (M–O) $x = 0.20$, and (P–R) $x = 0.25$) microcrystals, obtained by the CP method at 80 °C for 30 min.....	44
Figure 17: Schematic illustration of the proposed growth mechanism leading to the formation of $\alpha\text{-Ag}_{2-2x}\text{Zn}_x\text{WO}_4$ ($0 \leq x \leq 0.25$) microcrystals	47
Figure 18: Band structure of (a) pure $\alpha\text{-Ag}_2\text{WO}_4$, (b) model A, and (c) model B	49
Figure 19: DOS projected in (a) pure $\alpha\text{-Ag}_2\text{WO}_4$, (b) model A, and (c) model B.	51
Figure 20: Emission spectra of the $\alpha\text{-Ag}_{2-2x}\text{Zn}_x\text{WO}_4$ ($x =$ (a) 0, (b) 0.05, (c) 0.10, (d) 0.15, (e) 0.20, and (f) 0.25) microcrystals obtained by the CP method at 80 °C for 30 min; excited at 350.7 nm with a krypton ion laser	52
Figure 21: Deconvolution of PL spectra of $\alpha\text{-Ag}_{2-2x}\text{Zn}_x\text{WO}_4$ ($x =$ (a) 0, (b) 0.05, (c) 0.10, (d) 0.15, (e) 0.20, and (f) 0.25) microcrystals obtained by the CP method at 80 °C for 30 min. (insets) The area percentage of each color component corresponding to the emiss peak.....	54

RESUMO

MODIFICAÇÃO DAS PROPRIEDADES ESTRUTURAIS, MORFOLÓGICAS E ÓPTICAS DO Ag_3PO_4 e $\text{Ag}_{2-2x}\text{Zn}_x\text{WO}_4$ ($0 \leq x \leq 0.25$).

Os fosfatos e os tungstatos são compostos importantes e conhecidos principalmente por suas propriedades fotocatalíticas e fotoluminescentes. O presente trabalho propõe-se um estudo das propriedades estruturais, morfológicas e ópticas dos materiais: i) Ag_3PO_4 irradiado por feixe de elétrons e laser de femtosegundos, e $\text{Ag}_{2-2x}\text{Zn}_x\text{WO}_4$ ($0 \leq x \leq 0.25$) modificado com diferentes concentrações de Zn^{2+} obtidos pelo método de coprecipitação. As fases obtidas foram caracterizadas por difração de raios-X, espectroscopia de espalhamento Raman, espectroscopia de fotoelétrons por raios X, microscopia eletrônica de varredura e transmissão e por medidas de fotoluminescência. Os principais resultados investigados para os cristais de Ag_3PO_4 irradiados mostra que dados de difração de XRD apontam padrões semelhantes para o as amostras não irradiadas e irradiadas por elétrons, enquanto a amostra irradiada por laser de femtosegundos apresenta padrão de XRD mais baixa, mostrando um distúrbio estrutural mais alto a longo alcance. Para os Espectros Raman e Rietveld mostram que ambos $[\text{PO}_4]$ e $[\text{AgO}_4]$ são aglomerados distorcidos, sendo as ligações Ag-O de aglomerados $[\text{AgO}_4]$ mais lábeis que as ligações P-O de aglomerados $[\text{PO}_4]$. Além disso, foi observado mecanismo distinto de crescimento e tamanho na produção de Ag metálica. Para o Ag_2WO_4 , os resultados mostraram que o aumento da concentração de Zn nos microcristais na matriz hospedeira de $\alpha\text{-Ag}_2\text{WO}_4$ causou uma transformação morfológica e um deslocamento das propriedades ópticas. E em relação as propriedades fotoluminescentes dos microcristais $\alpha\text{-Ag}_2\text{WO}_4$ e $\alpha\text{-Ag}_{2-2x}\text{Zn}_x\text{WO}_4$ são explicadas por meio de efeitos de distorções e vacâncias de oxigênio (V_{O^x}) em clusters $[\text{WO}_6]$ e $[\text{AgO}_y]$ ($y = 2, 4, 6$ e 7) respectivamente causando um desvio para região do vermelho.

Palavras-chave: Fosfatos, tungstatos, irradiação, ópticas

ABSTRACT

MODIFICATION OF STRUCTURAL, MORPHOLOGICAL AND OPTICAL PROPERTIES OF Ag_3PO_4 e $\text{Ag}_{2-2x}\text{Zn}_x\text{WO}_4$ ($0 \leq x \leq 0.25$)

Phosphates and tungstates are important compounds and known mainly for their photocatalytic and photoluminescent properties. The present work proposes a study of the structural, morphological and photoluminescent properties of the materials: Ag_3PO_4 electron beam irradiated and femtosecond laser, and $\text{Ag}_{2-2x}\text{Zn}_x\text{WO}_4$ ($0 \leq x \leq 0.25$) modified with different concentrations of Zn^{2+} obtained by the method of co-precipitation. The obtained phases were characterized by X-ray diffraction, Raman scattering spectroscopy, X-ray photoelectron spectroscopy, scanning and transmission electron microscopy, and photoluminescence measurements. The main results investigated for the irradiated Ag_3PO_4 crystals show that XRD diffraction data show that the patterns for the non-irradiated and similar electron-irradiated samples, while the femtosecond laser-irradiated sample has a higher resolution XRD pattern, low, showing a higher structural disturbance at long range. For the Raman and Rietveld Spectra they show that both $[\text{PO}_4]$ and $[\text{AgO}_4]$ are distorted clusters, being the Ag-O bonds of agglomerates $[\text{AgO}_4]$ more labile than the P-O bonds of clusters $[\text{PO}_4]$. In addition, a distinct growth and size mechanism was observed in the production of metallic Ag. For Ag_2WO_4 , the results showed that the increase of Zn concentration in the microcrystals in the $\alpha\text{-Ag}_2\text{WO}_4$ host matrix caused a morphological transformation and a shift of the electronic and optical properties. And regarding the photoluminescent properties of the $\alpha\text{-Ag}_2\text{WO}_4$ and $\alpha\text{-Ag}_{2-2x}\text{Zn}_x\text{WO}_4$ microcrystals are explained by the effects of distortions and oxygen vacancies ($\text{V}_{\text{O}^{\times}}$) on clusters $[\text{WO}_6]$ and $[\text{AgO}_y]$ ($y = 2, 4, 6$ and 7) respectively causing a redshift.

Key-word: Phosphate, tungstates, irradiation, optical

SUMMARY

1. INTRODUCTION.....	1
1.1 Studied Inorganic materials	2
1.1.1 Silver Phosphate (Ag_3PO_4).....	2
1.1.2 Silver Tungstate (Ag_2WO_4).....	5
2. GOALS	7
3. PUBLISHED ARTICLES.....	8
3.1 Proof of concept studies directed towards the formation of metallic Ag nanostructures from Ag_3PO_4 induced by electron beam and femtosecond laser.	8
3.2 $\text{Ag}_{2-2x}\text{Zn}_x\text{WO}_4$ ($0 \leq x \leq 0.25$) Solid Solutions: Structure, Morphology and Optical Properties.....	30
4. FINAL CONSIDERATION.....	76
5. FUTURE PERSPECTIVE.....	76
GENERAL BIBLIOGRAPHY.....	76

1. INTRODUCTION

In recent decades, the search for new materials with specific properties has aroused great interest of researchers, thanks to the great scientific value of these materials. This way, many methods and synthetic routes are used to obtain and / or modify materials that have been extensively studied in order to intensify their properties. These properties are influenced by several factors such as chemical composition, particle size, surface structure, material morphology, doping addition, etc. [1-6].

Potentialize these properties is of paramount importance to large companies, especially in the area of electronics, due to the growing demand to generate new technologies and thus increase the efficiency of devices or equipment that can supply the needs of modern society.

The preparation of materials by new routes may lead to the discovery of distinct morphological characteristics, that may interact and change the properties of these materials, as new chemical preparation and processing routes may result in a reduction in temperature and processing time when, compared to other conventional methods [6,7].

To obtain materials, their syntheses, usually involve heat treatments at elevated temperatures. One of the possibilities that can be used is the solution synthesis route, which has been shown to be a suitable way to manufacture advanced materials with desired shapes and sizes [8]. Thus, the coprecipitation method has been shown to be a potentially attractive route for the production of ceramic powders [9]. In recent years the coprecipitation process for the synthesis of materials has attracted attention mainly due to fast synthesis, low energy consumption, low cost, low environmental impact, high yield of nanoparticles and so on.

In this context, semiconductor materials present themselves as a possibility of modification, due to their properties, the most common indications: magnetic, [7-8] bactericidal, [9] catalytic [10-11], luminescent, [12-13] antimicrobial [14] among others, and specific characteristics. In addition, its use is related to biotechnological and environmental advantages. [15-19].

The use of these materials has grown surprisingly in an infinity of

applications in diverse areas of human knowledge. This growth is the result of advances in scientific and technological knowledge in the field of materials science and engineering, in recent decades. As is known, semiconductors are, from an electronic point of view, materials that have intermediate conducting properties between insulating materials and conductors.

Among the semiconductors, the highlighted, in this study, are silver phosphates and silver tungstates, as they have interesting properties, such as catalytic, sensor, photoluminescent and so on, enabling their application in various areas

Thus, researches on these semiconductors are increasing [13-15], the prominence given to these materials has been directly confirmed by the large number of publications, according to the *science direct* database, the number of publications related to silver phosphate and silver tungstate were 1,835 articles in 2000 and 4,975 per year by 2019.

Although there is already a lot of research on the use of phosphate and silver tungstate materials, much still needs to be studied, especially in relation to their interaction with other materials and modification of their surface.

Because of this and the importance of the subject exposed, this research aims to modify the compounds Ag_3PO_4 and Ag_2WO_4 , allowing these materials to become even more attractive from the point of view of application, improving their properties.

1.1 Studied Inorganic materials

1.1.1 Silver Phosphate (Ag_3PO_4)

Inorganic materials have important and numerous applications in modern technology, according to their composition, structure and physicochemical properties. Among these materials we can highlight phosphates, as they are easily obtained and have unique properties. Phosphates are found in large quantities in nature, both in the form of minerals and biomaterials, and are an excellent source of inorganic materials due to some characteristics, such as (i) they exist in the form of monomers, oligomers and polymers chain open or closed; (ii) they form a big variety of gels, crystalline solids, and glassy solids that are resistant to crystallization; (iii) are

constituents of living organisms, being devoid of intrinsic toxicity.

Phosphates are characterized by P-O bonds, that is, bonds between oxygen atoms (O) and phosphorus (P), where the phosphorus atom is tetrahedrally coordinated by four oxygens, which means that the basic phosphate-forming units are PO_4 tetrahedra. These result from the formation of sp^3 hybrid orbitals through four oxygens from the phosphorus's outer five electrons ($3\text{s}^23\text{p}^3$), and the fifth phosphorus external electron is promoted to a 3d orbital where a π bond is formed ($\text{P}=\text{O}$) with 2p electrons of a terminal oxygen [7-10].

Phosphates are classified into three types: Orthophosphates, pyrophosphates and metaphosphates.

Orthophosphates are compounds containing PO_4^{3-} ions. Pyrophosphates and metaphosphates are known as condensed phosphates, formed by the repeated condensation (polymerization) of tetrahedral units $[\text{PO}_4]$, resulting in three-dimensional chains of PO_4 tetrahedral, with each tetrahedron bonding to the next, sharing the oxygen atom of one or two vertices. The term metaphosphate refers to cyclically structured anions that have the exact composition $(\text{PO}_3)_n^{n-}$ [10].

Condensed phosphates can be divided into three categories: linear polyphosphates whose formation unit is the PO_4^{3-} orthophosphate ion and the chains have the composition $[(\text{PO}_3)_{n-1}\text{PO}_4]^{-(n+2)}$, metaphosphates (cyclophosphates) which are compounded with ring-shaped chains and each ring-shaped anion has an exact composition $(\text{PO}_3)_n^{n-}$, and ultraphosphates (3D structures) that are chains that connect to each other by sharing up to three oxygens from vertices of a single tetrahedron (PO_4) forming 3D structures without any linear or cyclic symmetry as previously mentioned in the case of polysphosphates and metaphosphates. Due to its easy obtaining and cost, orthophosphate was chosen for this research [7,13].

Among the phosphates, silver phosphate (Ag_3PO_4) is well known because of the importance of these materials. Special emphasis has been given to silver phosphate ceramics because of their simpler structures, low cost, and easy getting, compared to other phosphates.

Ag_3PO_4 has a crystalline cubic centered body structure with $P43n$ space groups [16]. With a network parameter of approximately 6.004 Å [13]. The structure consists of tetrahedral clusters of $[\text{PO}_4]$ and $[\text{AgO}_4]$. Each isolated cluster of $[\text{PO}_4]$ is linked to three neighboring clusters of $[\text{AgO}_4]$ by oxygen atoms. $[\text{AgO}_4]$ clusters are highly distorted in the network, because of the inductive effect caused by the highly electronegative cluster of $[\text{PO}_4]$ [17-19]. Figure 1 illustrates the tetrahedral crystal

structure of Ag_3PO_4 [14].

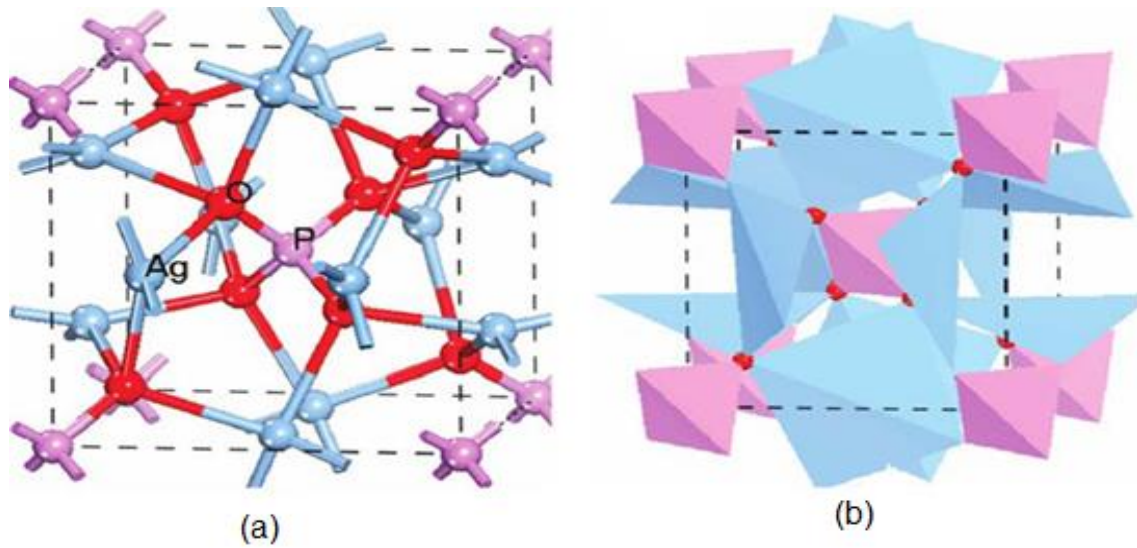


Figure 1: Crystalline structure of Ag_3PO_4 with rod-ball (a) and polyhedron (b) (red, purple, and blue spheres O represent P, and Ag atoms, respectively).

For Heterostructured compounds, the Ag_3PO_4 , may be formed with other materials (ZnO [20] TiO_2 [21] Ag [22-23] Fe_2O_3 [24] $\text{AgX}/\text{Ag}_3\text{PO}_4$ ($X = \text{Cl}, \text{Br}, \text{I}$), [25-26] C_3N_4 [27] and $\text{Ag}/\text{Ag}_3\text{PO}_4/\text{Bi}_2\text{MoO}_6$ [28]) in order to improve its physicochemical properties.

In particular, the synthesis of silver phosphate particles has been extensively reported [29-31]. Botelho *et al* [7] used silver phosphate in optical and photoluminescent properties and present interesting results as the formation of irregular spherical microparticles containing metallic Ag on the surface which directly influences photoluminescence.

According to studies by Zhang *et al* [15] they sought to understand the behavior of Ag_3PO_4 at different temperatures and morphology using various phosphate precursors, in which they studied the photocatalytic behavior of Ag_3PO_4 with carbon nanotubes at different temperatures and time and observed that there wasn't a significant difference in the photocatalytic process.

Another study is by Trench and contributors *et al* [32], in the study of the semiconductor Ag_3PO_4 , doped with different Mo^{6+} concentrations, was inserted into the crystal structure in the form of doping and they observed a significant improvement in the photocatalytic process of doped materials compared to pure material, being the material doped by 0.5% Mo presented better results for Rhodamine B degradation

1.1.2 Silver Tungstate (Ag_2WO_4)

Transition metal tungstates form an important class of functional materials because they possess a combination of covalent, ionic and metallic bonding which render them important physical and chemical properties allowing a series of applications as in photoluminescence, photochromism, production of scintillation materials, sensors, antimicrobial agent, solid-state lasers and catalysts [10,14,16].

Metallic tungstates are a group of multifunctional advanced ceramics, which are classified as complex oxides, with general chemical formula of type AWO_4 or A_2WO_4 where A represents the divalent or monovalent cation, respectively. Depending on the size of the cation, divalent tungstates (AWO_4) present specific crystalline structures, when the ionic radius of $A \leq 0.77\text{\AA}$ ($A = \text{Fe}, \text{Mn}, \text{Co}, \text{Ni}, \text{Mg}, \text{Zn}$) tungstates crystallize with monoclinic structure of the type wolframite, with space groups $P2/c$ and two units of formula in each unit cell, if the cations have an ionic radius $> 0.77\text{\AA}$, the tungstates crystallize with tetragonal schelite structure [33-35].

Among the tungstates, silver tungstate, Ag_2WO_4 , is highlighted in this study. In which it belongs to the family of tungstates with general formula is A_2BO_4 , and has various structures, such as α -orthorhombic, β -hexagonal and γ cubic, which are dependent on the reaction medium conditions (reaction medium temperature and pH) [36,37]. The most stable phase at room temperature is the α orthorhombic with space group $Pn2n$.

Figure 2 illustrates the crystalline structure of the α -orthorhombic phase constructed from the tungsten and silver sites [37].

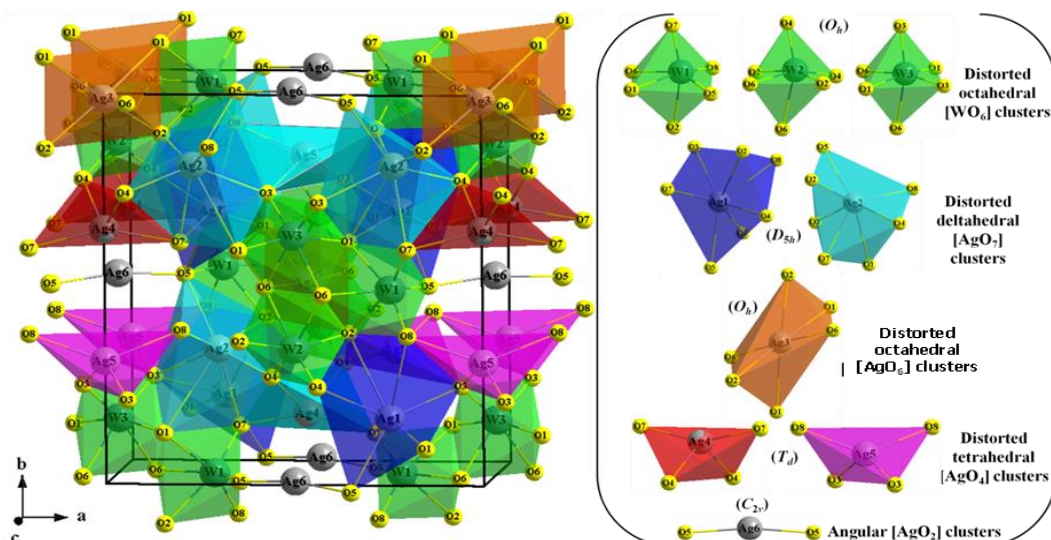


Figure 2: Representation of the unit cell of orthorhombic α - Ag_2WO_4

In the α -orthorhombic structure, site B is occupied by the tungsten atom (W) being coordinated by six oxygen atoms forming octahedral clusters $[\text{WO}_6]$ with different degrees of distortion. Site A is occupied by the silver atom (Ag) and may exhibit four types of different coordinations, forming distorted deltahedral clusters $[\text{AgO}_7]$, distorted octahedral clusters $[\text{AgO}_6]$, tetrahedral clusters $[\text{AgO}_4]$ and angular clusters $[\text{AgO}_2]$.

$\alpha\text{-Ag}_2\text{WO}_4$ has properties that may be linked to interactions between $[\text{WO}_6]$ octahedra and $[\text{AgO}_x]$ clusters ($x = 2, 4, 6, \text{ and } 7$) [33]. These properties are related to electronic and structural disorder, since the nature and interaction between the clusters of $[\text{WO}_6]$ and $[\text{AgO}_x]$ causes the formation of a flexible open-structure material, and the bonds (O-Ag-O and O-W-O) in the clusters have a weak interaction between unit cells being able to be chemically modified using electron irradiation [38].

Recently, an article has been published demonstrating the cytotoxic activity of silver tungstate against Gram positive and Gram negative [39] pathogenic bacteria. Longo et al., [40] demonstrated cytotoxic or antimicrobial effect of silver tungstate against strains of *Staphylococcus aureus*, methicillin-resistant, one of today's most potent antimicrobial drugs, and a 32-fold greater bactericidal action was observed when compared to silver tungstate under normal conditions, due to the observed improvement of some properties due to the effects caused by the reduction of material size.

Cavalcante et al. [41] observed photoluminescence in $\alpha\text{-Ag}_2\text{WO}_4$ prepared by different methods, coprecipitation, sonochemical and conventional hydrothermal. The sonochemical method showed the best photoluminescence result at room temperature with a maximum emission at 575 nm, yellow region of the visible spectrum. According to these authors, a smaller dispersion in the average crystal size and the presence of intermediate energy levels promoted the electronic transition between clusters $[\text{WO}_6]_o$ and $[\text{WO}_6]_d$ with medium-range structural order-disorder.

Longo *et al.*, [35] investigated the Mo^{6+} doped $\alpha\text{-Ag}_2\text{WO}_4$ microcrystals at different concentrations by the co-precipitation method. Given the main results, there was a rapid growth of silver nanoparticles on the material surface during exposure to the accelerated electron beam under 10 keV in the scanning electron microscope. The samples also presented ohmic behavior with resistance of the order of $10\Omega \cdot \text{m}$, with pure $\alpha\text{-Ag}_2\text{WO}_4$ crystals, exhibiting strong photoluminescence in the red region

that is reduced with doping and without considerable band gap variation as a function of Mo^{6+} concentration.

This work is to obtain and characterize the Ag_3PO_4 and $\text{Ag}_{2-2x}\text{Zn}_x\text{WO}_4$ ($0 \leq x \leq 0.25$) crystals, and to investigate structural, morphological and optical properties, as well as: To obtain Ag_3PO_4 and $\text{Ag}_{2-2x}\text{Zn}_x\text{WO}_4$ ($0 \leq x \leq 0.25$) crystals by coprecipitation method; To investigate the structural and morphological properties of the materials; To study the influence of electron beam and femtosecond laser irradiation on surface of Ag_3PO_4 ; To observe the growth of silver nanoparticles on the surface of the Ag_3PO_4 ; To investigate the photoluminescent properties of $\text{Ag}_{2-2x}\text{Zn}_x\text{WO}_4$ ($0 \leq x \leq 0.25$).

3. PUBLISHED ARTICLES

3.1 Proof of concept studies directed towards the formation of metallic Ag nanostructures from Ag_3PO_4 induced by electron beam and femtosecond laser.

3.1.1 Abstract

In this work, for the first time, the instantaneous nucleation and growth processes of Ag nanoparticles on Ag_3PO_4 mediated by femtosecond laser pulses are reported and analyzed. The investigated samples were pure Ag_3PO_4 sample, electron irradiated Ag_3PO_4 sample, and laser irradiated sample. Complete characterization of the samples is performed using X-ray diffraction (XRD), Rietveld refinements, field emission scanning electron microscopy, and energy dispersive spectroscopy (EDS). XRD confirmed that the irradiated surface layer remains crystalline, and according to EDS analysis, the surface particles are composed primarily of Ag nanoparticles. This method not only offers a one-step route to synthesize Ag nanoparticles using laser-assisted irradiation with particle size control, but also reports a complex process involving the formation and subsequent growth of Ag nanoparticles through an unexpected additive-free in situ fabrication process.

3.1.2 Introduction

The properties derived from the interaction of electrons/waves with matter have a key role in modern science and engineering. Energetic particle and/or electromagnetic interactions with solid materials have been studied for several decades, and the characterization of structure or property responses to these stimuli from the surrounding environment at the atomic scale have a key role in the understanding and rationalization of the structure–property–function relationship [1–2]. Electron microscopy and laser techniques are based on these interactions. Further, the analysis of the scattered electrons and radiation after propagation through a specimen provides information regarding the structural and electronic properties of the sample. Conventional microstructure characterization of nanomaterials relies heavily on electron microscopy, where high-energy electrons transmit through the specimen and provide

useful information at the nanometer and sub-nanometer levels of the samples based on a variety of electron-solid interactions. In the past decade, the advancement of technology associated with transmission electron microscopy has enabled direct observations of the growth process of nanostructured materials at high spatial and temporal resolutions [2–4]. The interaction of femtosecond (fs) laser radiation with matter has been extensively studied and practically utilized for surface manipulation at the micro and nanoscale levels, having a critical role in material processing at the micro–nano-scale [5–13]. In this context, Tan et al. [14] presented a critical overview of the current state of the art in studying different fs laser-induced phenomena in transparent materials including their physical and chemical mechanisms, applications and limitations, and future research trends. Although, these topics attract significant interest and demonstrate considerable potential for many applications, the phenomenology of these processes is complicated. Moreover, fundamental questions concerning the corresponding mechanisms continue to be debated and must be studied in detail.

Our research group, using a joint combination of experimental and theoretical studies, has conducted studies for understanding the formation mechanism of Ag nanoparticles (NPs) [15–16] provoked by the exposure to electron beams of an electronic microscope on the surfaces of several Ag-based materials such as α -Ag₂WO₄ [17–23], β -Ag₂WO₄ [24–25], γ -Ag₂WO₄ [26], β -Ag₂MoO₄ [27–28], Ag₂CrO₄ [29], AgVO₃ [30], Ag₂V₂O₇ [31] and Ag₃PO₄ crystals [32]. Furthermore, we have reported four new phenomena provoked by fs laser irradiation: i) the scale-up of the formation of Ag NPs on α -Ag₂WO₄ with bactericidal properties [17]; ii) the synthesis of metallic Bi NPs with coexisting crystallographic structures (rhombohedral, monoclinic, and cubic) on NaBiO₃ [33]; iii) the formation of in NPs on InP [34]; and iv) the synthesis of Ag–Bi nanoalloys from inorganic oxide Ag₂WO₄ and NaBiO₃ target [35]. Both fs and electron beam irradiation strategies allow us to obtain Ag NPs with interesting technological applications such as photoluminescent and bactericide materials.

A hybrid heterostructure formed by Ag NPs and Ag₃PO₄, Ag/Ag₃PO₄, was previously successfully synthesized and its application as a highly efficient and stable plasmonic photocatalyst validated [36–42]. In this context, recently we reported and analyzed the formation of Ag nanostructures on Ag₃PO₄ induced by electron beam irradiation [32]. Herein, inspired and as a continuation of these previous works, we

report a systemic investigation of this phenomena and demonstrate a growth of Ag NPs on a surface of Ag_3PO_4 induced by fs laser irradiation. The focus of this paper is three-fold: i) to report, for first time, the instantaneous nucleation and growth processes of Ag NPs on Ag_3PO_4 mediated by fs laser pulses; ii) to investigate samples that were pure Ag_3PO_4 (pAP), electron irradiated Ag_3PO_4 (eAP), and laser irradiated (IAP), iii) to compare this phenomena with previous observations where these processes that occur on Ag_3PO_4 are driven by an accelerated electron beam from an electronic microscope under high vacuum, and iv) to gain an improved understanding of this phenomenon and allow a finer control to future technological applications. Experimental techniques such as energy-dispersive X-ray spectroscopy (EDS) and transmission electron microscopy (TEM) with a high-angle annular dark field (HAADF) provide a valuable probe into the relationship between atomic-scale structural and electronic perturbations produced by fs laser pulses and electron beam material modification.

3.1.2 Experimental details

3.1.2.1 Synthesis of Ag_3PO_4 crystals

Synthesis: Synthesis of Ag_3PO_4 microcrystals: The methodology employed for the synthesis of the Ag_3PO_4 microcrystals was a simple chemical precipitation at room temperature, as described in detail previously [32]. Briefly, 75 mL of an aqueous solution containing 3 mmol of AgNO_3 (99.8%, Vetec) and 25 mL of an aqueous solution containing 1 mmol of NaH_2PO_4 (98.6%, J. T. Baker) were prepared. Both solutions were quickly mixed in constant agitation, promoting the instantaneous formation of yellow Ag_3PO_4 precipitate. The mixture was then stirred for 10 min. The precipitates obtained were washed several times with deionized water and centrifuged to remove the by-products formed during the reaction. The resulting powder was dried at 60 °C for several hours under air atmosphere. The sample obtained in this procedure is referred to as the pAP.

Electron beam irradiation of Ag_3PO_4 : A Carl Zeiss DSM940A scanning electron microscope (Germany) with an accelerating voltage of 30 kV was used to irradiate the sample with electrons. In this procedure, the pAP powder was placed in a

cylindrical sample holder. The electron beam exposure time was fixed at 5 min. The sample obtained here is referred to as the eAP.

Femtosecond laser irradiation of Ag_3PO_4 : The fs laser irradiation scheme is displayed in figure 3. The pure Ag_3PO_4 (pAP) sample was irradiated with a Ti:sapphire laser (Femtopower Compact Pro, Femto Lasers) emitting 30 fs pulses, FWHM, with a central wavelength of 800 nm and a repetition rate of 1 kHz. An iris was used to obtain a 6 mm laser beam that was focused on the surface of a powder target of Ag_3PO_4 using a 75 mm lens which allows to obtain a focal spot in the processing plane with a diameter of about 21 μm FWHM. The pAP sample was placed at the bottom of a quartz cuvette attached to a two-dimensional motion-controlled stage moving at a constant speed of 0.5mm/s. To ensure that the laser interacted with the entire sample, the irradiation process was repeated four times after stirring the sample each time. A mean power of 10, 80 and 200 Mw, was used to irradiate the sample. These provides a fluence over the sample of about 3, 24 and 60 J/cm^2 , respectively. Experimentally, we observed that the results of the synthesized nanoparticles with these different laser parameters were similar. Previously, we show that the optimal conditions for the irradiation of semiconductors by femtosecond lasers result when the sample is irradiated with a mean power of 200 mW [17,33]. Finally, to ensure that the pulse duration of the laser at the focal plane was 30 fs, a user-adjustable post-compression stage based on a pair of fused silica Brewster prisms was employed to compensate for the dispersion in the beam delivery path. The sample obtained in this procedure is referred to as the fs IAP. Although for comparison with our previous papers we employ a femtosecond laser [17,33-35], further studies can be conducted in order to elucidate if it is possible the formation of metallic Ag fby irradiation of pAP with other kind of lasers, as it happens in other Ag-containing compounds [64,65].

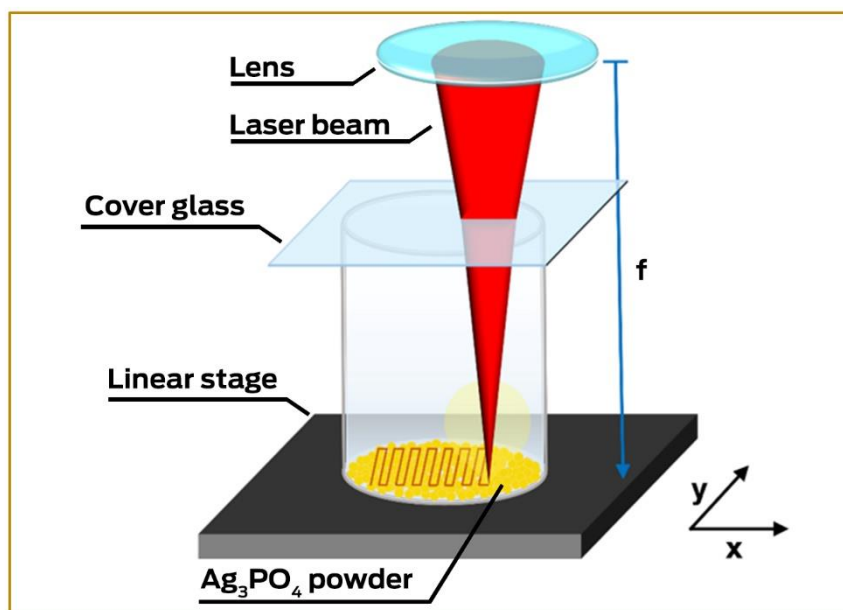


Figure 3: A schematic representation of the experimental procedure for femtosecond laser irradiation.

3.1.2.2 Characterization of Ag_3PO_4 crystals

The pAP, eAP, and IAP samples were structurally characterized by powder XRD using a Rigaku D/Max-2500PC diffractometer (Japan) with Cu-K α radiation ($\lambda = 0.15406$ nm). Data were collected in a 2θ range of $10\text{--}110^\circ$ using a step scan rate and step size of $1^\circ/\text{min}$ and 0.02° . Raman spectroscopy was performed using a Horiba Jobin-Yvon IHR550 (Japan) spectrometer coupled to a CCD detector and a Melles Griot, United States laser (USA), operated at 633 nm. XPS was performed using a Scienta Omicron ESCA+ spectrometer with a high-performance hemispheric analyzer (EA 125) with monochromatic Al K α ($h\nu = 1486.6$ eV) radiation as the excitation source. The operating pressure in the ultrahigh vacuum chamber (UHV) during analysis was 2×10^{-9} mbar. Energy steps of 50 and 20 eV were used for the survey and high-resolution spectra, respectively. The binding energies of all elements were calibrated by referencing to the C 1s peak at 284.8 eV.

The morphological features of Ag_3PO_4 microparticles and the effect of electron beam and fs laser exposure on the growth mechanisms of metallic Ag NPs was first examined by field emission scanning electron microscopy (FE-SEM) with a Carl Zeiss Supra 35VP (Germany) microscope operating at 5 kV. In this procedure, the micrographs were recorded as soon as possible to avoid influence of the electron

beam during the FE-SEM characterization of the prepared samples. TEM and high-resolution TEM (HRTEM) micrographs, as well as EDS analysis were performed with an FEI TECNAI F20 (Netherlands) microscope operating at 200 kV. HAADF image and EDS mapping were recorded in scanning transmission mode. The samples were prepared by depositing small amounts of the powders directly onto holed carbon-coated Cu grids to capture information regarding the nucleation and growth mechanisms of the metallic Ag.

3.1.3 Results and discussion

3.1.3.1 XRD analysis

Figure 4 displays the X-ray diffraction (XRD) patterns of the prepared samples. The diffraction peaks are all in agreement with the results reported in Inorganic Crystal Structure Data (ICSD) No. 1530, which are related to Ag_3PO_4 phase with a body-centered cubic structure (space group P-43n) [32,44]. No secondary phases were observed, even after the electron or laser irradiation. The narrow profiles of the diffraction peaks are related to a long-range structural ordering in these samples.

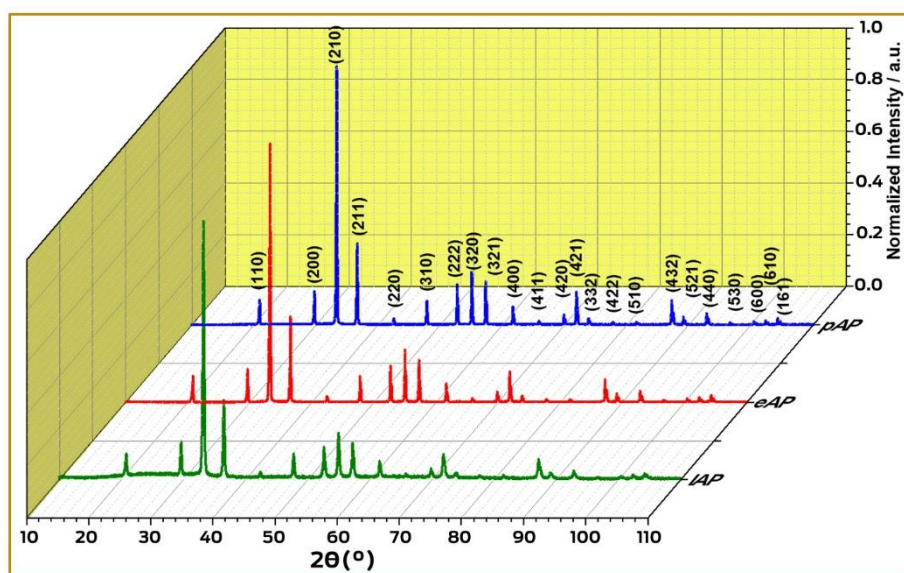


Figure 4: XRD patterns of Ag_3PO_4 microcrystals: pure (pAP) electron irradiation (eAP) and femtosecond laser irradiation (IAP)

The pAP and eAP XRD patterns are similar; the principal differences are observed in the IAP sample. In this specific case, the XRD pattern is less resolved and certain diffraction peaks no longer appear, such as the ones referred to as the (220),

(411), (332), (422), and (510) peaks. Thus, in the IAP sample, laser irradiation induces a higher structural disorder at the long-range of the Ag_3PO_4 crystalline structure. An analysis of the full width at half maximum (FWHM) of the most intense peak of the XRD patterns related to plane (210) was performed to understand the degree of order/disorder among the samples at long range. The pAP sample had an FWHM of approximately 0.07° , causing this value to increase with different types of irradiation; the value was 0.016° for eAP and 0.025° for IAP. It was determined that when Ag_3PO_4 is subjected to fs laser/electron beam irradiation, a higher degree of disorder is added to the new material, caused by distortions in the crystal lattice of the Ag_3PO_4 .

3.1.3.2 Rietveld refinement analysis

Rietveld refinements [45] were employed to understand the differences in the structural arrangements of the prepared samples. In this work, the refinements were performed through the general structure analysis program (GSAS)[46], assuming the spatial groups P-43n for the cubic structure of the centered body of Ag_3PO_4 and adjusted to ICSD No. 1530[32]. The plots of the refinements in figure S1 in the supplementary material are in perfect agreement with the XRD patterns presented in Figure 4.

The lists the fitting parameters (R_{wp} , R_p , R_{bragg} , χ^2), which revealed an acceptable adjust between the theoretical and observed XRD patterns. The results obtained from the refinement revealed similar lattice parameters for all samples as indicated in Table 1.

Table 1 - Rietveld refinement details obtained for Ag_3PO_4 microcrystals by the increased replacement of the complex cluster in the lattice

Samples Ag_3PO_4	Lattice Parameters			Cell volume (\AA^3)	R_{Bragg} (%)	χ^2 (%)	R_{wp} (%)	R_p (%)
	$\alpha = \beta = \gamma = 90^\circ$							
	a (\AA)	b (\AA)	c (\AA)					
pAP	6.015(66)	6.015(66)	6.015(66)	217.96(6)	0.0580	1.550	0.075	0.054
eAP	6.016(13)	6.016(13)	6.016(13)	217.74(7)	0.0582	2.020	0.081	0.059
IAP	6.013(54)	6.016(13)	6.016(13)	217.46(6)	0.0731	1.400	0.073	0.061
Ag_3PO_4 (ICSD 1530)	6.004(2)	6.004(2)	6.004(2)	216.43	-	-	-	-

However, the volume of the unit cell linearly decreases from the

microcrystalline pAP and eAP, and thereafter from the IAP, where the results indicate a small degree of distortion in the short distance for the tetrahedral $[\text{AgO}_4]$ cluster with values of 93.54° , 93.61° , and 93.69° , respectively. This could be because the structure underwent a process of cell contraction, possibly forming a high density of Ag vacancies (VAg). The schematic representation of the unit cell of cubic IAP is illustrated in figure 5.

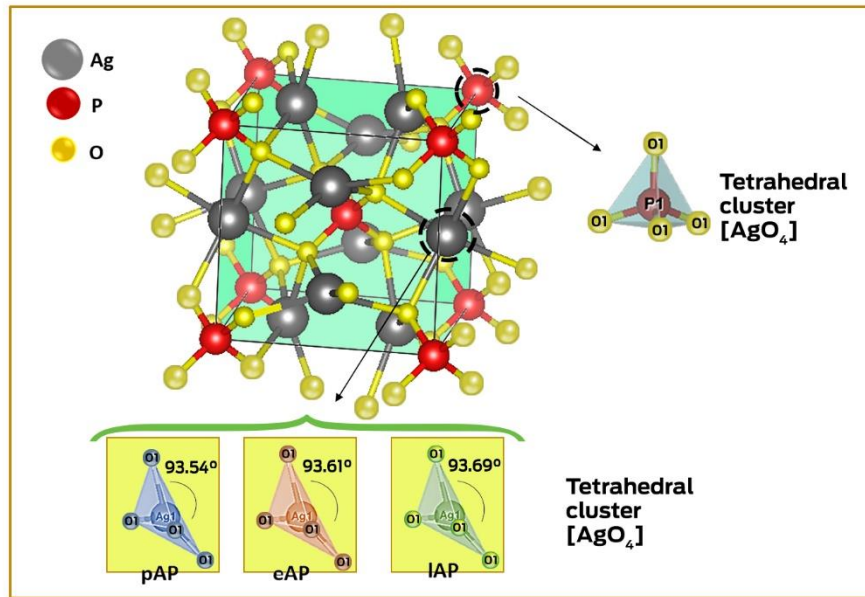


Figure 5: Schematic representation of the cubic body centered Ag_3PO_4 structure, illustrating $[\text{AgO}_4]$ and $[\text{PO}_4]$ clusters

3.1.3.3 Analysis of micro-Raman spectra

Raman spectroscopy was performed as a complementary technique to XRD to evaluate the order/disorder of the short-range. Figure 6 displays the Raman spectra obtained at room temperature for the pAP, eAP, and IAP samples. According to the analysis derived from the group theory, Ag_3PO_4 exhibits 18 active modes in the Raman spectrum, corresponding to $\Gamma=2A_1+4E+12T_2$ [32, 47]. The bands at 77 and 223 cm^{-1} are associated with external translational and rotation modes associated with the $[\text{PO}_4]$ clusters. The bending vibration modes related to the $[\text{PO}_4]$ group were found at 406 and 551 cm^{-1} . The band at 709 cm^{-1} corresponds to symmetrical stretching vibrations of P-O-P linkages in the $[\text{PO}_4]$ clusters. The band located at 908 cm^{-1} is related to the symmetrical stretching vibrations of $[\text{PO}_4]$, and asymmetrical stretching was verified at 951 and 1001 cm^{-1} [32, 48–51].

In the Raman spectra displayed in figure 6, changes in the intensity of the vibrational modes related to the $[\text{PO}_4]$ clusters such as those at 223, 551, 908, 951, and 1001 cm^{-1} can be observed. This behavior is more pronounced for IAP, indicating an important short-range disorder in this sample. Hence, a higher concentration of structural defects than pAP and eAP samples is provoked by the interaction of the fs laser.

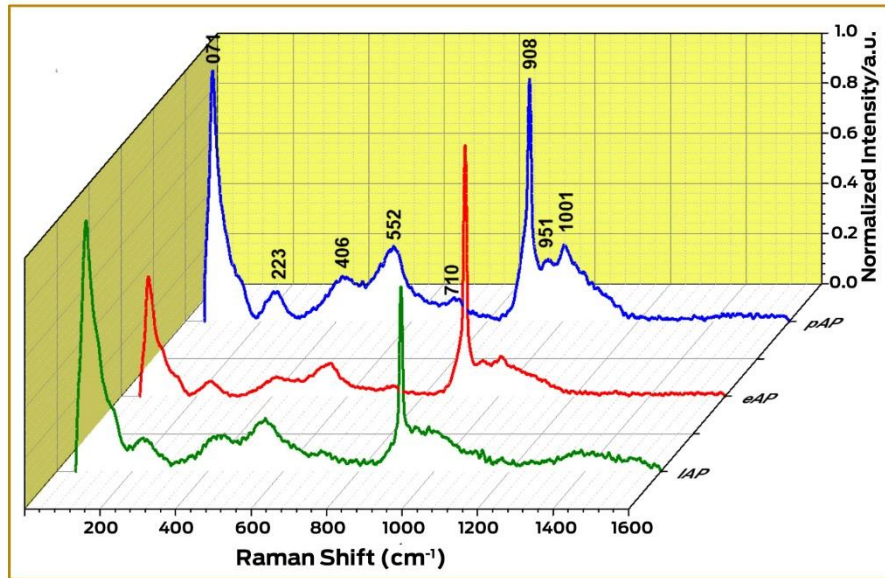


Figure 6: Micro-Raman of Ag_3PO_4 microcrystals: pure (pAP) electron irradiation (eAP) and femtosecond laser irradiation (IAP)

The analysis of the Raman spectra and Rietveld refinements indicates that both $[\text{PO}_4]$ and $[\text{AgO}_4]$ clusters are distorted with changes with respect to their equilibrium values for the O–P and O–Ag bond distances, and the O–P–O and O–Ag–O bond angles. One $[\text{PO}_4]$ cluster and three $[\text{AgO}_4]$ clusters are joined through the corner O anion. The Ag–O bonds of the $[\text{AgO}_4]$ clusters are more labile than the P–O bonds of the $[\text{PO}_4]$ clusters. Therefore, $[\text{PO}_4]$ clusters are more difficult to perturb by an external stimulus, making the $[\text{AgO}_4]$ clusters more susceptible to interact with incoming electrons/photons.

3.1.3.4 X-ray Photoelectron Spectroscopy

X-ray Photoelectron Spectroscopy measurements were performed to compare the pAP, eAP, and IAP samples. The XPS spectrum displayed in figure 7a indicates the presence of Ag, P, and O peaks, confirming the high degree of purity of the samples. Peaks related to C were also observed, which are related to the carbon

pollution from the XPS instrument itself [52–53]. The high resolution XPS spectra in figures 7b–d indicate two peaks with binding energies of approximately 367 eV and 373 eV, attributed to Ag 3d_{5/2} and Ag 3d_{3/2} orbitals, respectively [53–54]. Moreover, each of these peaks could be fitted in two separate components, indicating the presence of Ag in varied valences. These asymmetric peaks were fitted as described in figures 7b–d at 367.13/367.97 eV for Ag 3d_{5/2} and at 373.14/373.98 eV for Ag 3d_{3/2}. The high intensity peaks at 367.13 and 373.14 eV correspond to Ag⁺ ions, whereas the low intensity peaks at 367.97 and 373.98 eV are associated to metallic Ag [55–60].

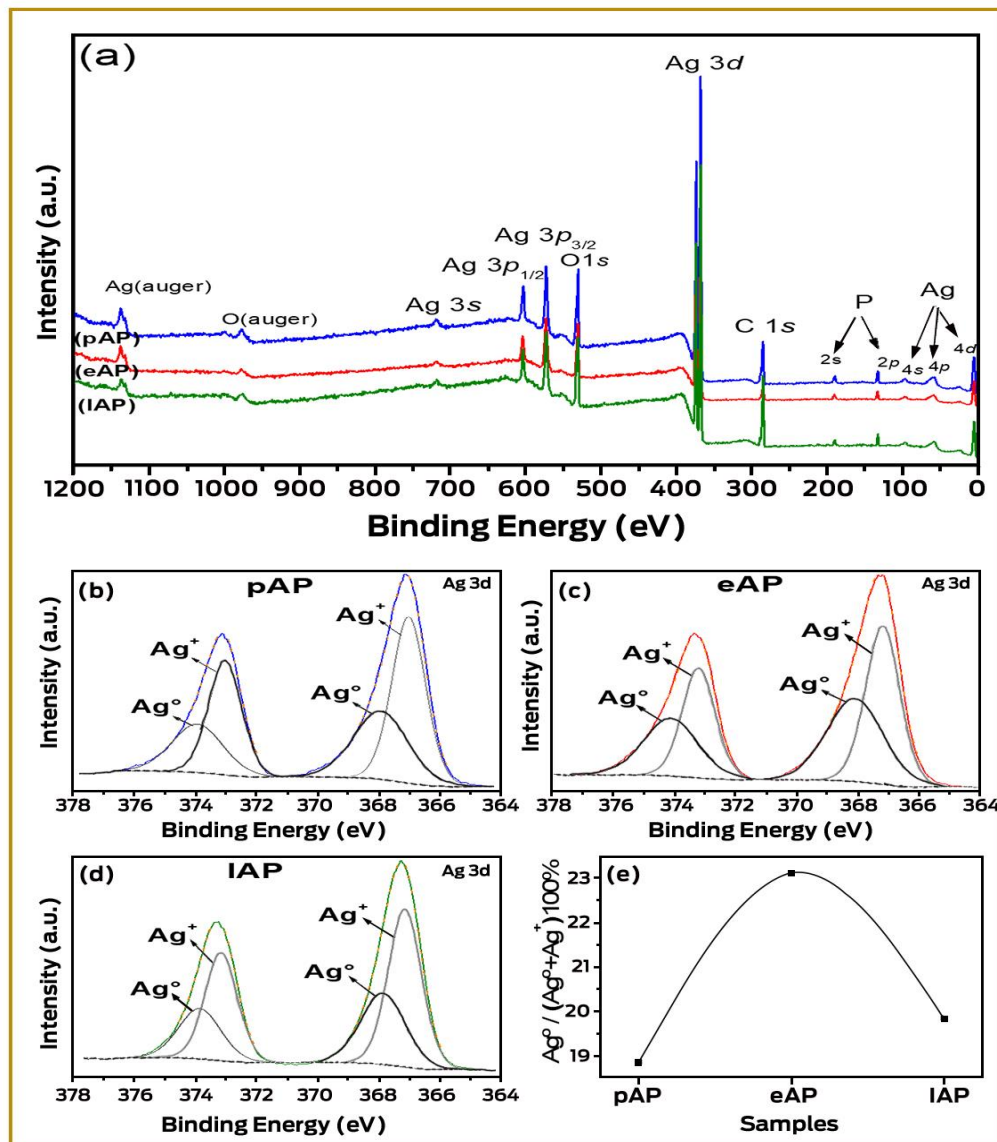


Figure 7: XPS survey spectrum of the samples microcrystals (a); High-resolution XPS spectra of Ag3d region of the samples pure (b), electron irradiation (c) and femtosecond laser irradiation (d); and the ratios of peak area attributed to Ag⁰ to the total area of all for these samples(e)

In the formed Ag/Ag₃PO₄ heterostructure, the amount of metal Ag in the microcrystals samples is considerably variable, i.e., the metallic Ag content for the pAP, eAP, and IAP samples was calculated, considering a mean area of metallic silver on the surface of the samples, to be 18.86%, 23.12%, and 19.85%, respectively. A higher metal Ag⁰ content is observed on the surface of the eAP sample, which is possibly associated with the larger amount fixed to the surface of the microcrystal, this is confirmed by the measurements of the scanning microscopy.

To examine the chemical characteristics of the P2p bond, we verified the high-resolution P2p level spectra for all the samples analyzed. Figure S2 in the supplementary material clearly indicates the spin-orbital division between the P2p_{1/2} and P2p_{3/2} peaks in the P2p core-level spectra, which corresponds to the characteristic binding energy of the P⁵⁺ oxidation state in Ag₃PO₄, the samples do not indicate significant differences.

3.1.3.5 FE-SEM analyses

FE-SEM images of pAP, eAP, and IAP exposure are displayed in Figure 8. In all the samples, irregular spherical microparticles with large size dispersion and aggregates can be observed. The particle dimensions for pAP, eAP, and IAP are 712, 468, and 432 nm, respectively. Further, it was possible to observe the nucleation and growth processes of metallic Ag NPs on the Ag₃PO₄ microcrystals surfaces. These processes occur via diffusion of the Ag⁺ species from their positions at the crystalline lattice corresponding to the [AgO₄] clusters to the Ag₃PO₄ surface, with subsequent reduction to Ag⁰. Both migration and reduction processes of the Ag⁺ species are provoked by the electron beam and laser irradiations. The metallic Ag nanoparticles on the eAP sample are predominantly rod-shaped, whereas the majority of the Ag nanoparticles on the IAP sample are composed of irregular spheres.

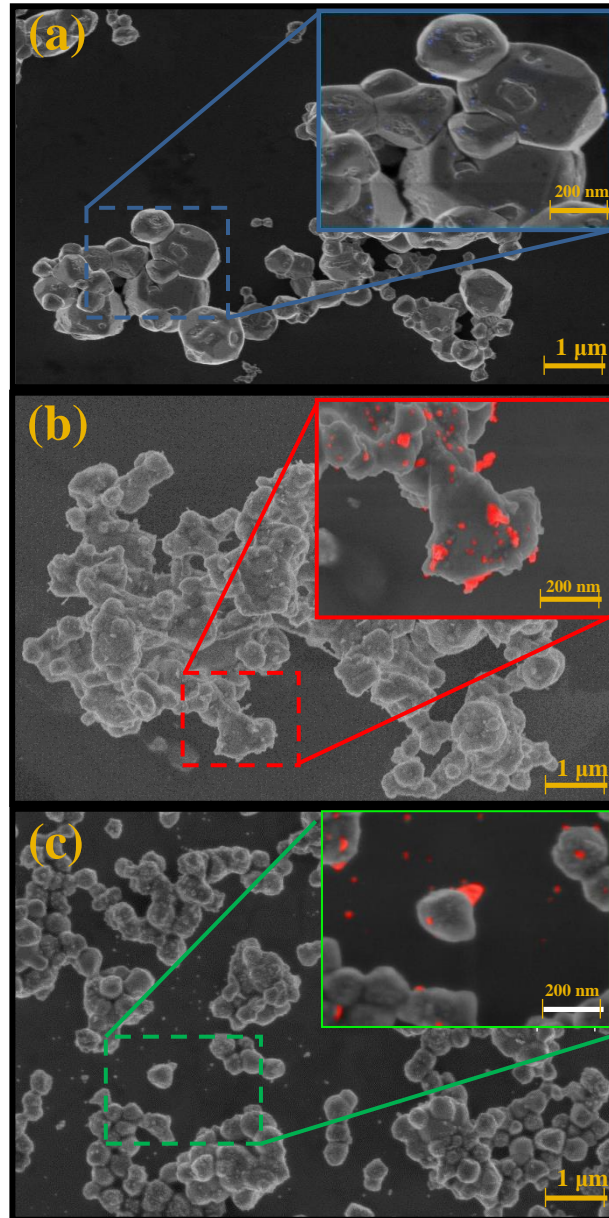


Figure 8: SEM images of Ag_3PO_4 microcrystals: pure (pAP) electron irradiation (eAP) and femtosecond laser irradiation (IAP). The Ag NPs are painted in red color

3.1.3.6 TEM analyses

The samples, pAP, eAP, and IAP, were also characterized by TEM. Figures 9a–c display the obtained TEM images at low magnification. As in the case of figure 9, the nucleation of Ag nanoparticles on the surface of the samples was also observed for eAP (nanorods) (Figure 9b) and IAP (irregular nanospheres) (Figure 9c). Moreover, owing to the high energy of the TEM analysis, the pAP also presented the initial stage of growth of Ag nanoparticles, which was included for comparison. To confirm this behavior of the nucleation of the Ag nanostructures, EDS analysis was also performed in two distinct regions of each image (Ag_3PO_4 and Ag nanoparticles).

Region 1 was selected in the center of the Ag_3PO_4 microparticle; Region 2 was selected in the Ag NPs. The results confirmed the presence of Ag, P, and O in Region 1 and predominantly Ag in Region 2, confirming the presence of metallic Ag in all samples. Cu and C refer to the sample port grid.

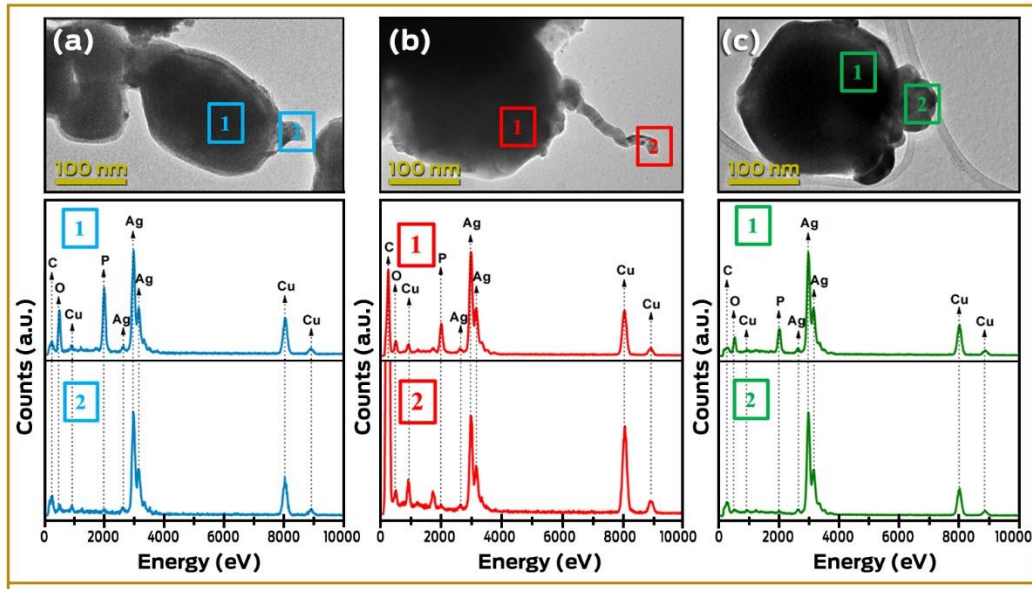


Figure 9: TEM of Ag_3PO_4 microcrystals: pure (pAP) electron irradiation (eAP) and femtosecond laser irradiation (IAP)

Different morphologies of Ag NPs were observed for both samples, as indicated in Figure 10a-b. The eAP sample presents a 1D nanostructure in the form of nanorods, Figure 10a, whereas the IAP sample presents a zero-dimensional nanostructure in the irregular spherical shape, Figure 10b. This difference in morphology of Ag nanoparticles is caused by the differences in the formation process, leading to different time, temperature and pressure conditions. For fs laser irradiation, the sample can reach a pressure around 1010 Pa and a temperature of 1000K [17], thus causing the formation of a large number of confined photons in a small area. Moreover, when irradiated with fs pulses the sample is in the steady state, that is, it does not present vibrational and rotational movements, since these occur in the second peak scale, which makes it difficult to follow the dynamic process of particle nucleation [15, 35].

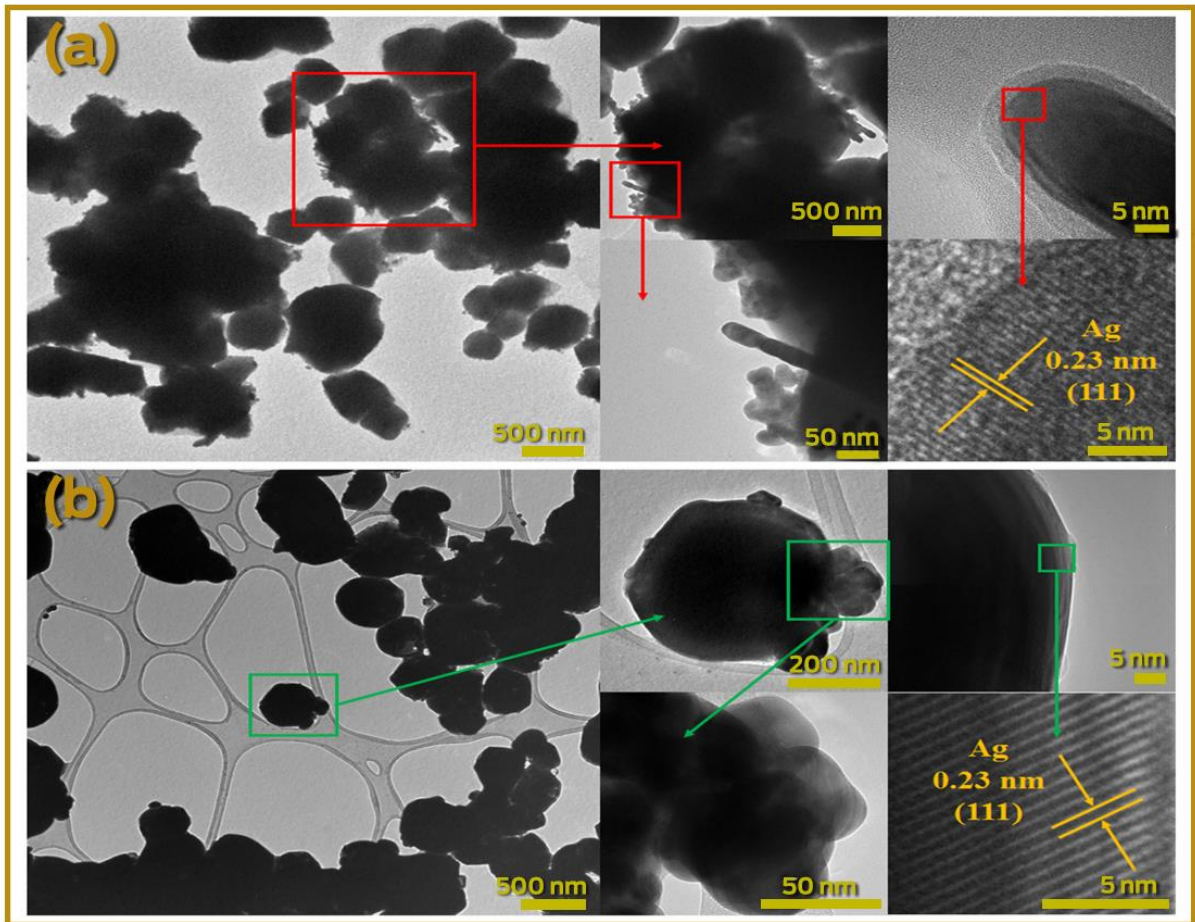


Figure 10: TEM micrographs at higher magnification of individual crystallites with: a) electron irradiation and b) femtosecond laser irradiation

These Ag nanoparticles were analyzed using HR-TEM in order to find the crystalline planes. The surface of these nanoparticles with light edges indicates a monocrystalline nature. This is confirmed by the reciprocal distances, with the strongest frame cubic metallic Ag nanoparticles characterized by a (111) plane with an interplanar distance of 0.23 nm (Figure 10), corresponding to PDF 89-3722 in the JCPDS (Joint Committee on Powder Diffraction Standards) [32].

In this part of the study, the initially formed Ag/Ag₃PO₄ composite of eAP and IAP samples were irradiated by a gradual converging electron beam. For this experiment, the electron beam of the TEM was condensed over these particles to increase the current density and to promote structural transformations. Figures 9a–b display the selected regions. An analysis of the results verifies that small and well-dispersed nanoparticles were formed near the initial Ag nanorod (eAP) or Ag irregular spheres (IAP) a few nanometers away from the initial Ag NPs. The HR-TEM images in

the insets of both figures demonstrate an interplanar distance of 0.23 nm for these particles, which can be associated to the (111) plane of cubic metallic Ag[61]. Thus, the exposure of a secondary electron beam from TEM leads to the growth of metallic Ag from the initial particles obtained in the eAP and IAP samples. Figures 11 a–b indicates that the dimensions of these particles are in the range of 2.26 and 3.36 nm for samples eAP and IAP, respectively. The Ag cations migrate from the matrix to the surface, resulting in structural and morphological modifications with the appearance of Ag vacancies [32].

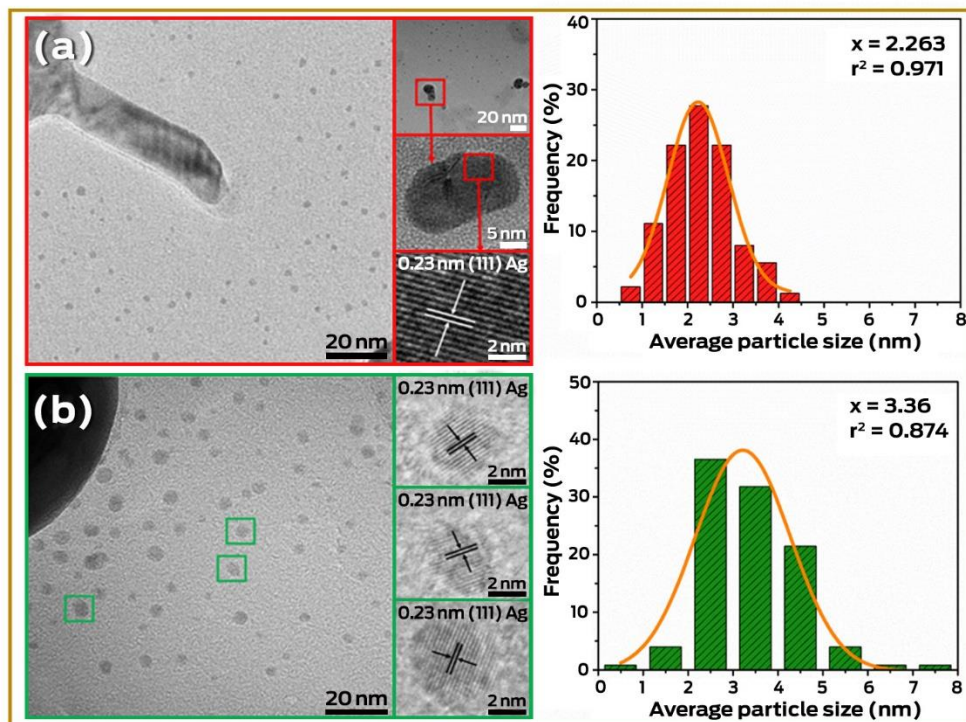


Figure 11: Distribution the particles of Ag° at the Ag_3PO_4 microcrystals with: a) electron irradiation and b) femtosecond laser irradiation

The above results can be viewed as an example of the electron beam-induced fragmentation process of the initial Ag particles by exposure to a condensed electron beam. This is a well-known process that results from the transfer of thermal energy and electric charge [62–63]. This phenomenon occurs in metallic samples that can melt and collapse into spherical units as the irradiating current density increases. The newly formed Ag NPs are expelled and “fly” in the carbon grid for several nanometers, as observed in the eAP and IAP samples.

3.1.3.7 Formation scheme of the Ag^0

Figure 12 presents the proposed growth mechanisms of the Ag NPs. The structure was irradiated with different energy levels, originating two morphologies associated to different metal nanoparticles, a nanobastones morphology, related to electron irradiation, and irregular spheres for fs laser irradiation.

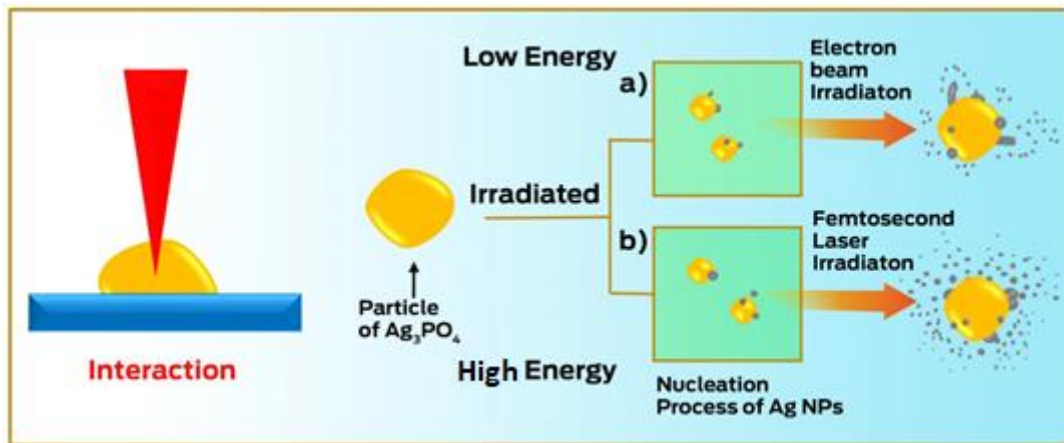


Figure 12: Schematic illustration of the proposed growth mechanism for the formation of metallic Ag on Ag_3PO_4 microcrystals: (A) surface interaction and (B) Coulomb explosion

The universality of Ag NPs generation through electron beam and/or fs laser pulses naturally indicates the existence of a common mechanism and in both cases, the interaction of the laser/electron beam on the Ag_3PO_4 provokes the reduction of Ag^+ ion to form metal Ag^0 . When the surface of the Ag_3PO_4 semiconductor is irradiated with an fs laser, the electrons of the valence band are excited to the conduction band. Because the electrons provide the bonding forces that hold atoms together in the lattice, if their distribution within the material changes significantly, the bonding forces can also change. At the local level, the multiphoton absorption of light leads to the excitation of the constituent clusters; $[\text{PO}_4]$ and $[\text{AgO}_4]$ are now located in an excited state where the Ag-O chemical bond no longer exists. This results in the formation of a plasma plume leading to the appearance of structural and electronic surface disorder. In the plasma, there are non-stoichiometric nanoparticles of Ag_3PO_4 and Ag metal. Then, the formation of metallic Ag and Ag vacancies occurs on the surface of the semiconductor.

The proposed mechanism for the formation of metallic Ag NPs on the surface of Ag_3PO_4 provoked by an electron beam is presented in figure 12. When the crystal of pAP is electron-irradiated, there is a reduction of Ag cations along an ordered movement from the bulk to the surface of the crystal. This promotes the formation of metallic Ag on its surface, which depends on the irradiation time and density of the injected electrons. Conversely, laser irradiation promotes an instantaneous Ag growth. Owing to the ultrashort pulse duration, fs scale, the pAP crystal loses symmetry and the metallic Ag NPs grows rapidly in a disorderly manner. These two experiments prove that electron and photons produce the same effect over the irradiated material. In this manner, the photo reduction and electron reduction effects, followed by an atomic displacement and Ag crystallization in the two experiments on the surface of a semiconductor crystal can be observed, see Figure 12b. The valence electrons responsible for the chemical bonds that hold the solids together are thus easily removed during the laser ablation process. This causes a mutually repulsive state between the atoms whose chemical bonds are broken, and the agglomerate explodes owing to mutual electrostatic repulsion of the ions.

3.1.4 Conclusion

We report, for first time, *in situ* nucleation and growth processes of Ag NPs on Ag_3PO_4 mediated by fs laser pulses. The results have been compared with previous observation in which these processes take place on Ag_3PO_4 driven by an accelerated electron beam from an electronic microscope under high vacuum. Present results allow us to gain a better understanding of these phenomena and allow a finer control to future technological applications, such as: forensic, biological and used in a variety of medical especialities, including ophthalmology, neurosurgery and veterinary. The main conclusions can be summarized as follows: i) XRD diffraction data render that the patterns for the pAP and eAP are similar, while IAP sample displays XRD pattern with lower resolution, showing a higher structural disorder at long-range; ii) Raman spectra and Rietveld refinements shows that both $[\text{PO}_4]$ and $[\text{AgO}_4]$ are distorted clusters, being the Ag-O bonds of $[\text{AgO}_4]$ clusters more labile than the P-O bonds of $[\text{PO}_4]$ clusters. Consequently, $[\text{PO}_4]$ clusters are more difficult to perturb by an external stimuli, being the $[\text{AgO}_4]$ clusters more susceptible to interact with incoming electrons/photons. This behavior is more pronounced for IAP samples; iii) XPS measurements point out that a larger metal Ag^0 content is observed on the surface of the eAP sample, which is confirmed by scanning microscopy measurements; iv) The metallic Ag nanoparticles on the eAP and IAP samples present rod-like and irregular sphere-like morphology, respectively; and v) A mechanism for the formation and growth of Ag nanoparticles on Ag_3PO_4 induced by electron beam and femtosecond laser irradiation has been proposed.

3.1.5 References

- [1] A. Moliton, *Electromagnetism and Materials*. Springer, **2007**.
- [2] R. Ramachandramoorthy, R. Bernal, H.D. Espinosa, *ACS Nano*. **2015**, 9, 4675.
- [3] J.M. Thomas, R.K. Leary, A.S. Eggeman, P.A. Midgley, *Chem. Phys. Lett.* **2015**, 103.
- [4] O. Ersen, I. Florea, C. Hirlimann, C. Pham-Huu, *Mater. Today*. **2015**, 18, 395.
- [5] I.G. Gonzalez-Martinez, A. Bachmatiuk, V. Bezugly, J. Kunstmann, T. Gemming, Z. Liu, G. Cuniberti, M.H. Rummeli, *Nanoscale* **2016**, 8, 11340.
- [6] W. Xiong, Y. Zhou, W. Hou, L. Jiang, M. Mahjouri-Samani, J. Park, X. He, Y. Gao, L. Fan, T. Baldacchini, J.F. Silvain, Y. Lu, *Front. Optoelectron.* **2015**, 8, 351.
- [7] G. G. Rubio G, P. Díaz-Núñez, A. Rivera, A. Prada, G. Tardajos, G. J. Izquierdo , L. Bañares, P. Llombart, L. G. Macdowell, M. A. Palafox, L. M. Liz-Marzán, O. Peña-Rodríguez, A. Guerrero-Martínez¹, *Science* **2017**, 8, 640.
- [8] L. Wang, Q. Li, H.Y. Wang, J.C. Huang, R. Zhang, Q.D. Chen, H.L. Xu, W. Han, Z.Z. Shao, H.B. Sun, *Light Sci. Appl.* **2015**, 4, 1.
- [9] M. Haque, K.K.C. Lee, S. Ho, L.A. Fernandes, P.R. Herman, *Lab Chip*. **2014**, 14, 3817.
- [10] A. Y. Vorobyev, C. Guo, *Laser Photonics Rev.* **2013**, 7, 385.
- [11] J. Bonse, J. Krüger, S. Höhm, A. Rosenfeld, *J. Laser Appl.* **2012**, 24, 042006.
- [12] J. Bonse, S. Höhm, S.V. Kirner, A. Rosenfeld, J. Krüger, *IEEE J. Sel. Top. Quantum Electron.* **2017**, 23, 109.
- [13] R. Buividas, M. Mikutis, S. Juodkazis, *Prog. Quantum Electron.* **2014**, 38, 119.
- [14] D. Tan, K.N. Sharafudeen, Y. Yue, J. Qiu, *Prog. Mater. Sci.* **2016**, 76, 154.
- [15] J. Andrés, A. F. Gouveia, L. Gracia, E. Longo, G. M. Faccin, E. Z. Silva, D. H. Pereira, M. A. San-Miguel, *Int. J. Quantum chem.* **2018**, 118, 25551.
- [16] G. M. Faccin, M. A. San-Miguel, J. Andrés, E. Longo, E. Z. Silva, *J Phys Chem C*. **2017**, 121, 7030.
- [17] M. Assis, E. Cordoncillo, R. Torres-Mendieta, H. Beltrán-Mir, G. Mínguez-Vega, R.C. Oliveira, E.R. Leite, C.C. Foggi, C.E. Vergani, E. Longo, J. Andrés, *Sci Rep.* **2018**, 8, 1.
- [18] V. M. Longo, C. C. De Foggi, M. M. Ferrer, A. F. Gouveia, R. S. André, W. Avansi, C. E. Vergani, A. L. Machado, J. Andrés, L. S. Cavalcante, A. C. Hernandez, E. Longo, *J. Phys. Chem. A*. **2014**, 118, 5769.

- [19] E. Longo, D.P. Volanti, V.M. Longo, L. Gracia, I.C. Nogueira, M.A.P. Almdeira, A.N. Pinheiro, M.M. Ferrer, L.S. Cavalcante, J. Andrés, *J. Phys. Chem. C* **2014**, *118*, 1229.
- [20] M. A. San-Miguel, E. Z. da Silva, S. M. Zanetti, M. Cilense, M. T. Fabbro, L. Gracia, J. Andrés, E. Longo, *principles. Nanotechnol* , **2016**, *27*, 225703.
- [21] J. Andrés, L. Gracia, P. Gonzalez-Navarrete, V.M. Longo, W.J. Avansi, D.P. Volanti, M.M. Ferrer, P.S. Lemos, F.A. La Porta, A.C. Hernandez, E. Longo, *Sci. Rep.* **2014**, 5391.
- [22] W. S. Pereira, J. Andrés J, L.Gracia, M. A. San-Miguel, E. Z. Silva, E. Longo, V. M. Longo, *Phys. Chem. Chem. Phys.* **2015**, *17*, 5352.
- [23] E. Longo, L.S. Cavalcante, D.P. Volanti, A.F. Gouveia, V.M. Longo, J.A. Varela, M.O. Orlandi, J. Andrés, *Sci. Rep.* **2013**, *3*, 1676.
- [24] R.A. Roca, A.F. Gouveia, P.S. Lemos, L. Gracia, J. Andrés, E. Longo, *Inorg. Chem.* **2016**, *55*, 8661.
- [25] R. A. Roca, P. S. Lemos, J. Andrés, E. Longo, *Chem. Phys. Lett.* **2016**, *244*, 68.
- [26] R. A. Roca, P. S. Lemos, L.Gracia, J. Andrés, E. Longo, *R. Soc. Chem.* **2017**, *7*, 5610.
- [27] M.T. Fabbro, L. Gracia, G.S. Silva, L.P.S. Santos, J. Andrés, E. Cordoncillo, E. Longo, *J. Solid State Chem.* **2016**, *239*, 220.
- [28] J. Andres, M. M. Ferrer, L. Lourdes, A. Beltran, V. M. Longo, G. H. Cruvinel, R. L. Tranquilin, E. Longo, *Part Part Syst Charact.* **2015**, *32*, 646.
- [29] G.S. Silva, L. Gracia, M. T. Fabbro, L. P. S. Santos, Luis P.; H. Beltran-Mir, E. Cordoncillo, E. Longo, J. Andres, *Inorg. Chem.* **2016**, *55*, 8961.
- [30] R.C. de Oliveira, S.M. Zanetti, M. Assis, M. Penha, M. Mondego, M. Cilense, E. Longo, L.S. Cavalcante, *J. Am. Ceram. Soc.* **2017**, *100*, 2358.
- [31] R. C. Oliveira, C. C. Foggi, M. Mondego, M. D. S. Penha, M. Assis, F. M. Francisco, B. N. A. S. Pimentel, P.F. S. Pereira, C. E. Vergani, A. L. Machado, J. Andrés, L. Garcia, E. Longo, *ACS Appl Mater Interfaces.* **2017**, *9*, 11472.
- [32] G. Botelho, J. C. Sczancoski, J. Andres, L. Gracia, E. Longo, *J. Phys. Chem.* **2015**, *119*, 6293.
- [33] M. Assis, E. Cordoncillo, R. Torres-Mendieta, H. Beltran, G. Minguez-Vega, A.F. Gouveia, E. R. Leite, J. Andrés, E. Longo, *Phys Chem Chem Phys.* **2018**, *20*, 13693.
- [34] M. Assis, N. G. Macedo, T. R. Machado, M. M. Ferrer, A. F. Gouveia, E. Cordoncillo, R. Torres-Mendieta, H. Beltrán-Mir, G. Mínguez-Vega, E.R. Leite, J. R. Sambrano, J. Andrés, E. Longo, *Part Part Syst Charact.* **2018**, *180037*, 1.

- [35] T. R. Machado, N. G. Macedo, M. Assis, C. Doñate-Buendia, G. Mínguez-Vega, Gladys, M. T. Teixeira, C.C. Foggi, C. E. Vergani, H. Beltrán-Mir, Héctor, J. Andrés, E. Cordoncillo, E. Longo, *ACS Omega*. **2018**, 3, 9880.
- [36] Y. Liu, L. Fang, H. Lu, L. Liu, H. Wang H, C. Hu, *Catal. Commun.* **2012**, 17, 200.
- [37] J. Yu, J. Yu, T. Ying, C. Cui, Y. Sun, X. Liu, *J Alloy Compd.* **2019**, 775, 225.
- [38] W. Teng, X. Li, Q. Zhao, J. Zhao, D. Zhang. *Appl Catal B-Environ.* **2012**, 125, 538.
- [39] M. A. Gondal, X. Chang, W. E. I. Sha, Z. H. Yamani, Q. Zhou, *J Colloid Interf Sci.* **2013**, 392, 325.
- [40] K. Huang, Y. Lv, W. Zhang, S. Sun, B. Yang, F. Chi, S. Ran, X. Liu, *Mater. Res. Lett.* **2015**, 18, 939.
- [41] Y. Bi, H. Hu, S. Ouyang, Z. Jiao, G. Lu, J. Ye, *Chem.Eur. J.* **2012**, 18, 14272.
- [42] T. Yana, W. Guan, Y. Xiao, J. Tiaa, Z. Qiao, H. Zhai, W. Li, J. Youa, *Appl Surf Sci.* **2017**, 391, 592.
- [43] W. Teng, X. Y. Li., Q. D. Zhao, J. J. Zhao, D. K. Zhang, *Appl Catal B-Environ.* **2012**, 125, 538.
- [44] J. J. Liu, X. L. Fu, S. F. Chen, Y. F. Zhu, J. J. Liu, X. L. Fu, S. F. Chen, Y. F. Zhu, *Appl. Phys. Lett.* **2011**, 99, 2011.
- [45] H. M. A Rietveld, *J. Appl. Crystallogr.* **1969**, 2, 65.
- [46] B. H Toby, *J. Appl. Crystallogr.* **2001**, 34, 210.
- [47] X. Q. Liu, W. J. Chen, H. Jiang, *Chem Eng J.* **2017**, 308, 889.
- [48] Q. Liang, Y. Shi, W. Ma, Z. Li, X. Yang, *Chem Chem Phys.* **2012**, 14, 15657.
- [49] P. Dong, Y. Wang, B. Cao, S. Xin, L. Guo, J. Zhang, F. Li, *Appl. Catal., B.* **2013**, 132, 44..
- [50] L.W. Cheng,; J. C. Tsai, T. Y. Huang, C. W. Huang, B. Unnikrishnan, Y.W. Lin, *Mater. Res. Express*, **2014**, 1, 1.
- [51] M. Mroczkowska, J. L. Nowinski, G. Z. Zukowska, A. Mroczkowska, J. E. Garbarczyk, M. Wasiucioneck, S. Gierlotka, *J. Power Sources*, **2007**, 173, 729.
- [52] W. Teng, X. Li, Q. Zhao, G. Chen, *J. Mater. Chem. A.* **2013**, 1, 9060.
- [53] D. Seo, J. C. Park, H. Song, *J. Am. Chem. Soc.* **2006**, 128, 14863.
- [54] P. Wang, B. Huang, Q. Zhang, X. Zhang, X. Qin, Y. Dai, J. Zhan, J. Yu, H. Liu, Z. Lou, *Chem. Eur. J.* **2010**, 16, 10042.
- [55] P. Dong, G. Hou, C. Liu, H. Tian, F. Xu, X. Xi, R. Shao, G.R. Patzke, ed. *Materials.* **2016**, 9, 968.

- [56] C.G. Kontoyannis, N.V. Vagenas, *Analyst*. **2000**, 125, 251.
- [57] T. Yan, W. Guan, J. Tian, P. Wang, B. Huang, J. *Alloys Compd.* **2016**, 680, 436.
- [58] J. Wan, E. Liu, J. Fan, X. Hu, L. Sun, C. Tang, Y. Yin, H. Li, Y. Hu, *Ceram. Int.* **2015**, 41, 6933.
- [59] H. Zhang, W. Geng, D. Ghen, X. Lv, J. Li, *Chem. Mater.* **2008**, 20, 6543.
- [60] L. Cai, X. Xiong, N. Liang, Q. Long, *Appl. Surf. Sci.* **2015**, 353, 939.
- [61] W. S. Pereira, J. C. Sczancoski, Y. Colmenares, V. Mastelaro, G. Botelho, T. Machado, E. R. Leite, E. Longo, *Appl. Surf. Sci.* **2018**, 440, 61.
- [62] J. M. P. Coelho, C. Silva, A. Ruivo, A. P. Matos, *Mater. Sci. Forum*, **2012**, 915, 730.
- [63] W. D. Pyrz, S. Park, T. Vogt, D. J. Buttrey, *J. Phys. Chem. C.* **2007**, 111, 10824.
- [64] E. K. Fields, Seymour Meyerson, *J. Org. Chem.*, **1976**, 41, 916.
- [65] H.-T. Chen, H.-L. Lin, C. Kuo and I.-G. Chen, *J. Mater. Chem. C*, **2016**, 4, 7675.

3.2 $\text{Ag}_{2-2x}\text{Zn}_x\text{WO}_4$ ($0 \leq x \leq 0.25$) Solid Solutions: Structure, Morphology and Optical Properties

3.2.1 Abstract

A theoretical study was elaborated to support the experimental results of the Zn-doped $\alpha\text{-Ag}_2\text{WO}_4$. These $\alpha\text{-Ag}_{2-2x}\text{Zn}_x\text{WO}_4$ ($0 \leq x \leq 0.25$) solid solutions were obtained by coprecipitation method. X-ray diffraction data indicated that all $\alpha\text{-Ag}_{2-2x}\text{Zn}_x\text{WO}_4$ ($0 \leq x \leq 0.25$) microcrystals presented an orthorhombic structure. The experimental values of the microRaman frequencies were in reasonable agreement with both previously reported and calculated results. Microscopy images showed that the replacement of Ag^+ by Zn^{2+} promoted a reduction in the average crystal size and modifications in the morphology, from rod-like with hexagonal shape to roll-like with a curved surface. A theoretical methodology based on the surfaces calculations and Wulff constructions was applied to study the particle shapes transformations and the surface energy variations in $\alpha\text{-Ag}_{2-2x}\text{Zn}_x\text{WO}_4$ ($0 \leq x \leq 0.25$) system. The decrease in the band gap value (from 3.18 to 3.08 eV) and the red shift in photoluminescence with the Zn^{2+} addition were associated with intermediary energy levels between the valence and conduction bands. First-principles calculations with density functional theory associated with B3LYP hybrid functional were conducted. The calculated band structures revealed an indirect band gap for the $\alpha\text{-Ag}_{2-2x}\text{Zn}_x\text{WO}_4$ models. The electronic properties of $\alpha\text{-Ag}_2\text{WO}_4$ and $\alpha\text{-Ag}_{2-2x}\text{Zn}_x\text{WO}_4$ microcrystals were linked to distortion effects and oxygen vacancies (V^{\times}_O) present in the clusters, respectively. Finally, photoluminescence properties of $\alpha\text{-Ag}_2\text{WO}_4$ and $\alpha\text{-Ag}_{2-2x}\text{Zn}_x\text{WO}_4$ microcrystals were explained by means of distortional effects and oxygen vacancies (V^{\times}_O) in $[\text{AgO}_y]$ ($y = 2, 4, 6, \text{ and } 7$) and $[\text{WO}_6]$ clusters, respectively, causing a red shift. Calculations revealed that the substitution for Ag^+ with Zn^{2+} occurred randomly in the $\alpha\text{-Ag}_2\text{WO}_4$ lattice, and it was more favorable on the Ag4 site, where the local coordination of Ag^+ cations was four.

3.2.2 Introduction

Metal tungstates are a well-known family of inorganic materials due to their prominent properties with multifunctional applications in many fields such as catalysis, photocatalysis, microbial agents, and luminescence [1–12]. α - Ag_2WO_4 is a significant member of this family, and a variety of particle characteristics and properties have been obtained using different methods such as electrochemical [13], sonochemical [3,14], supersonic assisted homogeneous precipitation [15] conventional hydrothermal [3] hydrothermal microwave [5,16–21] and coprecipitation method [3,4,16,22–30]. Very recently, Fan *et al.* reported a preparation method for highly uniform one-dimensional α - Ag_2WO_4 nanostructures with a controllable aspect ratio [31]. α - Ag_2WO_4 has received significant attention owing to its potential applications, in different fields such as organic catalysis [24,32,33], photocatalysis [4,17,34] electrocatalysis [25] gas sensing [1,19] dye adsorbents [14], photoswitches [35], and as antimicrobia [5] and antibacterial agents [14,15,17]. These unique features provide the opportunity to tailor the basic physical and chemical properties and performance of α - Ag_2WO_4 compounds by intentionally mixing them with metals. Obtaining solid solutions, formed by a mixture of two or more crystalline solids, is found to be a very effective strategy to tailor the crystal structure, continuous tunability of band gap values, and optical properties. Solid solutions may have new properties or improve on those existing in separate phases. In particular, the synthesis and formation mechanisms of the solid solutions of metal tungstate, their stability and corresponding properties, as well as the potential technological applications, are important topics of research. In this context, the synthesis and characterization of solid solutions involving metal tungstates such as $\text{Sr}_{1-x}\text{Pb}_x\text{WO}_4$ [36], $\text{Ca}_{1-x}\text{Sr}_x\text{WO}_4$ [37], $\text{Ba}_{1-x}\text{Sr}_x\text{WO}_4$ [38], and $\text{Sr}_{1-x}\text{Ba}_x\text{WO}_4$ [37] have been performed. The photoluminescence (PL) properties of $\text{Ca}_x\text{Sr}_{1-x}\text{WO}_4$ [39] and $\text{Ca}_{1-x}\text{Cd}_x\text{WO}_4$ [40] have been analyzed, while the structures, optical properties, and magnetism have been studied for $\text{Zn}_{1-x}\text{Ni}_x\text{WO}_4$ [41], $\text{Mn}_{1-x}\text{Cu}_x\text{WO}_4$ [42], $\text{Cd}_{1-x}\text{Zn}_x\text{WO}_4$ [43], $\text{Ni}_{1-x}\text{Co}_x\text{WO}_4$ [44], $\text{Zn}_{1-x}\text{Cu}_x\text{WO}_4$ [45] and $\text{Zn}_{1-x}\text{Co}_x\text{WO}_4$ [46]. Our group is engaged in a research devoted to finding a rational synthesis of solid based on the α - Ag_2WO_4 material, and very recently, we performed a study on the effects of chemical substitution of α - $\text{Ag}_{2-2x}\text{Ni}_x\text{WO}_4$ solid solutions [47]. α - Ag_2WO_4 presents an orthorhombic structure with space group $Pn2n$. Each W cation is bonded to six oxygen atoms, while the

Ag cations are found to have two-, four-, six-, and sevenfold coordinated geometries. Therefore, the corresponding building blocks of this structure are the $[\text{WO}_6]$ cluster with Oh symmetry and $[\text{AgO}_y]$ ($y = 2, 4, 6, \text{ and } 7$) clusters with C_{2v} , Td , Oh , and D_{5h} symmetries, respectively. These clusters are distorted, because different W-O and Ag-O distances can be sensed, and then these clusters present deviations from the ideal symmetry [3,48]. ZnWO_4 has a monoclinic structure with the space group P2/c , where six oxygen ions are arranged around W and Zn cations forming a distorted octahedral coordination, corresponding to $[\text{WO}_6]$ and $[\text{ZnO}_6]$ clusters, respectively.⁴⁹ In both $\alpha\text{-Ag}_2\text{WO}_4$ and ZnWO_4 structures, all clusters are asymmetric and not homogeneous. This fact results in a set of nonequivalent clusters of metal–oxygen bonds distributed over the lattice. In addition, differences in the ionic radii and charges between Ag^+ and Zn^{2+} may produce lattice distortions and vacancies in the crystal. Thus, through the substitution of Ag^+ with Zn^{2+} in $\alpha\text{-Ag}_2\text{WO}_4$, an interesting prospect for applications is the control of material properties in the corresponding solid solution by disturbance of the local M-O environment.

Herein, we developed new $\alpha\text{-Ag}_{2-2x}\text{Zn}_x\text{WO}_4$ ($0 \leq x \leq 0.25$) solid solutions via a simple coprecipitation (CP) method. The structure was confirmed by X-ray diffraction (XRD), X-ray fluorescence spectrometry (XRF), Rietveld refinement data, micro-Raman (MR) and Fourier transform infrared (FTIR) spectroscopies. The optical properties were investigated by ultraviolet–visible (UV–vis) diffuse reflectance spectroscopy and photoluminescence (PL). Field-emission scanning electron microscopy (FE-SEM) images were employed to evaluate the shapes, sizes, and growth processes of the crystals as the doped concentration of Zn^{2+} ions in the $\alpha\text{-Ag}_2\text{WO}_4$ network was increased. To complement these experimental results, theoretical calculations with the density functional theory (DFT) were performed. The electronic information, such as band structure and density of states (DOS), and Raman spectra were calculated to understand the phenomenon of structural order–disorder in the $\alpha\text{-Ag}_2\text{WO}_4$ structure caused by Zn^{2+} replacement. The paper is organized in three other sections. Section 2 describes the methodology details. Section 3 exposes the results and the discussion concerning the structural and properties characteristics. The paper combined experimental and theoretical results in order to understand the relationship between the structural modifications and the obtained PL properties. Section 4 describes our conclusions.

3.2.3 Experimental Procedures

3.2.3.1 Synthesis

The α - $\text{Ag}_{2-2x}\text{Zn}_x\text{WO}_4$ ($x = 0, 0.05, 0.10, 0.15, 0.20$ and 0.25) microcrystals were prepared by the CP method. The procedure for the typical α - $\text{Ag}_{2-2x}\text{Zn}_x\text{WO}_4$ microcrystals synthesized by the CP method is described as follows: 1×10^{-3} mol of tungstate (VI) sodium dihydrated ($\text{Na}_2\text{WO}_4 \cdot 2\text{H}_2\text{O}$; 99.5% purity, Sigma-Aldrich) and 2×10^{-3} mol of silver (I) nitrate (AgNO_3 ; 99.8% purity, Sigma-Aldrich) were dissolved separately in 50 mL of deionized water at 80 °C under magnetic stirring. The solution with Ag^+ and NO_3^- was added to the solution containing the WO_4^{2-} ions, and this solution remained at 80 °C under magnetic stirring for 30 min. After that, a yellow suspension appeared, and a white precipitate was rapidly formed. The solid solutions were prepared according to the molar ratio in α - $\text{Ag}_{2-2x}\text{Zn}_x\text{WO}_4$ ($x = 0.05, 0.10, 0.15, 0.20,$ and 0.25) considering the charge balance between Ag^+ and Zn^{2+} . Zinc nitrate octahydrated ($\text{Zn}(\text{NO}_3)_2 \cdot 8\text{H}_2\text{O}$; 99.99% purity, Sigma-Aldrich) was added to AgNO_3 solution, and the procedure was similar to that described for the α - Ag_2WO_4 . The resulting suspensions were washed several times with deionized water to remove the residual Na^+ ions. The crystalline α - $\text{Ag}_{2-2x}\text{Zn}_x\text{WO}_4$ microcrystals were collected and dried in an oven at 70 °C.

3.2.3.2 Characterization

These α - $\text{Ag}_{2-2x}\text{Zn}_x\text{WO}_4$ microcrystals were structurally characterized by XRD patterns using a D/Max-2000PC diffractometer Rigaku (Japan) with Cu K α radiation ($\lambda = 1.5406 \text{ \AA}$) in the 2θ range from 10° to 70° in the normal routine with a scanning velocity of 2°/min and from 10° to 110° with a scanning velocity of 1°/min in the Rietveld routine. XRF analyses were performed on a Shimadzu EDX 720 XRF spectrometer. MR spectroscopy was conducted on a Horiba Jobin-Yvon (Japan) spectrometer chargecoupled device detector and argon-ion laser (Melles Griot, United States) operating at 514.5 nm with maximum power of 200 mW. The spectra were measured in the range of 250–1000 cm^{-1} . FTIR spectroscopy was recorded in the range from 250 to 1000 cm^{-1} using KBr pellets as a

reference in a Bomem–Michelson spectrophotometer in transmittance mode (model MB102). The shapes and sizes of these $\alpha\text{-Ag}_{2-2x}\text{Zn}_x\text{WO}_4$ microcrystals were observed with an FE-SEM Inspect F50 (FEI Company, Hillsboro, OR) operated at 5 kV. The optical properties of the $\alpha\text{-Ag}_{2-2x}\text{Zn}_x\text{WO}_4$ microcrystals were analyzed by UV–vis and PL spectroscopies. UV–vis spectra were taken using a (Varian, USA) spectrophotometer (model Cary 5G) in a diffusereflectance mode. PL measurements were performed through a Monospec 27 monochromator (Thermal Jarrel Ash) coupled to a R446 photomultiplier (Hamamatsu Photonics, Japan). A krypton-ion laser (Coherent Innova 90K; $\lambda = 350.7$ nm) was used as the excitation source; its maximum output power was maintained at 500 mW. The laser beam was passed through an optical chopper, and its maximum power on the sample was maintained at 40 mW. PL measurements were performed at room temperature.

3.2.3.3 Theoretical Methods

All theoretical calculations for the $\alpha\text{Ag}_2\text{WO}_4$ and $\alpha\text{-Ag}_{2-2x}\text{Zn}_x\text{WO}_4$ structure were performed with the CRYSTAL [14] software package [50]. This code uses a Gaussian-type basis set to represent crystalline orbitals as a linear combination of Bloch functions defined in terms of local functions (atomic orbitals). The computational method is based in the DFT associated with the Becke’s three-parameter hybrid nonlocal exchange functional [51] combined with a Lee–Yang–Parr gradient-corrected correlation functional [52] (B3LYP). The diagonalization of the Fock matrix was performed using a (4×4×4) Pack-Monkhorst k-points grid in the reciprocal-space. The thresholds controlling the accuracy of the calculation of the Coulomb and exchange integrals were set to 1×10^{-8} and 1×10^{-14} , and the percent of Fock/Kohn–Sham matrix mixing was set to 30 (IPMIX keyword). The lattice parameters and the internal atomic coordinates were fully optimized until all force components were less than 1×10^{-6} eV \AA^{-2} . The basis sets to describe the atomic centers of $\alpha\text{-Ag}_2\text{WO}_4$ were the same as those employed by Longo et al., [52]. Zn atoms were described by 86–411d31G, which was obtained from the Crystal Web site [53]. The Raman vibrational modes and their corresponding frequencies were calculated using numerical second derivatives of total energies as implemented in the CRYSTAL [14] package [50]. The band structure and DOS of the models were constructed along the appropriate high-symmetry directions of the corresponding irreducible Brillouin zone. Three models were constructed to more accurately

describe structural and electronic properties derived from the experimental synthesis, a pure $\alpha\text{-Ag}_2\text{WO}_4$, and two models in which the Zn^{2+} cation substitutes the Ag^+ cation Ag^+ and Zn^{2+} cations. To evaluate the stability of substituted structures, we directly compared the total energies of the Zn replacement in the $\alpha\text{-Ag}_2\text{WO}_4$. The procedure to obtain the complete set of morphologies, based on the Wulff construction, has been previously presented by Andres *et al.*, [54].

3.2.4 Results and Discussion

3.2.4.1 XRD and XRF analysis

The long-range order of $\alpha\text{-Ag}_{2-2x}\text{Zn}_x\text{WO}_4$ was evaluated by XRD diffraction. Figure 13-f shows the XRD patterns of the $\alpha\text{-Ag}_{2-2x}\text{Zn}_x\text{WO}_4$ microcrystals, where $x = 0.0, 0.05, 0.10, 0.15, 0.20,$ and 0.25 , respectively, obtained by the CP at $80\text{ }^\circ\text{C}$ for 30 min.

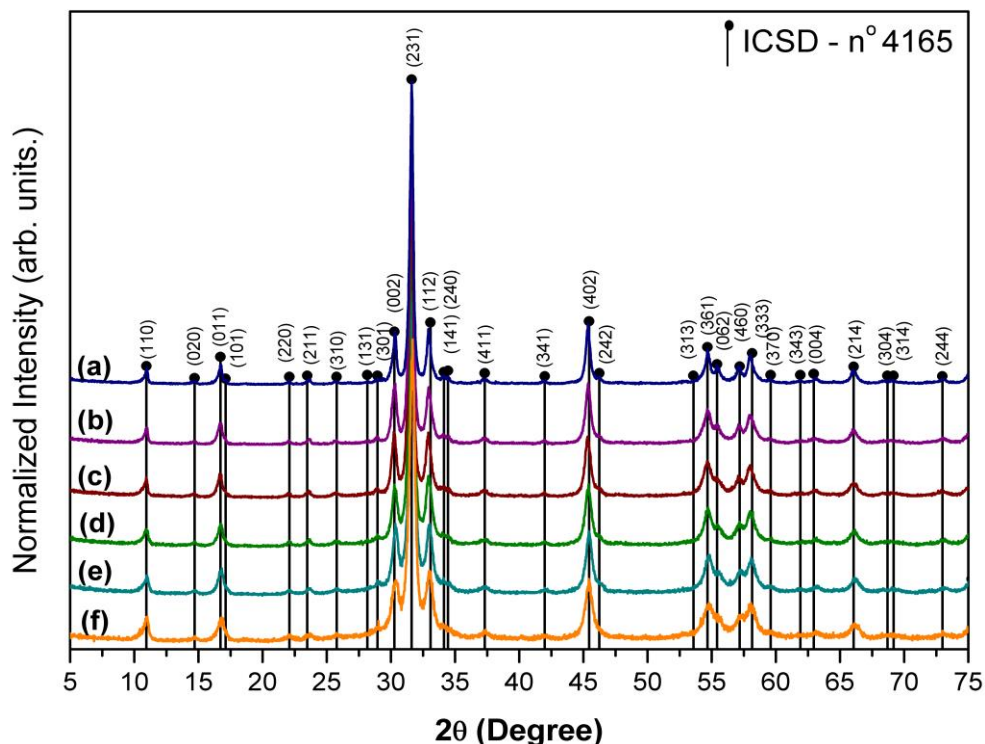


Figure 13: XRD of the $\alpha\text{-Ag}_{2-2x}\text{Zn}_x\text{WO}_4$ (where $x =$ (a) 0, (b) 0.05, (c) 0.10, (d) 0.15, (e) 0.20, and (f) 0.25) microcrystals obtained by the CP method at $80\text{ }^\circ\text{C}$ for 30 min.

The XRD patterns (Figure 13) confirm that all $\alpha\text{-Ag}_{2-2x}\text{Zn}_x\text{WO}_4$ samples have a pure orthorhombic structure (space group $\text{Pn}2_1$, $\text{C}2v$ 10 symmetry) [55,56] in accordance with the Inorganic Crystal Structure Database card No. 4165. The well-defined diffraction peaks of figure 13 suggest a high degree of crystallinity [57], for all materials. It is noticed that

the orthorhombic periodicity was not affected by the presence of Zn^{2+} ions (see Figure 13b–f). The presence of Zn^{2+} in the lattice causes only a small structural distortion, confirmed by the lower definition of the diffraction peaks and the small shift observed in the strongest diffraction peaks of figure SI-1. However, the diffraction peaks were slightly shifted to higher 2θ values as the Zn^{2+} ion concentration was increased, resulting in smaller interplanar distances. The left shift observed in some peaks of the $x = 0.10$ sample is possibly caused by the creation of homogeneous defects induced by the structure relaxation. This relaxation is due to the number of vacancies and the kinds of sites occupied by the Zn atoms. The XRD results (Figure 1) indicate that the Zn^{2+} ions have been incorporated into the lattice and induced a slight reduction in the unit cell volume. It is important to note that the $x = 0.25$ is the maximum Zn doping value, because from a large value of x the network $\alpha\text{-Ag}_2\text{WO}_4$ is not maintained and even appears the formation of other phases (see figure SI-2).

The presence of Zn^{2+} ions and their relative values in comparison with the Ag^{1+} were confirmed by XRF analysis (see Table SI-1). This methodology was used for the determination of silver and zinc concentrations in the $\alpha\text{-Ag}_{2-2x}\text{Zn}_x\text{WO}_4$ structure by direct nondestructive method. The results show that the molar amounts were close to the calculated values for the syntheses. Some small deviations observed between theoretical and experimental values are assigned to matrix effects and equipment errors, such as calibration curve and interference effects.

3.3.4.2. Rietveld Refinement Analysis

A detailed study of the XRD patterns was conducted by means of Rietveld refinement analysis using the General Structure Analysis System (GSAS) program [58]. This technique allows an estimation of real structure parameters comparing the XRD peak profiles with the profile of other reported papers [59]. In these analyses, the background was refined using a Chebyshev polynomial of the first kind, and the peak profiles were adjusted by the Thompson-Cox-Hastings pseudo-Voigt (pV–TCH)60 function with the asymmetry function described by Finger et al [61]. The anisotropy in halfwidth was taken into account using the model developed by Stephens [62].

In this paper, we performed the Rietveld refinement to check the effects of the substitution of Ag^+ by Zn^{2+} in the crystalline structure of $\alpha\text{-Ag}_2\text{WO}_4$. Rietveld refinement plots

of $\alpha\text{-Ag}_{2-2x}\text{Zn}_x\text{WO}_4$ for (a-f) $x = 0, 0.05, 0.10, 0.15, 0.20,$ and $0.25,$ respectively, are shown in Figure SI-3. The Rietveld results were in accordance with ICSD Card No. 4165.55 The crystals exhibited a single phase, confirming that there is a substitution for Ag^+ by Zn^{2+} cations in all samples ($x = 0.05, 0.10, 0.15, 0.20,$ and 0.25). Figure SI-3a-f shows good concordance between the experimental XRD patterns and theoretical results. This affirmation is based on the slight differences between the experimental intensity (Y_{Obs}) and the calculated intensity (Y_{Calc}), as shown by the line $Y_{\text{Obs}} - Y_{\text{Calc}}$. So, the quality of the refinement is generally checked using R-values ($R_{\text{wp}}, R_{\text{Bragg}}, R_{\text{p}},$ and χ^2). The Table SI-2 shows low deviations in the R-values, suggesting that the refinement result presents acceptable values. Additional information concerning the refinement reliability and the cell information are illustrated in Table SI-2. On the basis of the Rietveld refinement, there is a small difference between the unit cell parameters of each sample. The volume of the unit cell decreased with the Zn^{2+} incorporation; this is a consequence of the decrease in the cell parameters (see Table SI-2). Therefore, the substitution process of Ag^+ by Zn^{2+} provokes a rearrangement of the geometry for the $[\text{AgO}_y]$ by $[\text{ZnO}_y]$ ($y = 2, 4, 6,$ and 7) clusters; then, the local geometry of the metals ($\text{W}, \text{Ag},$ and Zn) and their corresponding interactions with oxygen anions contribute to the structural and electronic modifications. Tables SI-3 and SI-4 shows the atomic positions for $\text{Ag}, \text{W}, \text{O},$ and Zn estimated in the refinement. These results show that there are changes in the positions of all atoms ($\text{Ag}, \text{W},$ and O), even with the introduction of a low Zn^{2+} concentration. These variations are more pronounced in the O positions, since they are the lighter atoms and form connections between the adjacent clusters along the $[\text{AgO}_y]\text{-}[\text{ZnO}_y]$ ($y = 2, 4, 6,$ and 7) framework.

3.2.4.3 Unit Cell Representation for $\alpha\text{-Ag}_{2-2x}\text{Zn}_x\text{WO}_4$

Figure 14 displays a schematic representation of the $\alpha\text{-Ag}_{1.50}\text{Zn}_{0.25}\text{WO}_4$ orthorhombic unit cell. This structure was modeled using the Visualization for Electronic and Structural Analysis (VESTA) program [63]. From the lattice parameters and atomic coordinates obtained through of the Rietveld refinements (listed in Table SI-4), it was possible to construct the unit cell represented in figure 14.

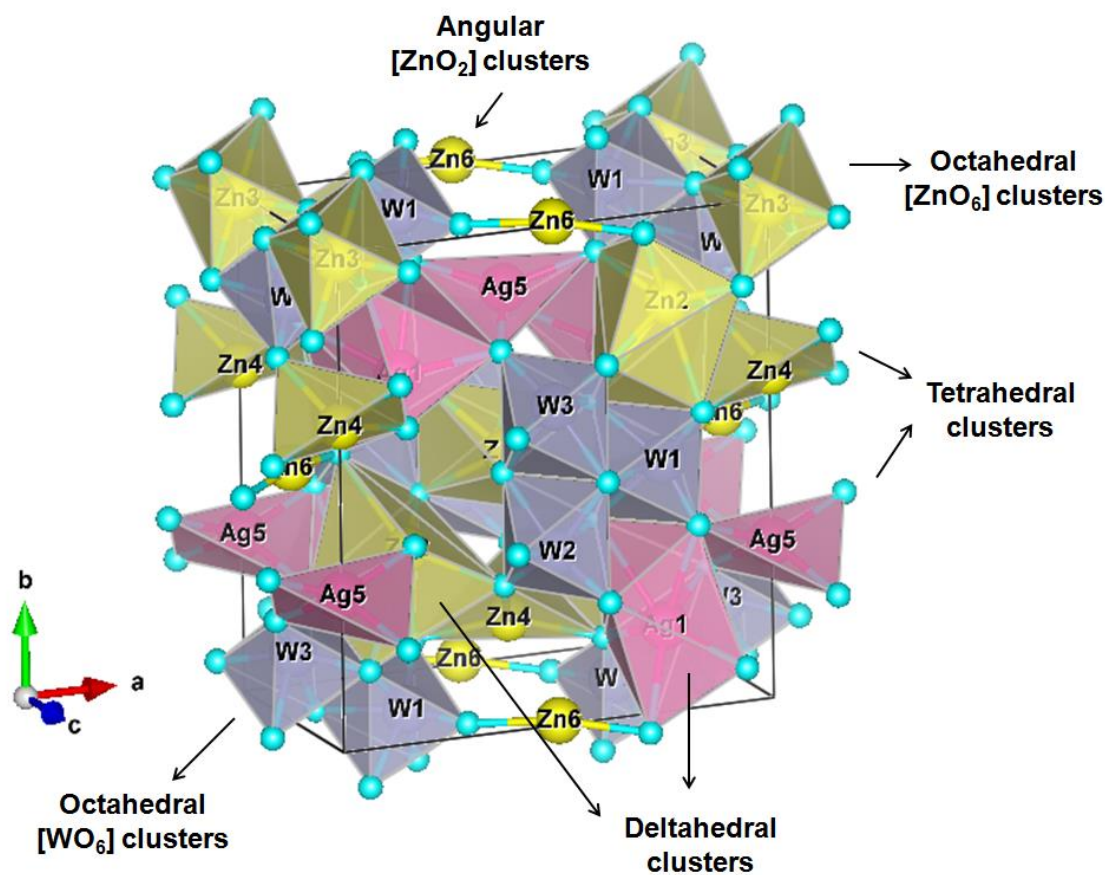


Figure 14: Schematic representation of crystalline units cells of $\alpha\text{Ag}_{2-2x}\text{Zn}_x\text{WO}_4$ ($x = 0.25$) microcrystals.

It is well-known [3,23,47] that $\alpha\text{-Ag}_2\text{WO}_4$ is composed of three different W sites (W1, W2, and W3), all coordinated with six oxygen atoms forming a distorted $[\text{WO}_6]$ cluster with an octahedral configuration. Six types of Ag sites with four different coordinations are presented (see Table 1): the Ag1 and Ag2 atoms are bonded with seven oxygen atoms generating a distorted bipyramidal $[\text{AgO}_7]$ clusters; already the Ag3 atoms are linked by six oxygen atoms that form the distorted octahedral $[\text{AgO}_6]$ cluster; for Ag4 and Ag5 atoms are arranged with four oxygen atoms, forming the distorted tetrahedral $[\text{AgO}_4]$ clusters; and finally the Ag6 atoms are coordinated by two oxygen atoms, which form an angular $[\text{AgO}_2]$ cluster. The Rietveld refinement technique allows for identifying possible sites of Zn^{2+} cation occupancies in the $\alpha\text{Ag}_{2-2x}\text{Zn}_x\text{WO}_4$ lattice. The substitution of Ag sites with Zn^{2+} cations represented through $[\text{AgO}_y]/[\text{ZnO}_y]$ ($y = 2, 4, 6, \text{ and } 7$) clusters was determined for $\alpha\text{-Ag}_{2-2x}\text{Zn}_x\text{WO}_4$ ($x = 0.10, 0.15, 0.20, \text{ and } 0.25$) solid solutions, and these are listed in Table 1 with their atomic occupation values.

The refinement results show that the Zn^{2+} cations occupy different sites in the α -

Ag_2WO_4 lattice. In the $\alpha\text{-Ag}_{2-2x}\text{Zn}_x\text{WO}_4$ ($x = 0.10$ and 0.15) samples, Zn cations occupy the Ag1 and Ag2 sites corresponding to $[\text{AgO}_7]$ and Ag6 sites of the $[\text{AgO}_2]$ clusters. For $\alpha\text{-Ag}_{2-2x}\text{Zn}_x\text{WO}_4$ ($x = 0.20$), the replacement takes place at these sites, as well as at the Ag4 site of the $[\text{AgO}_4]$ cluster. Finally, for $\alpha\text{-Ag}_{2-2x}\text{Zn}_x\text{WO}_4$ ($x = 0.25$), the substitutions occur in the Ag1, Ag2, Ag3, Ag4, and Ag6 sites of the $[\text{AgO}_y]$ ($y = 7, 7, 6, 4,$ and 2) clusters, respectively. With the increase in the amount of Zn^{2+} , there is a saturation of the substitution of Ag1, Ag2, and Ag6 sites, and the Zn^{2+} begins to occupy other sites first the Ag4 and then the Ag3 sites. The $[\text{ZnO}_y]$ ($y = 7, 6, 4,$ and 2) arrangements are represented, respectively, by distorted bipyramidal, tetrahedral, octahedral, and angular clusters.

The random occupations of the Zn^{2+} cations lead to distortions in the $\alpha\text{-Ag}_2\text{WO}_4$ lattice observed by the different values of bond lengths and angles. These structural differences result in electronic order–disorder effects that, consequently, influence the $\alpha\text{-Ag}_2\text{WO}_4$ material as a whole, which is confirmed mainly by the morphology and optical properties. The atomic Zn occupation values are illustrated in Table 1; however, to have greater accuracy of these values, another technique such as extended X-ray absorption fine structure (EXAFS) analysis is required.

Table 2 - Atomic Zn Occupation in Sites of $[\text{AgO}_y]$ a Clusters of the $\alpha\text{-Ag}_{2-2x}\text{Zn}_x\text{WO}_4$ b Microcrystals

Refined formula ($\square\text{-Ag}_{2-2x}\text{Zn}_x\text{WO}_4$)	Ag1 [AgO ₇]	Ag2 [AgO ₇]	Ag3 [AgO ₆]	Ag4 [AgO ₄]	Ag5 [AgO ₄]	Ag6 [AgO ₂]
x = 0.10 occupation	[ZnO ₇] 0.026	[ZnO ₇] 0.046	-	-	-	[ZnO ₂] 0.028
x = 0.15 occupation	[ZnO ₇] 0.031	[ZnO ₇] 0.058	-	-	-	[ZnO ₂] 0.062
x = 0.20 occupation	[ZnO ₇] 0.015	[ZnO ₇] 0.087	-	[ZnO ₄] 0.063	-	[ZnO ₂] 0.035
x = 0.25 occupation	[ZnO ₇] 0.022	[ZnO ₇] 0.078	[ZnO ₄] 0.022	[ZnO ₄] 0.074	-	[ZnO ₂] 0.048

3.2.4.4 Structural Theoretical Analysis for $\alpha\text{-Ag}_{2-2x}\text{Zn}_x\text{WO}_4$

The Rietveld results show that orthorhombic $\alpha\text{-Ag}_2\text{WO}_4$ presents a very complex structure with different kinds of $[\text{AgO}_y]$ clusters (where y can be 2, 4, 6, and 7) and that Zn^{2+} replacement can occur in any of these sites, depending on the Zn^{2+} concentration. To complement the experimental results and to study the effects of the presence of Zn^{2+} in the $\alpha\text{-Ag}_2\text{WO}_4$ structure, two theoretical models, namely, A and B, for $x = 0.25$ (stoichiometry coefficient) of Zn ions were selected, in which the Zn replacements and Ag vacancies were made considering the charge balance between the Ag^+ and Zn^{2+} cations. In model A, the

Ag2 sites were replaced by Zn²⁺ cations, while in model B, the replacement was on the Ag4 sites, and the vacancies were allocated near the substitution sites in both models.

The theoretical results indicated that the Zn²⁺ could be located in both Ag2 and Ag4 positions. However, the Zn replacement on the Ag4 site (model B) was 0.15 eV more stable than that in the Ag2 site (model A). The $\alpha\text{Ag}_{2-2x}\text{Zn}_x\text{WO}_4$ geometry showing the Zn additions and the Ag vacancy positions is depicted in figure SI-4.

An analysis of the changes provoked by the substitution by Zn reveals that all clusters undergo modifications, exhibiting new coordination numbers and oxygen vacancies, as summarized in Table 2.

Table 3 - Kinds of clusters present in the models after optimization

Structures	Ag clusters	Zn clusters	W clusters
$\alpha\text{-Ag}_2\text{WO}_4$	[AgO ₇] [AgO ₆] [AgO ₄] [AgO ₂]	–	[WO ₆]
ZnWO ₄	–	[ZnO ₆]	[WO ₆]
Model A	[AgO ₆] [AgO ₅] [AgO ₄]	[ZnO ₄]	[WO ₄]
Model B	[AgO ₅] [AgO ₄]	[ZnO ₄]	[WO ₅] [WO ₄]

Besides the structural distortion, the Zn replacement changes the $\alpha\text{-Ag}_2\text{WO}_4$ electronic structure with the creation of holes in the systems, which are responsible for changes in the electronic properties of the tungstate. Thus, the properties are not only functions of the shallow defects (distorted clusters), as in the case of the $\alpha\text{-Ag}_2\text{WO}_4$ structure, but also are functions of deeper defects (oxygen vacancies, V^x_O) in the clusters presented in $\alpha\text{-Ag}_{2-2x}\text{Zn}_x\text{WO}_4$ caused by the rearrangement of the oxygen atoms around the cations. Therefore, in the $\alpha\text{-Ag}_{2-2x}\text{Zn}_x\text{WO}_4$ solid solutions, there are [WO₅·V^x_O], [WO₄·2V^x_O], [ZnO₅·V^x_O], [ZnO₄·2V^x_O], and [AgO_x]^x_d distorted clusters that are responsible for the PL properties.

3.2.4.5 Micro-Raman Spectroscopy Analysis

Through the Raman it is possible to determine the structural order of the material.⁶⁴ In accordance with the literature [65] the $\alpha\text{-Ag}_2\text{WO}_4$ structure is classified into the internal and external modes, due to the weak coupling among group [WO₄]²⁻ and the Ag⁺ ion [66]. Thus, the internal modes are related to the vibrational molecular units, where the centers of mass remains immobile and the external mode refer to the lattice phonon, which is attributed to the motion of Ag⁺ ion [67].

Figure 15a illustrates the Raman spectra of $\alpha\text{-Ag}_{2-2x}\text{Zn}_x\text{WO}_4$ ($x = 0, 0.05, 0.10, 0.15, 0.20,$ and 0.25) microcrystals prepared at $80\text{ }^\circ\text{C}$ for 30 min by the CP method, and Figure 3b compares the experimental Raman vibrational modes of $\alpha\text{-Ag}_{2-2x}\text{Zn}_x\text{WO}_4$ microcrystals with the Raman-active modes calculated theoretically.

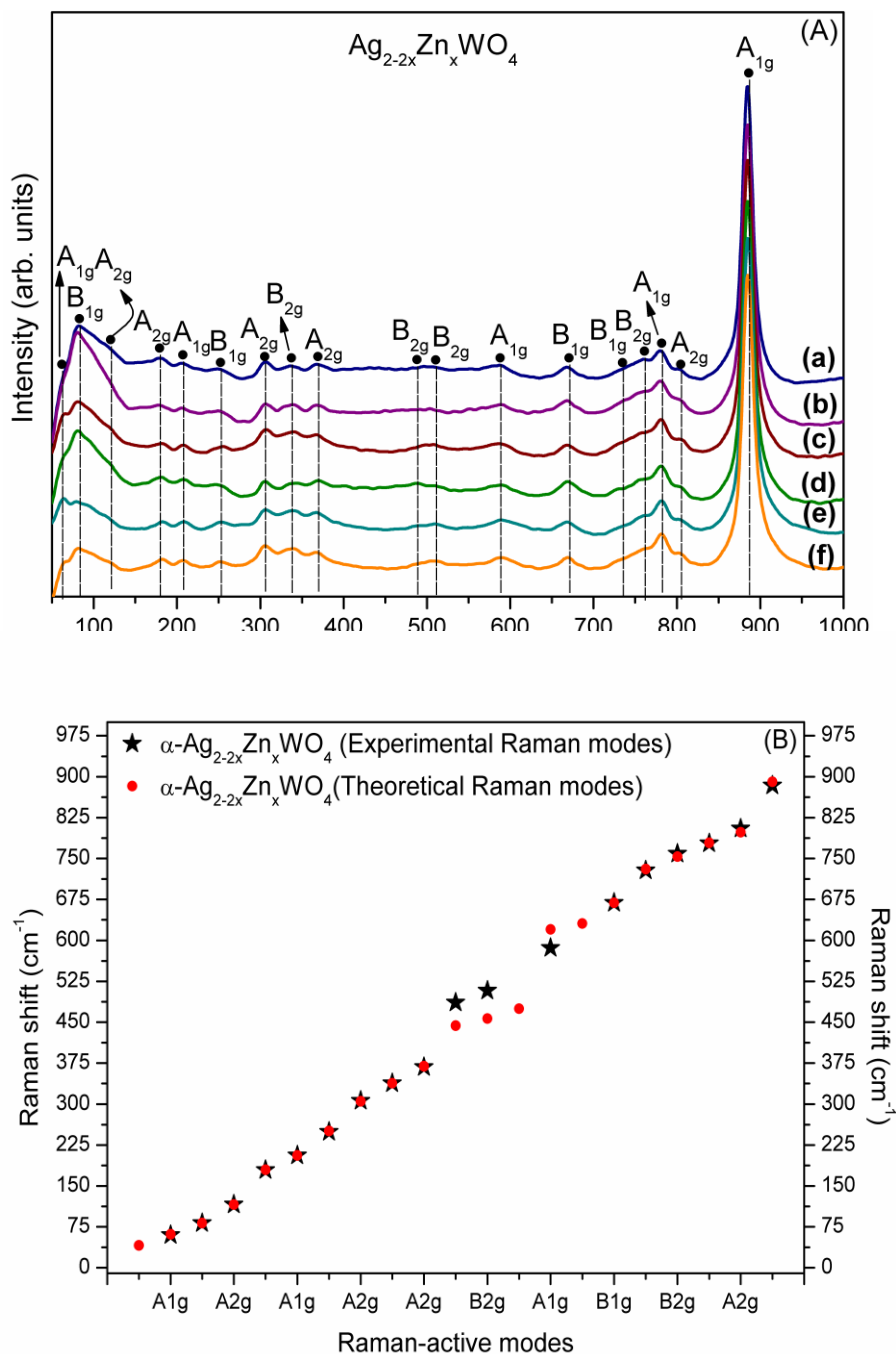


Figure 15: (a) Raman spectra of the $\alpha\text{-Ag}_{2-2x}\text{Zn}_x\text{WO}_4$ ($x =$ (a) 0, (b) 0.05, (c) 0.10, (d) 0.15, (e) 0.20, and (f) 0.25) microcrystals obtained by the CP method at $80\text{ }^\circ\text{C}$ for 30 min and (b) comparison between the relative positions of theoretical and experimental Raman-active modes of $\alpha\text{-Ag}_{2-2x}\text{Zn}_x\text{WO}_4$ microcrystals

In Table SI-5, a comparison is presented among the experimental and simulated Raman active modes of α -Ag₂WO₄ microcrystals and values reported in the literature [22, 23, 56, 68].

According to the literature [56], there are 21 different vibrational modes in the tungstate with an orthorhombic structure. However, as can be seen in Figure 15a, 18 well-defined Raman-active modes were detected. These modes can be associated with the symmetric and asymmetric stretching among O–W–O moieties inside the [WO₆] cluster, revealing peaks corresponding to the Raman-active internal modes A₁, A₂, B₁, and B₂, 5 while the modes located at lower energy represent the torsion among W–O and Ag–O situated in the 50–1000 cm⁻¹ range. All modes presented in Figure 3a are intense and well-defined, suggesting that all α -Ag_{2-2x}Zn_xWO₄ (x = 0, 0.05, 0.10, 0.15, 0.20, and 0.25) microcrystals are structurally ordered at short-range. However, it is important to note that several modes were not observed probably due to their small intensities.

In this work, the active mode located in lower energy corresponds to translational A_{1g} (60 cm⁻¹) mode, and this refers to external or lattice phonons due to the Ag⁺ heavycation movement in the rigid molecular unit. The strong interaction between the ions can cause an increase in the Raman-active mode intensity, and this occurs due to stretching and bending vibrations of shorter M–O bonds [69]. Thus, the intense peak at [884] cm⁻¹ is attributed to the A_{1g} mode caused by the symmetric stretching vibrations of [O←W→O] bonds of octahedral [WO₆] clusters [5,23], as opposed to the lattice modifier assigned to [AgO_y] (y = 2, 4, 6, and 7) clusters. Three Raman modes (A_{1g}, B_{2g}, and B_{1g}) were also not observed, probably due to their small intensities.

Figure 15a displays that the Raman spectra for these samples presented a small change, indicating that the addition of Zn²⁺ ions in α -Ag₂WO₄ does not cause drastic changes in the stretching, torsional, and bending vibrational modes of the orthorhombic structure. It occurs because of the Zn²⁺ substitutes the Ag⁺ cation; however, some variations were expected. For example, the intense peaks at ~884 cm⁻¹ show reductions in their intensities as the Zn²⁺ concentration is increased (see figure 15a), due to structural distortions in the α Ag_{2-2x}Zn_xWO₄ microcrystal lattice produced by the Zn²⁺ substitution on the Ag⁺ sites. These distortions also provoke changes in the bond lengths of the W–O distances in the [WO₆] clusters [23] The result is in accordance with the Rietveld data, where a

decrease in the cell volume as the concentration of Zn^{2+} was increased in the $\alpha\text{-Ag}_2\text{WO}_4$ lattice was observed. One way to assess the quality of the theoretical models is to compare the vibrational modes. Figure 3b displays the Raman modes of the experimental samples, represented by (\bullet), compared with our theoretical model (model B), illustrated as (\star). Both experimental and theoretical results are in accordance with the literature [5,20,22,23,56] (see Table SI-5). This fact indicates that our model provides an appropriate representation of the $\alpha\text{-Ag}_{2-2x}\text{Zn}_x\text{WO}_4$ solid solutions. A slight variation of some modes can be detected, mainly at 443.9, 456.7, and 474.9 cm^{-1} (Bg), which are associated with the stretching and bending vibrational modes of the Zn–O when compared with the experimental Raman modes (see Figure 3b and Table SI-5). This difference can be attributed to the different methods of synthesis, crystal size, and structural changes of bond distances Ag–O, W–O, and Zn–O, and bond angles Ag–W–O, Ag–W–Zn, along the $[\text{AgO}_y]\text{--}[\text{WO}_6]\text{--}[\text{AgO}_y]$ and $[\text{AgO}_y]\text{--}[\text{WO}_6]\text{--}[\text{ZnO}_y]$ ($y = 2, 4, 6, \text{ and } 7$) [20] frameworks.

3.2.4.6 FTIR Spectroscopy Analysis.

FTIR data obtained in the interval of 200–1000 cm^{-1} of the $\alpha\text{-Ag}_{2-2x}\text{Zn}_x\text{WO}_4$ ($x = 0, 0.05, 0.10, 0.15, 0.20, \text{ and } 0.25$) microcrystals synthesized by CP at 80 °C for 30 min are displayed in figure SI-5. Figure SI-5a–f presents the 14 IR-active vibrational modes assigned to the $[\text{WO}_4^{2-}]$ group, Ag–O and Zn–O bonds, and Zn–O–W bond angles. The samples exhibit two intense absorption bands at 874 and 821 cm^{-1} referring to bonds between the W–O–W and O–W–O antisymmetric stretching of the tetrahedral WO_4^{2-} group (see the inset in figure SI-5). The 317 and 295 cm^{-1} bands represent the IR-active vibrational internal modes associated with the symmetric bending vibrations and external modes attributed to the torsional within the WO_4^{2-} group, respectively.

Figure SI-5 shows that, for the samples with $x > 0.05$, there is a change in some modes of the W–O bonds and O–W–O bending, which can be observed in the range of 400–750 cm^{-1} . This behavior is due to distortions of the $[\text{AgO}_y]\text{--}[\text{WO}_6]\text{--}[\text{ZnO}_y]$ ($y = 2, 4, 6, \text{ and } 7$) clusters. Thus, the observed bands at 617 and 588 cm^{-1} are assigned to the bridging oxygen atoms in the W_2O_2 asymmetric stretching, with the latter related to a small shift to lower wavenumbers (cm^{-1}) for samples with $x = 0.20$ and 0.25 of Zn^{2+} ion substitution (see

Figure SI-5e, f). The vibrations of the O–W–O moiety also results in the active modes at 737 and 926 cm^{-1} , and in the W–O–W moiety the vibrations result in the mode at 671 cm^{-1} [47]. The absorption bands at 361 and 487 cm^{-1} can be attributed to nonsymmetric deformation modes of Zn–O bonds, and the absorption bands at 911 and 1051 cm^{-1} are related to the bending and stretching of the Zn–O–W framework [2,70]. FTIR spectra provided evidence that all $\alpha\text{-Ag}_{2-2x}\text{Zn}_x\text{WO}_4$ powders have an orthorhombic-type structure.

3.2.4.7 FE-SEM Morphological Analysis.

Figure 16a–r presents the morphologies and microstructures of the $\alpha\text{-Ag}_{2-2x}\text{Zn}_x\text{WO}_4$ ($x = 0, 0.05, 0.10, 0.15, 0.20,$ and 0.25) microcrystals obtained by CP at 80 $^\circ\text{C}$ for 30 min.

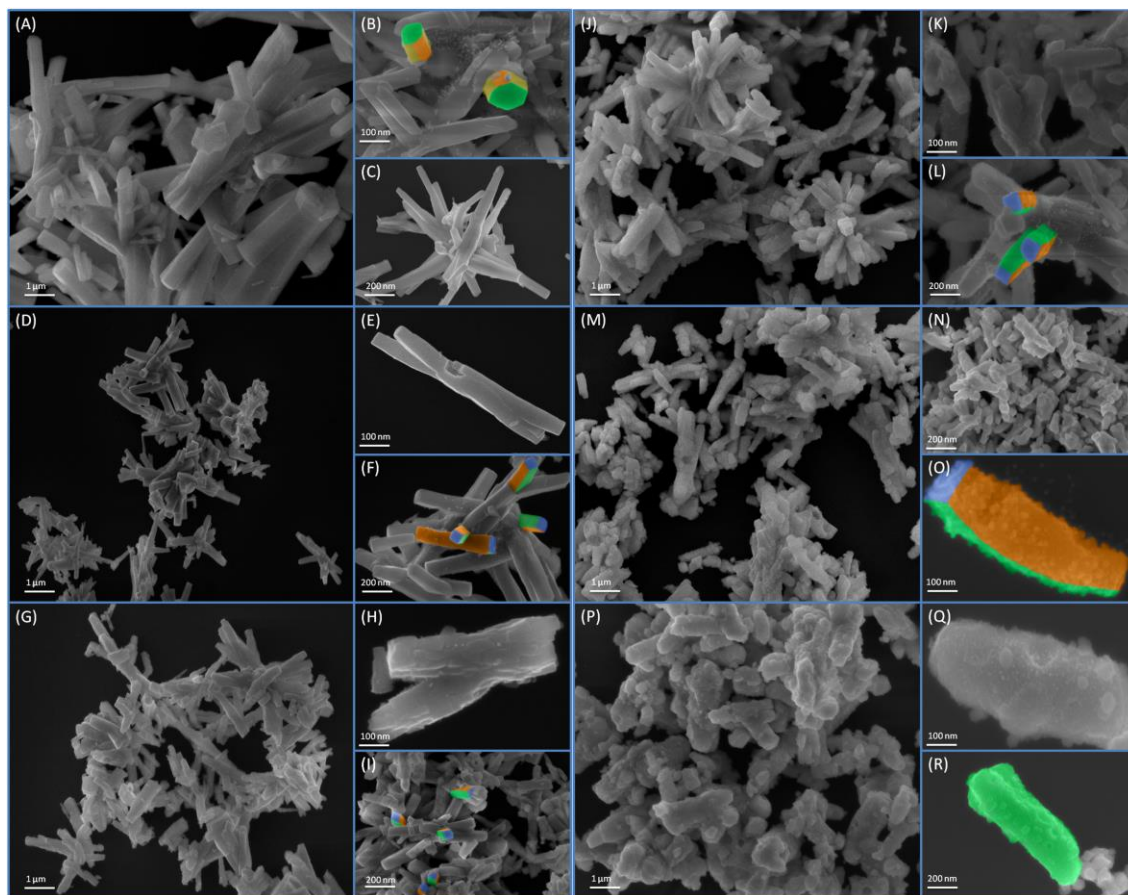


Figure 16: FE-SEM images of $\alpha\text{-Ag}_{2-2x}\text{Zn}_x\text{WO}_4$ (where (A–C) $x = 0$, (D–F) $x = 0.05$, (G–I) $x = 0.10$, (J–L) $x = 0.15$, (M–O) $x = 0.20$, and (P–R) $x = 0.25$) microcrystals, obtained by the CP method at 80 $^\circ\text{C}$ for 30 min

All samples are agglomerated with a polydisperse size distribution and shape (see

figure 16a–r), in accordance with our previous studies [3,17,47]. On the basis of the Wulff construction, it is possible to find surface energy ratios to achieve the same morphologies obtained experimentally [54,71,72]. However, this is a simple method that can be applied to show how the Zn^{2+} replacement influences the crystal morphology and, consequently, the materials properties (see figure SI-6). An analysis of the images for the $\alpha\text{-Ag}_2\text{WO}_4$ microcrystals displayed in Figure 16a–c shows several elongated rod-like structures, and it is possible to verify that $\alpha\text{-Ag}_2\text{WO}_4$ microcrystals present a well-defined face with a hexagonal shape (see Figure 16b) [3,17,47] It can be observed that some small $\alpha\text{-Ag}_2\text{WO}_4$ nanocrystals, as well as large $\alpha\text{-Ag}_2\text{WO}_4$ microcrystal surfaces, were not diffused within the interior. According to Cavalcante et al. [3], this behavior is because the partial diffusion of these small microcrystals through larger particles of $\alpha\text{-Ag}_2\text{WO}_4$ and/or that thermal energy that was not enough to the normal growth rate of the $\alpha\text{-Ag}_2\text{WO}_4$ microcrystals. According to Roca et al. [17] $\alpha\text{-Ag}_2\text{WO}_4$ microcrystals with a hexagonal rod-like shape have a preferential growth along the [010] direction. Coming from the vacuum structure previously obtained, the Wulff construction of the hexagonal rod-like shape can be obtained by destabilizing the (010) surface (increasing its energy) and stabilizing the (101) surface (decreasing the energy). The relative surface energies of this morphology are described in figure SI-6b.

In the solid solution with $x = 0.05$ of Zn^{2+} occurs a modification in the microcrystal shapes and sizes, as can be seen in figure 16d–f. These figures illustrate the formation of rod-like microcrystals with crystallographic face-squared shapes (see figure 16e, f). The average size of these particles is also smaller than the pure $\alpha\text{-Ag}_2\text{WO}_4$. Thus, the Wulff construction of this morphology was reached destabilizing the (001) surface and stabilizing the (100) surface (see figure SI-6c). It is worth mentioning that the elongation of these particles is provided by the decrease in the (001) surface energy in relation to the (100) and (010) surfaces. Therefore, this information allows one to know how the Zn^{2+} influences the particle growth, by providing a stabilization of the (101) surface with respect to the (100), (010), and (001) surfaces. The surface energy values in thermodynamic equilibrium can be found in figure SI-6c.

Figure 16g–i presents the $\alpha\text{-Ag}_{2-2x}\text{Zn}_x\text{WO}_4$ ($x = 0.10$) solid solution, where a similar behavior of $\alpha\text{-Ag}_{2-2x}\text{Zn}_x\text{WO}_4$ ($x = 0.05$) microcrystals is observed, and this can be proved through the Wulff construction (see Figure SI-6c); however, the microcrystals show a more rugose surface and a decrease in the average size (see Figure 16h).

Figure 16j–l shows the $\alpha\text{-Ag}_{2-2x}\text{Zn}_x\text{WO}_4$ ($x = 0.15$) microcrystals, which exhibit a rugose surface and face-quasisquared shape, while also showing a curved surface (see figure 16k, l). Finally, in the $\alpha\text{-Ag}_{2-2x}\text{Zn}_x\text{WO}_4$ ($x = 0.20$ and 0.25) microcrystals the Zn^{2+} caused a pronounced change in the microcrystals' shapes and sizes (see figures 16m, n, p–r), respectively, leading to the formation of deformed rod-like structures with curved surfaces.

In a general observation, the low concentration of Zn^{2+} initially induced the disappearance of the (101) surface at equilibrium, resulting in a tetrahedral morphology. Increasing the amount of Zn^{2+} ions, it was noticed that imperfections formed on the tetrahedral crystals, as observed in figure 16h, up to a point where the morphologies suffered a deconfiguration (see figure 16m–r). Therefore, the structural disorganization induced by Zn^{2+} on the lattice tends to hamper the atomic stacking at a superficial level, generating these observed changes.

Thus, figure 17 schematizes the growth mechanism, which leads to the formation of the $\alpha\text{-Ag}_{2-2x}\text{Zn}_x\text{WO}_4$ ($0 \leq x \leq 0.25$) microcrystals in comparison with FE-SEM micrographs. Initially, through the strong electrostatic attraction between the hydrated Ag^+ , Zn^{2+} and WO_4^{2-} clusters, the first nuclei are formed, and, consequently, the nucleation phase starts spontaneously with the formation of primary particles that lead the precipitation. Thus, the rapid nucleation step is followed by the uniform growth of the particles.

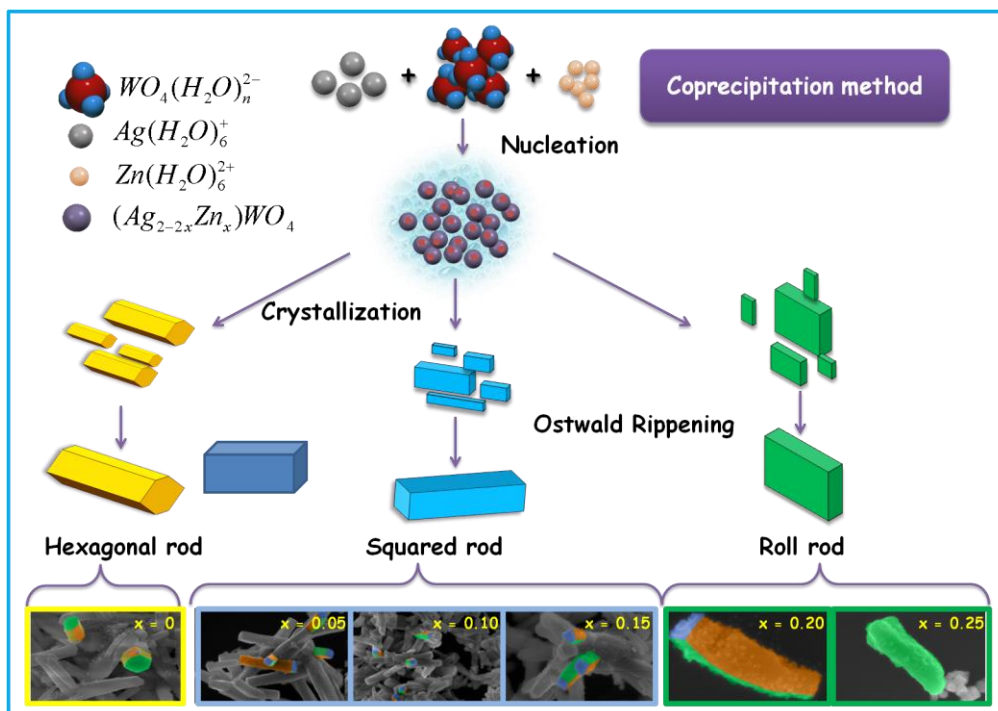


Figure 17: Schematic illustration of the proposed growth mechanism leading to the formation of α - $\text{Ag}_{2-2x}\text{Zn}_x\text{WO}_4$ ($0 \leq x \leq 0.25$) microcrystals

This process is called Ostwald ripening (OR), in which the system reaches an equilibrium condition between the solubility and precipitation processes. The OR process occurs when small particles in suspension redissolve and are deposited in larger particles. This OR process can happen in two steps: a very slow or fast nucleation step, leading to the formation of polydisperse or monodisperse particles, respectively [47,73]. When a change in the morphology is observed due to the addition of Zn^{2+} clusters and to the silver vacancies, there is a spontaneous formation of oxygen vacancies in the clusters that creates irregularities or surface defects in α - $\text{Ag}_{2-2x}\text{Zn}_x\text{WO}_4$ ($0.05 \leq x \leq 0.25$) microcrystals, indicating a polydisperse growth nature (see the morphology in the Figure 17 inset).

3.2.4.8 UV-Vis Absorption Spectroscopy Analysis and Band Structures of α - $\text{Ag}_{2-2x}\text{Zn}_x\text{WO}_4$ Microcrystals

The optical band gap energies (E_{gap}) of α - $\text{Ag}_{2-2x}\text{Zn}_x\text{WO}_4$ ($x = 0, 0.05, 0.10, 0.15, 0.20,$ and 0.25) microcrystals were calculated by the Wood-Tauc [74] method and Kubelka-Munk [75] function. The gap energy values were obtained through the equations discussed in previous Works [3,17,23,57,76]. According to the literature [77,78] the α -

Ag_2WO_4 microcrystals present a direct electronic transition. Additionally, on the basis of our theoretical calculations, the electronic transitions for the $\alpha\text{-Ag}_{2-2x}\text{Zn}_x\text{WO}_4$ ($0 \leq x \leq 0.25$) systems are governed by an indirect transition. This information was used for the band gap energy estimation in the Wood-Tauc method.

Table 4 presents the estimated band gap values for $\alpha\text{-Ag}_{2-2x}\text{Zn}_x\text{WO}_4$ ($x = 0, 0.05, 0.10, 0.15, 0.20, \text{ and } 0.25$) microcrystals obtained by CP at 80°C for 30 min. The UV-vis spectra of these samples are present in figure SI-7.

Table 4 - Optical Band Gap Energy (E_{gap}) Values to $\alpha\text{-Ag}_{2-2x}\text{Zn}_x\text{WO}_4^{\text{a}}$ Microcrystals Obtained by CP Method^b

$\alpha\text{-Ag}_{2-2x}\text{Zn}_x\text{WO}_4$	E_{gap} (eV)
x = 0	3.18
x = 0.05	3.04
x = 0.10	3.03
x = 0.15	3.07
x = 0.20	3.08
x = 0.25	3.08

^a $x = 0.00, 0.05, 0.10, 0.15, 0.20, \text{ and } 0.25$. ^bAt 80°C for 30 min

As observed in Table 4, the experimental E_{gap} values show a slight decrease as the presence of Zn^{2+} ions in the $\alpha\text{-Ag}_2\text{WO}_4$ lattice increases. The study of these electronic transitions can be evaluated through theoretical calculations. Therefore, figure 18a-c illustrates the band structures of pure $\alpha\text{-Ag}_2\text{WO}_4$, for model A and model B.

Typically, the introduction of impurities in the lattice tends to decrease band gap due to the creation of new intermediate levels [3,22,57] in the forbidden region, as also observed in our model as well. This tendency can occur not only because of the insertion of impurities but also by the disordered structure as structural defects at medium range, local bond distortions [57,68] $[\text{WO}_6]\text{-}[\text{WO}_6]$, $[\text{AgO}_y]\text{-}[\text{AgO}_y]$, or $[\text{WO}_6]\text{-}[\text{AgO}_y]$ [47] intrinsic surface states, and interfaces [17].

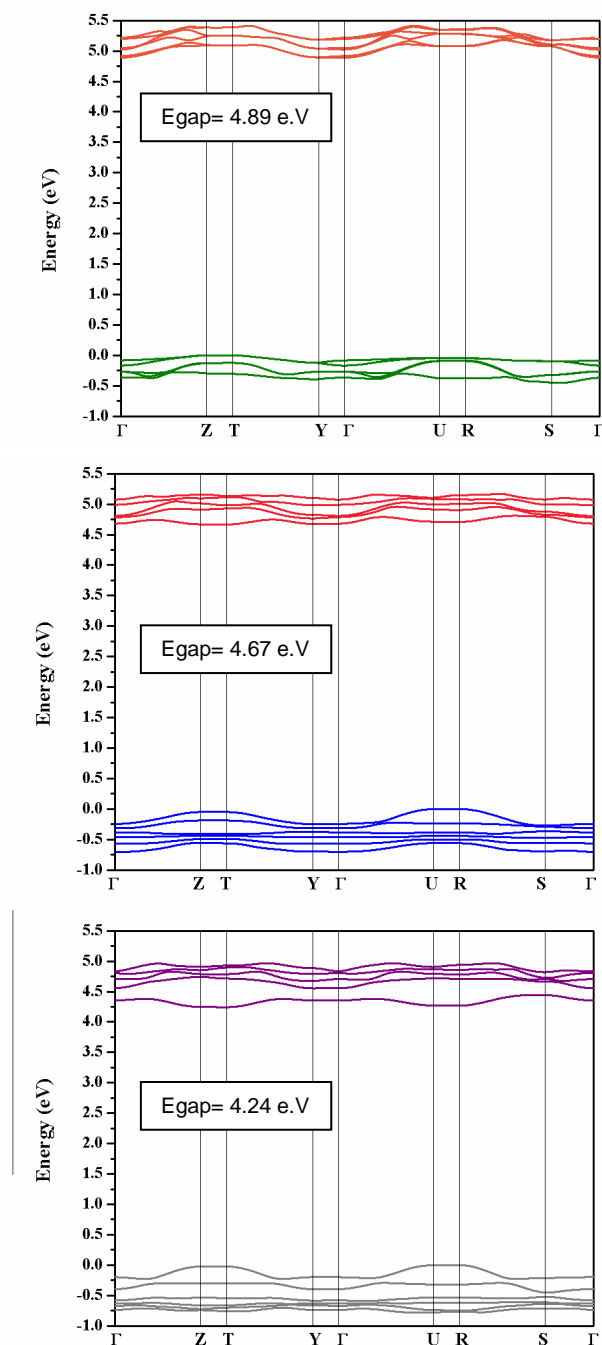


Figure 18: Band structure of (a) pure α -Ag₂WO₄, (b) model A, and (c) model B

By means of the band structure analysis, it was noticed that the pure α -Ag₂WO₄ and the two models with the Zn replacement are typically characterized by indirect electronic transitions. In the band structure of pure α -Ag₂WO₄, the top of the valence band (VB) is located at the T point, and the bottom of the conduction band (CB) is at the Γ point; in models A and B, the bottom of the CB is located at the T point, and the top of the VB is placed at the

U and R points, respectively. Even though the band gaps of the two models are similar, the indirect characteristic of the band gap was retained, although the change of U–T to R–T transition.

This result confirms that the location of the replacement (in the Ag2 site in model A; in the Ag4 site in model B) affects the transition energy. The comparison between the energies revealed that model B is more stable than model A. Additionally, this stability resulted in the reduction in the band gap value due to the modification of energy levels, which can be better evaluated by the DOS analysis.

3.2.4.9 Density of States

The DOS of pure α -Ag₂WO₄ and the two models were also studied to give information in relation to the electronic transitions. Figure 19 shows the total DOS for pure α -Ag₂WO₄ and the models with Zn replacement (models A and B). For all models, the projected DOS on the W atom is principally determined in the CB with 5d orbitals. The VB is mainly resulting from the hybridization of 2p and 4d orbitals from O and Ag atoms, respectively. The Zn atoms present a small contribution for both bands. When we analyze these results, it is possible to notice that the region of the band gap underwent an enlargement in both bands. This fact is linked with the kinds of defects that the Zn²⁺ replacement created in the α -Ag₂WO₄ bulk. There might be different defects in the structure; for example, shallow and deep defects. The first one is related to structural order–disorder effects, such as bond stretching or bond bending, whereas the deep defect is assigned to oxygen vacancies (V^{\times}_O).

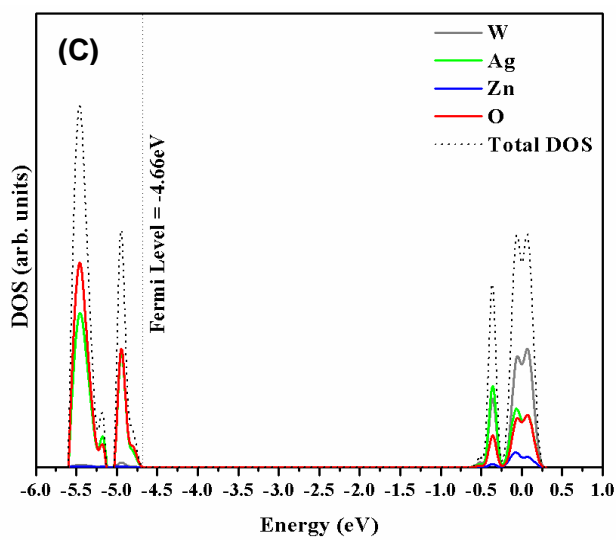
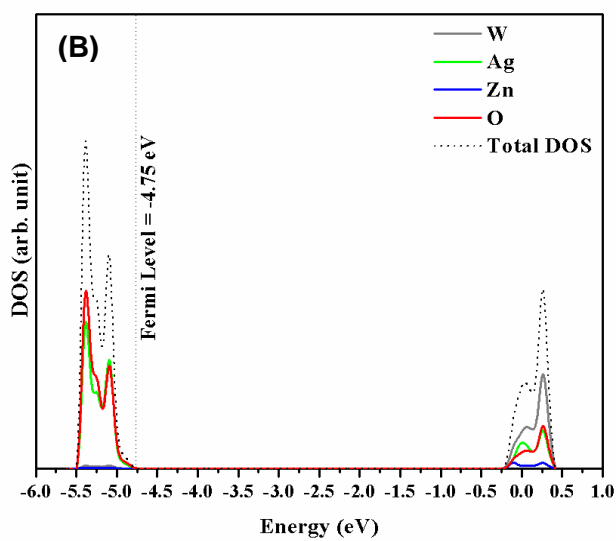
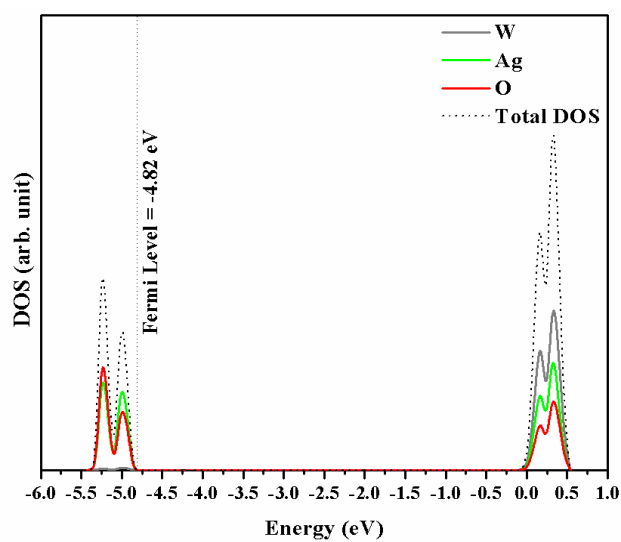


Figure 19: DOS projected in (a) pure α -Ag₂WO₄, (b) model A, and (c) model B.

When we induce the Zn^{2+} substitution in the theoretical models, changes in the α - Ag_2WO_4 bulk (pure model) were observed, mainly causing different types of clusters. These structural deformations and oxygen vacancies are present in $[AgO_y]$, $[ZnO_y]$ ($y = 2, 4, 6,$ and 7), and $[WO_6]$ clusters.

3.2.4.9 Photoluminescence

PL spectra of the α - $Ag_{2-2x}Zn_xWO_4$ ($x = 0, 0.05, 0.10, 0.15, 0.20,$ and 0.25) samples prepared by the CP method at $80\text{ }^\circ\text{C}$ for 30 min with a 350.7 nm excitation are shown in Figure 20. The PL studies are an important way to evaluate the electronic levels and to analyze the theoretical models.

Figure 20 shows the PL emissions from 350 to 850 nm for all of the samples. It is possible to observe a wide band with maximum intensity emission in the violet–blue range between 450 and 465 nm and another in the orange–red region between 606 and 690 nm, related to cluster-to-cluster charge transfer processes. All spectra present a wide band in the visible range, indicating that the emission is a multilevel process [22], involving the contribution of various energy states in the band gap [3,68].

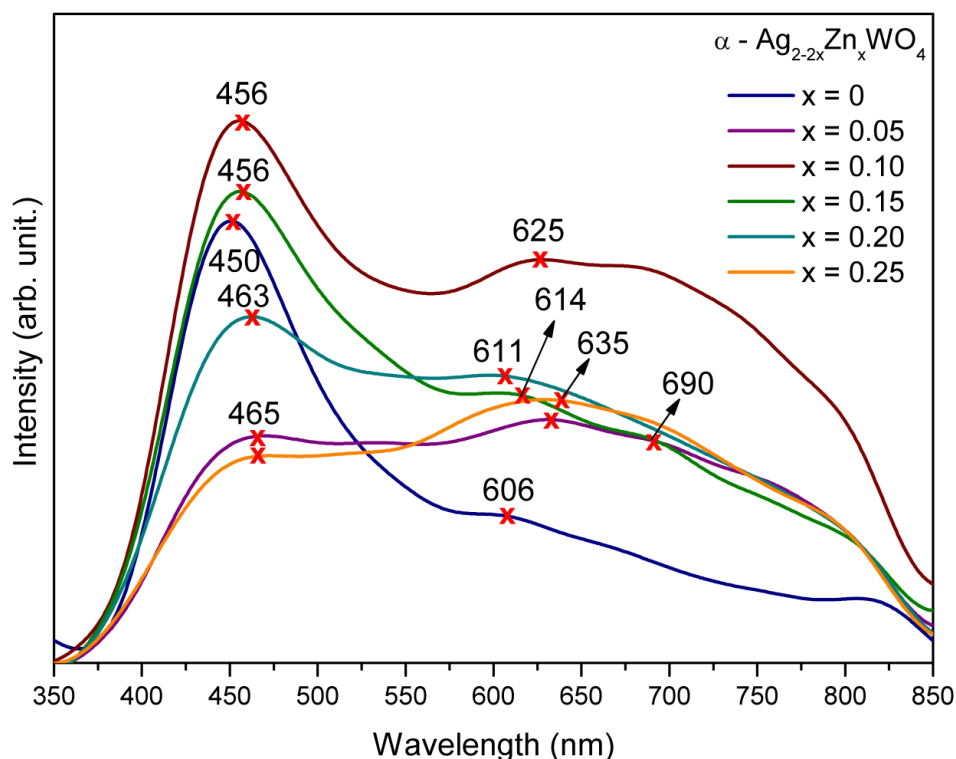


Figure 20: Emission spectra of the α - $Ag_{2-2x}Zn_xWO_4$ ($x =$ (a) 0, (b) 0.05, (c) 0.10, (d) 0.15, (e) 0.20, and (f) 0.25) microcrystals obtained by the CP method at $80\text{ }^\circ\text{C}$ for 30 min; excited at 350.7 nm with a krypton ion laser

Figure 20 illustrates the maximum blue PL emission peak of the α - Ag_2WO_4 sample, with the maximum intensity centered at 450 nm, possibly caused by electronic transitions in the octahedral $[\text{WO}_6]$ cluster. On the one hand, a red shift to 465 nm and a decrease in the intensity are observed. On the other hand, there is an increase of the red region emission from 600 to 800 nm in the samples with the Zn^{2+} ion addition in the α - Ag_2WO_4 lattice. This red shift of the maximum emission and the changes in the PL profile of the spectra observed in Figure 20 indicate that the $[\text{WO}_6]$ and $[\text{AgO}_y]$ clusters were influenced by distortions of the $[\text{AgO}_y]-[\text{WO}_6]-[\text{ZnO}_y]$ ($y = 2, 4, 6, \text{ and } 7$) bonds and also that there are clusters with oxygen vacancies (VO_x). This fact can be associated with the formation of new $[\text{ZnO}_y]$ clusters in the α - Ag_2WO_4 lattice, which are responsible for the different distribution of the energy levels within the band gap [47], confirming the substitution of Zn^{2+} on the Ag^+ site. To better understand the effect of Zn^{2+} in the α - $\text{Ag}_{2-2x}\text{Zn}_x\text{WO}_4$ lattice and its behavior on the PL properties, a deconvolution of each peak of the PL spectra was performed using the PickFit program with the Voight area function, as illustrated in figure 21.

Figure 21 presents that, through the deconvolution of the PL spectra, four curves at $\lambda = 441$ (blue), 491 (green), 630 (red), and 768 nm (orange) were possible to cover all of the visible electromagnetic spectrum. These results show a different behavior in each sample as the concentration of Zn^{2+} in the α - $\text{Ag}_{2-2x}\text{Zn}_x\text{WO}_4$ solid solutions was increased. However, these results reveal an elevated percentage of the red and orange area, indicating a higher amount of deep defects compared to shallow defects. This behavior is different from the pure α - Ag_2WO_4 sample, which favors the blue and green area, corresponding to shallow structural defects. These oscillations in the PL emissions corroborate with the Rietveld data, which show a random distribution of Zn^{2+} ions on the Ag^+ sites. The replacement of Ag^+ by Zn^{2+} in α - $\text{Ag}_{2-2x}\text{Zn}_x\text{WO}_4$ forms a complex structure with ionic bonds and, consequently, forms complexes with strong bonds. Thus, the substitutions occur in different clusters as the number of Zn^{2+} ions are increased, causing a red shift, which is linked to the increase in the amount of deep defects. These results were confirmed by theoretical models, where it was possible to notice different clusters of $[\text{ZnO}_5 \cdot \text{V}^x\text{O}]$, $[\text{ZnO}_4 \cdot 2 \text{V}^x\text{O}]$, $[\text{WO}_5 \cdot \text{V}^x\text{O}]$, $[\text{WO}_4 \cdot 2 \text{V}^x\text{O}]$, and $[\text{AgO}_y]$ ($y = 4, 5, \text{ and } 6$), as demonstrated in Section 3.4 (Structural Theoretical Analysis). When the Zn^{2+} ions are doped into α - Ag_2WO_4 , the red emission is favored, and it is linked to the deep defects, which are, in turn, linked to the oxygen vacancies presented in the clusters. In α - Ag_2WO_4 microcrystals, it is supposed that the Zn^{2+} ion replaces the Ag^+ ion. Thus, the

replacement of bivalent ion for a monovalent requires a charge balance of the lattice [67]. This behavior is expressed through eqs 1–4 [19].

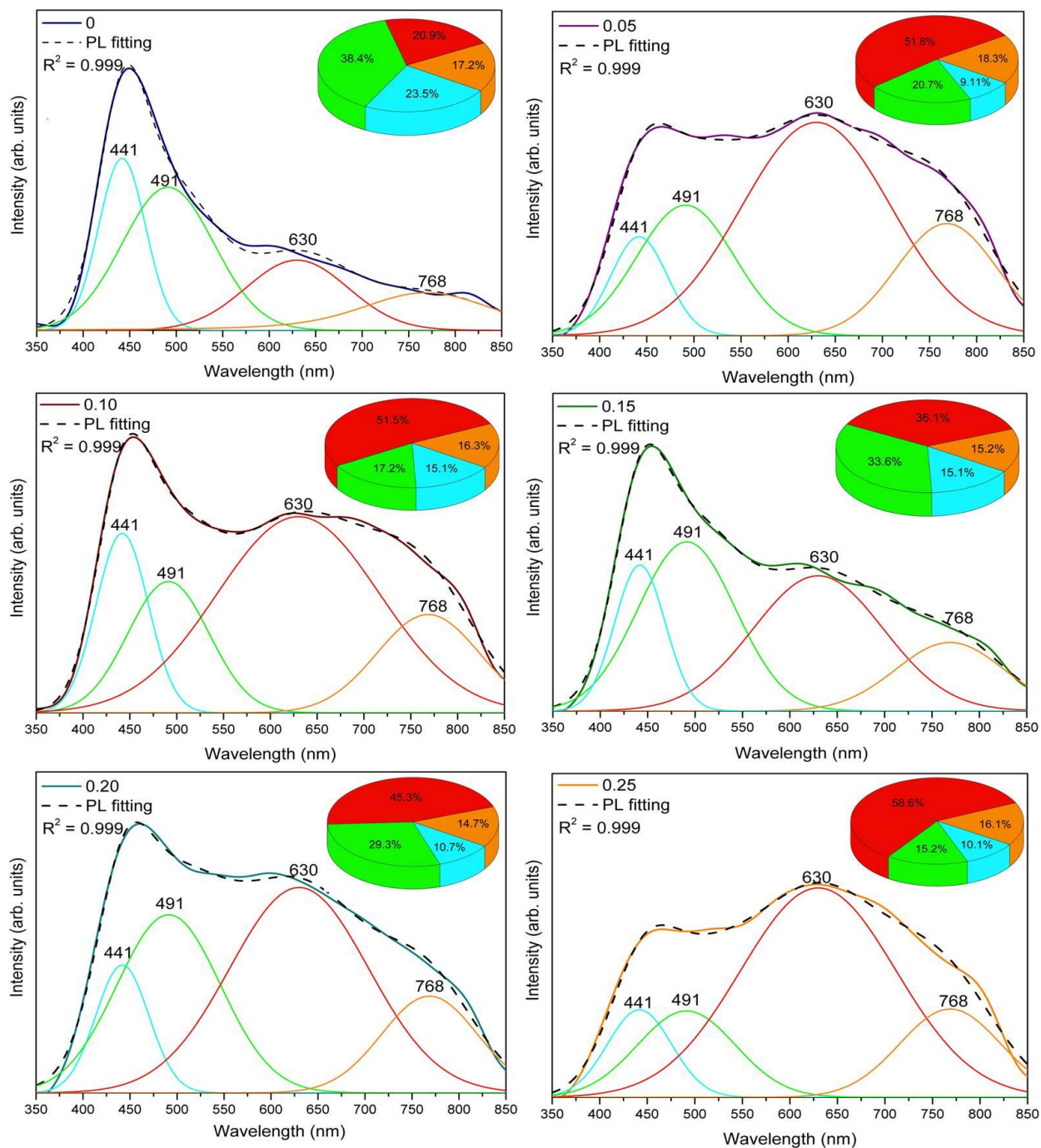
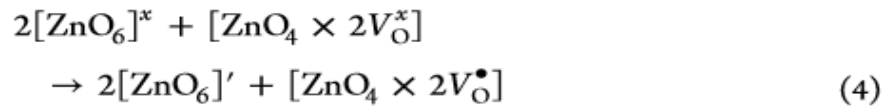
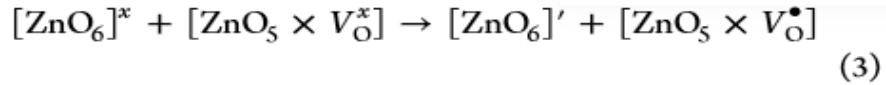
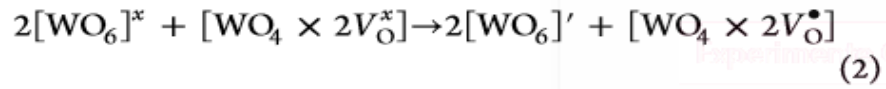
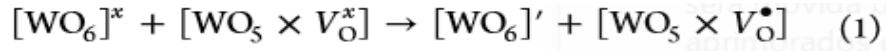


Figure 21: Deconvolution of PL spectra of $\alpha\text{-Ag}_2\text{-}2x\text{Zn}_x\text{WO}_4$ ($x =$ (a) 0, (b) 0.05, (c) 0.10, (d) 0.15, (e) 0.20, and (f) 0.25) microcrystals obtained by the CP method at 80 °C for 30 min. (insets) The area percentage of each color component corresponding to the emiss peak



The oxygen vacancies can be found in different charge states in the disordered lattice, such as $[\text{WO}_5 \cdot V_{\text{O}}^x]$, $[\text{WO}_4 \cdot 2V_{\text{O}}^x]$, $[\text{ZnO}_5 \cdot V_{\text{O}}^x]$, and $[\text{ZnO}_4 \cdot 2V_{\text{O}}^x]$, where these donate electrons and are neutral relative to the lattice. $[\text{WO}_5 \cdot V_{\text{O}}^\bullet]$, $[\text{WO}_4 \cdot 2V_{\text{O}}^\bullet]$, $[\text{ZnO}_5 \cdot V_{\text{O}}^\bullet]$, and $[\text{ZnO}_4 \cdot 2V_{\text{O}}^\bullet]$ are singly ionized states and donate and capture electrons, while $[\text{WO}_5 \cdot V_{\text{O}}^{\bullet\bullet}]$, $[\text{WO}_4 \cdot 2V_{\text{O}}^{\bullet\bullet}]$, $[\text{ZnO}_5 \cdot V_{\text{O}}^{\bullet\bullet}]$, and $[\text{ZnO}_4 \cdot V_{\text{O}}^{\bullet\bullet}]$ are doubly positively charged states in the lattice and capture electrons. Thus, these oxygen vacancies generate new energy states into the band gap, being attributed to $[\text{WO}_6]$, $[\text{AgO}_y]$, or $[\text{ZnO}_y]$ complex clusters [67].

3.2.5 Conclusion

In summary, $\alpha\text{-Ag}_{2-2x}\text{Zn}_x\text{WO}_4$ ($0 \leq x \leq 0.25$) solid solutions crystals were synthesized successfully by the CP method and, for first time, the introduction of Zn^{2+} ions to control the crystal characteristics and optical properties was investigated. XRD patterns and Rietveld refinement data showed that the $\alpha\text{-Ag}_{2-2x}\text{Zn}_x\text{WO}_4$ ($0 \leq x \leq 0.25$) microcrystals were monophasic with orthorhombic structure and space group $\text{Pn}2\text{n}$ and showed that Zn replacement occurred randomly in Ag sites in the $\alpha\text{-Ag}_2\text{WO}_4$ structure, depending on the Zn concentration. Thus, structural theoretical analysis based on first-principles calculations showed that Zn replacement in $\alpha\text{-Ag}_2\text{WO}_4$ structure is more favorable on the Ag4 site (tetracoordinated). MR and FTIR spectroscopies were employed to evaluate the vibrational modes, and the results have confirmed that all vibrational modes are characteristic of the orthorhombic structure.

The addition of Zn^{2+} ions in $\alpha\text{-Ag}_2\text{WO}_4$ was unable to modify the stretching, torsional, and bending active vibrational modes. The theoretical values of the Raman spectra are in agreement with previously reported values and the experimental results.

FE-SEM images revealed that the incorporation of Zn^{2+} in the $\alpha\text{-Ag}_2\text{WO}_4$ structure affected the shape and size of the microcrystals. On the basis of the Wulff's theorem and theoretical results, a model was elaborated to determine the surface energies of the $\alpha\text{-Ag}_2\text{WO}_4$ crystals with atomic-level resolution and the crystal morphologies at equilibrium. Particle shape transformations of the $\alpha\text{-Ag}_2\text{WO}_4$ were estimated by controlling the ratio between surface energy values of each face. The Ag substitution by Zn decreased the number of exposed surfaces, and the shape changed from roll-like to curved surfaces in $\alpha\text{-Ag}_2\text{WO}_4$ and $\alpha\text{-}\alpha\text{-Ag}_{2-2x}\text{Zn}_x\text{WO}_4$ ($x = 0.25$), respectively. The UV-vis spectrum indicated that, for $\alpha\text{-Ag}_2\text{WO}_4$ microcrystals and $\alpha\text{-}\alpha\text{-Ag}_{2-2x}\text{Zn}_x\text{WO}_4$, the band gap value was governed by an indirect transition.

The PL behavior of the $\alpha\text{-Ag}_2\text{WO}_4$ microcrystals was associated with structural rearrangements, provoked by the order-disorder effects on $[\text{WO}_6]_o$ x - $[\text{WO}_6]_d$ and $[\text{AgO}_y]_o$ x - $[\text{AgO}_y]_d$ ($y = 2, 4, 6, \text{ and } 7$) clusters. These effects are linked to shallow defects, resulting

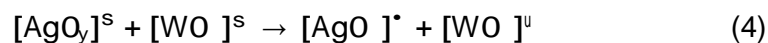
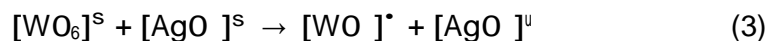
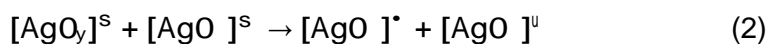
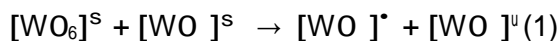
in a higher percentage of the blue region contribution in the PL profile. In the α - $\text{Ag}_{2-2x}\text{Zn}_x\text{WO}_4$ ($0.05 \leq x \leq 0.25$) microcrystals, the PL is associated with distortion and oxygen vacancies (V^{\times}_O) in these clusters causing a red shift, which is linked to an increase in the amount of deep defects.

SUPPORTING INFORMATION DESCRIPTION

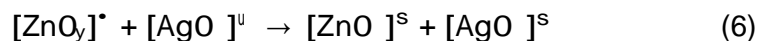
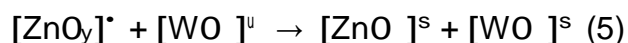
Photoluminescence: The α - Ag_2WO_4 crystals consist of $[\text{WO}_6]$ and $[\text{AgO}_y]$ ($y = 2, 4, 6,$ and 7) clusters in the lattice; thus, the $[\text{WO}_6]$ clusters are linked by strong bonds $[-\text{W}-\text{O}-\text{W}-]$ between the clusters, resulting in internal vibrational spectra that provide information on the structure and order-disorder effects in the framework. If a symmetry break occurs, it can induce the formation of different structures with different properties and, consequently, can modify the electronic levels of the materials and significantly influence the PL emission properties.

In general, it is assumed that the PL emissions of metal tungstates are related to the charge-transfer transitions within the distortions in tetrahedral $[\text{WO}_4]$ clusters or are due to oxygen vacancies or surface defects.^{1,2} Thus, this cluster-to-cluster charge transfer (CCCT) process in the α - Ag_2WO_4 crystals is characterized by excitations involving electronic transitions between the distorted $[\text{W}^{\text{s}}]$ – $[\text{W}^{\text{s}}]$ and $[\text{Ag}^{\text{s}}]$ – $[\text{AgO}_y]^{\text{s}}$ ($y = 2, 4, 6,$ and 7) clusters.¹⁻³ The blue–green emission of tungstate is due to the charge transfer transitions within the $[\text{WO}_6]$ cluster, and the emission in the red region is likely due to the $[\text{AgO}_y]$ ($y = 2, 4, 6,$ and 7) clusters, which form vacancies, inducing more disorder and deeper defects in the forbidden band gap; thus, the PL emission peaks situated at longer wavelengths were related to deep-level defects due to distortions in the lattice modifier clusters $[\text{AgO}_y]$ ($y = 2, 4, 6,$ and 7).^{2,4}

The PL emission behavior of α - $\text{Ag}_{2-2x}\text{Zn}_x\text{WO}_4$ can be explained through equations (1–4) below, according to the notation of Kröger–Vink.⁵ The electron–hole ($e'-h^\bullet$) pairs can be created before the electrons achieve the system. The structural distortions in $[\text{WO}_6]^{\text{s}}$ – $[\text{AgO}_y]^{\text{s}}$ (intrinsic defects) are able to polarize the structure and make electronic transitions between $[\text{WO}_6]^{\text{s}} / [\text{AgO}_y]^{\text{s}}$ and $[\text{W}^{\text{s}}] / [\text{Ag}^{\text{s}}]$ (disordered and ordered neutral clusters, respectively). Thus, when the photon energy is finally absorbed by the crystal, electron transitions to the conduction band occur and, subsequently, the relaxation of the network causes photons to be emitted. The superscript x indicates neutral clusters, \bullet present clusters with one hole (positive charge, h^\bullet), and $'$ indicates clusters with one electron (negative charge, e').



The equations (1–4) show the formation of e^- - h^+ pairs in the α - Ag_2WO_4 lattice due to ordered and disordered $[\text{WO}_6]^s / [\text{WO}]^s$, $[\text{AgO}]^s / [\text{AgO}]^s$, and $[\text{WO}_6]^s / [\text{AgO}]^s$ neutral clusters, consequently promoting the blue–green emission, thus leading to the generation of shallow defects (see Figure 12) as explained above and expressed through equations (5) and (6).



The suppression of the blue–green emission occurs in equation (5), in which the $[\text{WO}]^u$ clusters (donors) transfer their electrons to $[\text{ZnO}]^*$ clusters (acceptors), resulting in neutral clusters. The $[\text{ZnO}_y]^*$ new clusters act as networks modifiers contributing to the recombination of e^- - h^+ pairs.

Tables

Table SI-1. X-ray fluorescence of the chemical analysis of zinc-doped in α - $\text{Ag}_{2-2x}\text{Zn}_x\text{WO}_4$ ($0.05 \leq x \leq 0.25$) obtained by CP method at 80 °C for 30 min.

Samples	Theoretical (mol) for Ag^+	Experimental XRF (mol) for Ag^+	Theoretical (mol) for Zn^{2+}	Experimental XRF (mol) for Zn^{2+}
α - $\text{Ag}_{1.90}\text{Zn}_{0.05}\text{WO}_4$	1.90	1.98	0.05	0.08
α - $\text{Ag}_{1.80}\text{Zn}_{0.10}\text{WO}_4$	1.80	1.80	0.10	0.14
α - $\text{Ag}_{1.70}\text{Zn}_{0.15}\text{WO}_4$	1.70	1.83	0.15	0.18
α - $\text{Ag}_{1.60}\text{Zn}_{0.20}\text{WO}_4$	1.60	1.71	0.20	0.22
α - $\text{Ag}_{1.50}\text{Zn}_{0.25}\text{WO}_4$	1.50	1.44	0.25	0.28

Table SI-2. Lattice parameters, unit cell volume and statistical parameters of quality obtained by Rietveld refinement for the $\alpha\text{-Ag}_{2-2x}\text{Zn}_x\text{WO}_4$ ($x = 0, 0.05, 0.10, 0.15, 0.20$ and 0.25 mol) microcrystals synthesized by CP method at $80\text{ }^\circ\text{C}$ for 30 min.

Refined formula ($\alpha\text{-Ag}_{2-2x}\text{Zn}_x\text{WO}_4$)	Lattice Parameters			Cell	R_{Bragg} (%)	χ^2 (%)	R_{wp} (%)	R_{p} (%)
	volume a (Å)	b (Å)	c (Å)	(Å ³)				
x = 0	10.8868(5)	12.0399(7)	5.9071(1)	774.28(9)	1.78	1.90	9.83	7.73
x = 0.05	10.8637(9)	12.0246(2)	5.8998(3)	770.71(4)	2.17	1.71	8.40	6.43
x = 0.10	10.8660(5)	12.0286(0)	5.9005(2)	771.21(9)	1.57	1.77	8.57	6.37
x = 0.15	10.8543(8)	12.0176(6)	5.8943(2)	768.88(2)	1.60	1.83	8.59	6.26
x = 0.20	10.8502(6)	12.0190(6)	5.8953(1)	768.80(7)	2.23	2.09	9.71	7.50
x = 0.25	10.8421(3)	12.0138(7)	5.8963(6)	768.03(8)	2.15	2.01	9.65	7.44
ICSD N° 4165	10.89(2)	12.03(2)	5.92(2)	775.56	-	-	-	-

Table SI-3. Atomic positions of the $\alpha\text{-Ag}_{2-2x}\text{Zn}_x\text{WO}_4$ ($x = 0, 0.05$ and 0.10) samples.

$\alpha\text{-Ag}_{2-2x}\text{Zn}_x\text{WO}_4$									
Atom	$x = 0$			$x = 0.05$			$x = 0.10$		
	x	y	z	x	y	z	x	y	z
W1	0.2592(1)	-0.0054(5)	0.5233(4)	0.2564(9)	-0.0050(5)	0.5187(6)	0.2577(2)	-0.0039(5)	0.5228(3)
W2	0.000	0.8420(4)	0.500	0.000	0.8446(2)	0.500	0.000	0.8435(4)	0.500
W3	0.000	0.1325(4)	0.500	0.000	0.1397(4)	0.500	0.000	0.1340(4)	0.500
Ag1	0.7605(8)	0.1768(3)	0.9906(6)	0.7550(7)	0.1659(9)	0.9847(1)	0.7664(7)	0.1751(5)	0.9899(3)
Ag2	0.2445(8)	0.8233(3)	0.0121(6)	0.2380(8)	0.8168(3)	0.0137(5)	0.2504(7)	0.8216(5)	0.0114(3)
Ag3	0.000	0.9929(3)	0.000	0.000	0.9951(6)	0.000	0.000	0.9912(5)	0.000
Ag4	0.000	0.6588(3)	0.000	0.000	0.6591(7)	0.000	0.000	0.6571(5)	0.000
Ag5	0.000	0.3205(3)	0.000	0.000	0.3139(3)	0.000	0.000	0.3188(4)	0.000
Ag6	0.000	0.5149(3)	0.500	0.000	0.5084(2)	0.500	0.000	0.5132(5)	0.500
O1	0.3570(9)	0.5929(8)	0.1800(6)	0.3641(7)	0.5987(8)	0.1959(6)	0.3669(5)	0.6008(6)	0.1811(9)
O2	0.3570(9)	0.3589(8)	0.1730(6)	0.3796(4)	0.3781(1)	0.1703(2)	0.3669(5)	0.3668(6)	0.1741(9)
O3	0.4080(9)	0.7159(8)	0.8000(6)	0.4133(7)	0.7307(1)	0.8107(8)	0.4179(5)	0.7238(6)	0.8011(9)
O4	0.4140(9)	0.2439(8)	0.7770(6)	0.3863(2)	0.2747(4)	0.7945(7)	0.4239(5)	0.2518(6)	0.7781(9)
O5	0.1510(9)	0.4749(8)	0.2670(6)	0.1648(8)	0.4706(7)	0.2696(0)	0.1609(5)	0.4828(6)	0.2681(9)
O6	0.4030(9)	0.4769(8)	0.8320(6)	0.4158(4)	0.4827(7)	0.8439(1)	0.4129(5)	0.4848(6)	0.8331(9)
O7	0.1780(9)	0.5929(8)	0.8420(6)	0.1970(2)	0.6092(2)	0.8199(7)	0.1879(5)	0.6008(6)	0.8431(9)
O8	0.1820(9)	0.3599(8)	0.8850(6)	0.1919(1)	0.4081(4)	0.9378(1)	0.1919(5)	0.3678(6)	0.8861(9)
Zn1	-	-	-	-	-	-	0.7664(7)	0.1751(5)	0.9899(3)
Zn2	-	-	-	-	-	-	0.2504(7)	0.8216(5)	0.0114(3)
Zn3	-	-	-	-	-	-	0.000	0.9912(5)	0.000
Zn4	-	-	-	-	-	-	0.000	0.6571(5)	0.000
Zn5	-	-	-	-	-	-	0.000	0.3188(4)	0.000
Zn6	-	-	-	-	-	-	0.000	0.5132(5)	0.500

Table SI-4. Atomic positions of the α -Ag_{2-2x}Zn_xWO₄ (x = 0.15, 0.20 and 0.25) samples.

α -Ag _{2-2x} Zn _x WO ₄									
Atom	x = 0.15			x = 0.20			x = 0.25		
	x	y	z	x	y	z	x	y	z
W1	0.2576(2)	-0.0038(1)	0.5247(8)	0.2597(0)	0.0016(1)	0.5259(0)	0.2621(3)	0.0021(4)	0.5295(7)
W2	0.000	0.8436(8)	0.500	0.000	0.8491(1)	0.500	0.000	0.8496(4)	0.500
W3	0.000	0.1341(8)	0.500	0.000	0.1396(1)	0.500	0.000	0.1401(4)	0.500
Ag1	0.7674(6)	0.1748(9)	0.9892(5)	0.7464(5)	0.1694(1)	0.9896(2)	0.7458(2)	0.1688(3)	0.9879(8)
Ag2	0.2414(6)	0.8213(9)	0.0107(5)	0.2304(5)	0.8159(1)	0.0111(2)	0.2298(2)	0.8153(3)	0.0094(8)
Ag3	0.000	0.9909(5)	0.000	0.000	0.9855(1)	0.000	0.000	0.9849(3)	0.000
Ag4	0.000	0.6568(9)	0.000	0.000	0.6514(1)	0.000	0.000	0.6508(3)	0.000
Ag5	0.000	0.3185(9)	0.000	0.000	0.3131(1)	0.000	0.000	0.3125(3)	0.000
Ag6	0.000	0.5129(9)	0.500	0.000	0.5075(1)	0.500	0.000	0.5069(3)	0.500
O1	0.3679(8)	0.6047(2)	0.1767(7)	0.3760(7)	0.6209(7)	0.1777(4)	0.3803(6)	0.6249(7)	0.1757(3)
O2	0.3679(8)	0.3707(2)	0.1697(7)	0.3760(7)	0.3869(7)	0.1707(4)	0.3803(6)	0.3909(7)	0.1687(3)
O3	0.4189(8)	0.7277(2)	0.7967(7)	0.4270(7)	0.7439(7)	0.7977(4)	0.4313(6)	0.7479(7)	0.7957(3)
O4	0.4249(8)	0.2557(2)	0.7737(7)	0.4330(7)	0.2719(7)	0.7747(4)	0.4373(6)	0.2759(7)	0.7727(3)
O5	0.1619(8)	0.4867(2)	0.2637(7)	0.1700(7)	0.5029(7)	0.2647(3)	0.1743(6)	0.5069(7)	0.2627(3)
O6	0.4139(8)	0.4867(2)	0.8320(6)	0.4220(7)	0.5049(7)	0.8397(4)	0.4263(6)	0.5089(7)	0.8277(3)
O7	0.1889(8)	0.6047(2)	0.8420(6)	0.1970(7)	0.6209(7)	0.8397(4)	0.2013(6)	0.6249(7)	0.8377(3)
O8	0.1929(8)	0.3717(2)	0.8817(7)	0.2010(7)	0.3879(7)	0.8827(3)	0.2053(6)	0.3919(7)	0.8807(3)
Zn1	0.7674(6)	0.1748(9)	0.9892(5)	0.7464(5)	0.1694(1)	0.9896(2)	0.7458(2)	0.1688(3)	0.9879(8)
Zn2	0.2414(6)	0.8213(9)	0.0107(5)	0.2304(5)	0.8159(1)	0.0111(2)	0.2298(2)	0.8153(3)	0.0094(8)
Zn3	0.000	0.9909(5)	0.000	0.000	0.9855(1)	0.000	0.000	0.9849(3)	0.000
Zn4	0.000	0.6568(9)	0.000	0.000	0.6514(1)	0.000	0.000	0.6508(3)	0.000
Zn5	0.000	0.3185(9)	0.000	0.000	0.3131(1)	0.000	0.000	0.3125(3)	0.000
Zn6	0.000	0.5129(9)	0.500	0.000	0.5075(1)	0.500	0.000	0.5069(3)	0.500

Table SI-5. Raman modes (in cm^{-1}) of $\alpha\text{-Ag}_{2-2x}\text{Zn}_x\text{WO}_4$ ($x = 0, 0.05, 0.10, 0.15, 0.20$ and 0.25) microcrystals obtained by the CP method at $80\text{ }^\circ\text{C}$ for 30 min, compared to the literature.

Mode	This work		Literature values			
	Experimental	Theoretical	Turkovic et al. ⁶	Sreedevi et al. ⁷	Prasad et al. ⁸	Longo et al. ⁹ (theo.)
A _{1g}	-	41.3	44	-	-	40.4
A _{1g}	60	61.3	60	70	59	54.1
B _{1g}	82	81.7	92	-	81	87.0
A _{2g}	116	116.1	116	103	114	112.2
A _{2g}	179	179.6	182	175	179	152.4
A _{1g}	206	205.7	208	205	204	212.4
B _{1g}	249	250.6	248	246	249	246.2
A _{2g}	306	304.9	306	301	301	308.6
B _{2g}	338	338.4	336	335	-	329.6
A _{2g}	368	369.4	366	361	365	369.5
B _{2g}	486	443.9	488	475	-	450.8
B _{2g}	508	456.7	510	504	-	523.4
B _{2g}	-	474.9	546	544	-	564.2
A _{1g}	586	620.0	590	588	584	599.4
B _{1g}	-	631.1	629	624	-	628.6
B _{1g}	669	668.8	667	664	662	662.8
B _{1g}	728	730.8	730	722	-	712.7
B _{2g}	759	753.5	754	742	755	716.6
A _{1g}	778	778.9	778	773	777	809.0
A _{2g}	805	798.2	800	791	801	813.5
A _{1g}	884	890.6	884	881	881	845.3

Figures

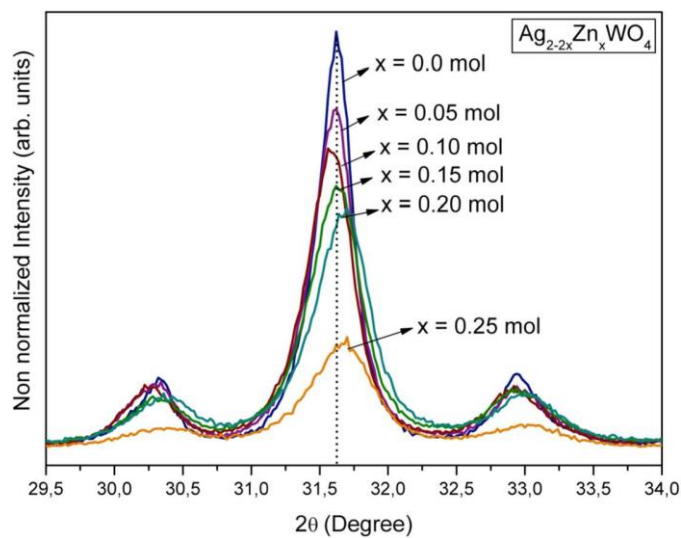


Figure SI-1. Magnification of region between $2\theta = 29.5^\circ$ to 34° .

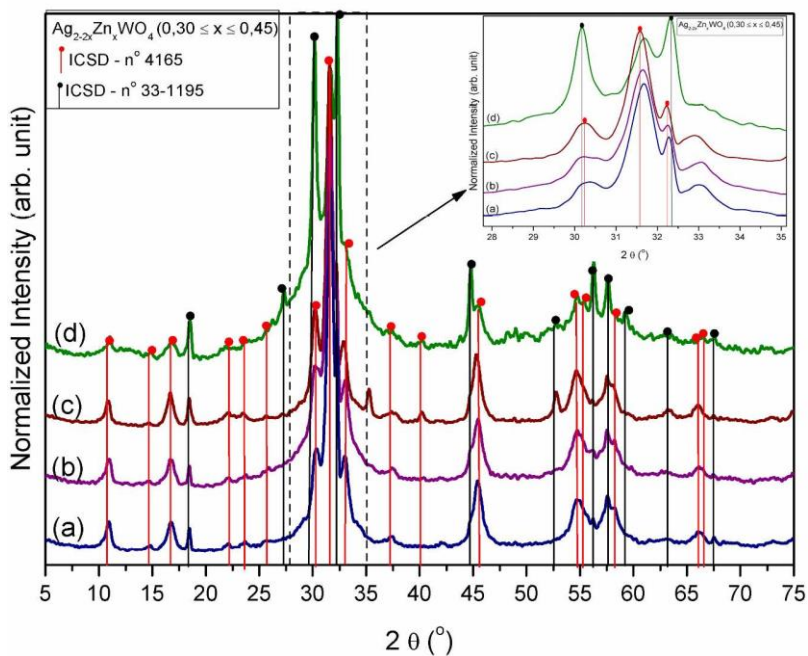


Figure SI-2. XRD of $\alpha\text{-Ag}_{2-2x}\text{Zn}_x\text{WO}_4$ where: (a) 0.30 (b) 0.35 (c) 0.40 and (d) 0.45 microcrystals, obtained by CP method at 80°C for 30 min.

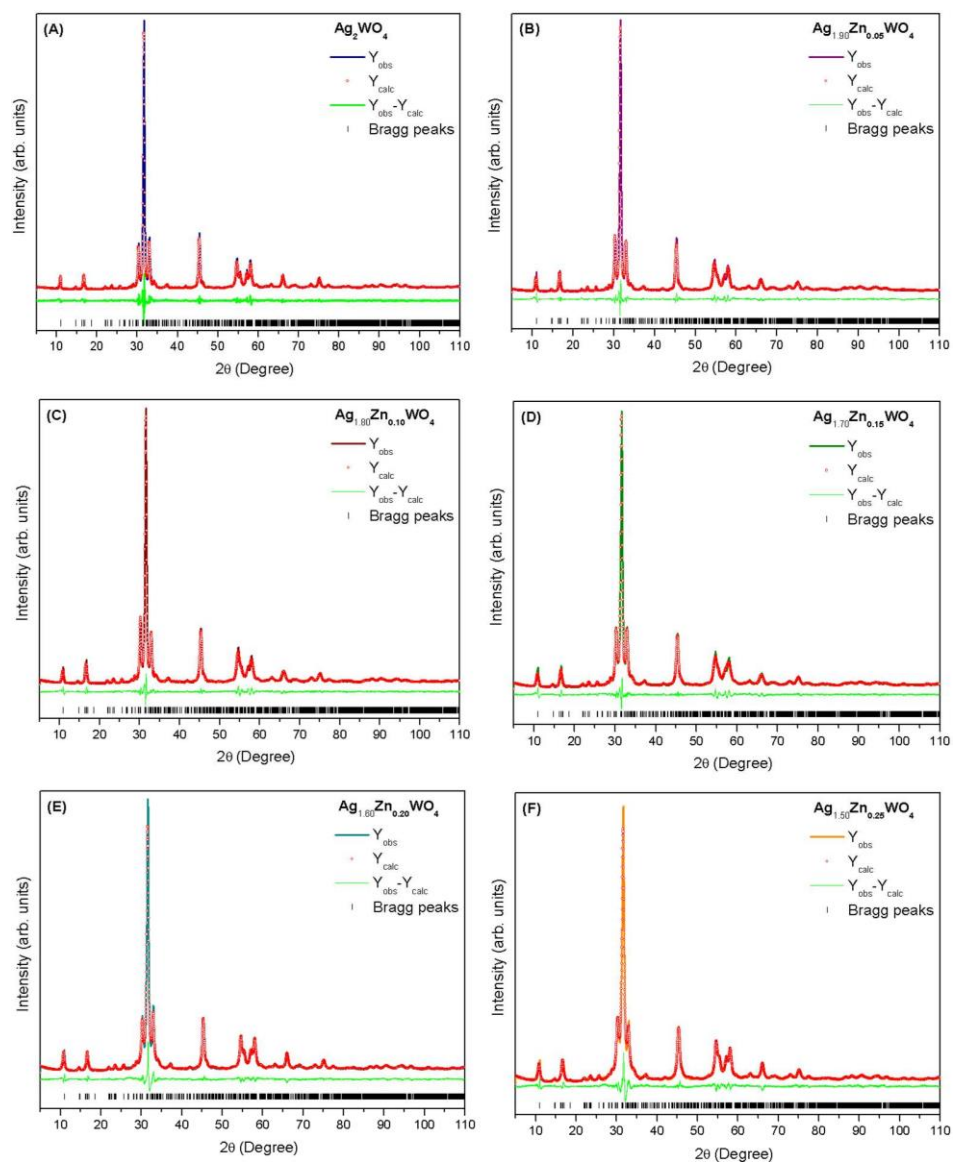


Figure SI-3. Rietveld refinement plot for α - $\text{Ag}_{2-2x}\text{Zn}_x\text{WO}_4$ synthesized by the CP method at 80 °C for 30 min: (a) $x = 0$, (b) $x = 0.05$, (c) $x = 0.10$, (d) $x = 0.15$, (e) $x = 0.20$, and (f) $x = 0.25$

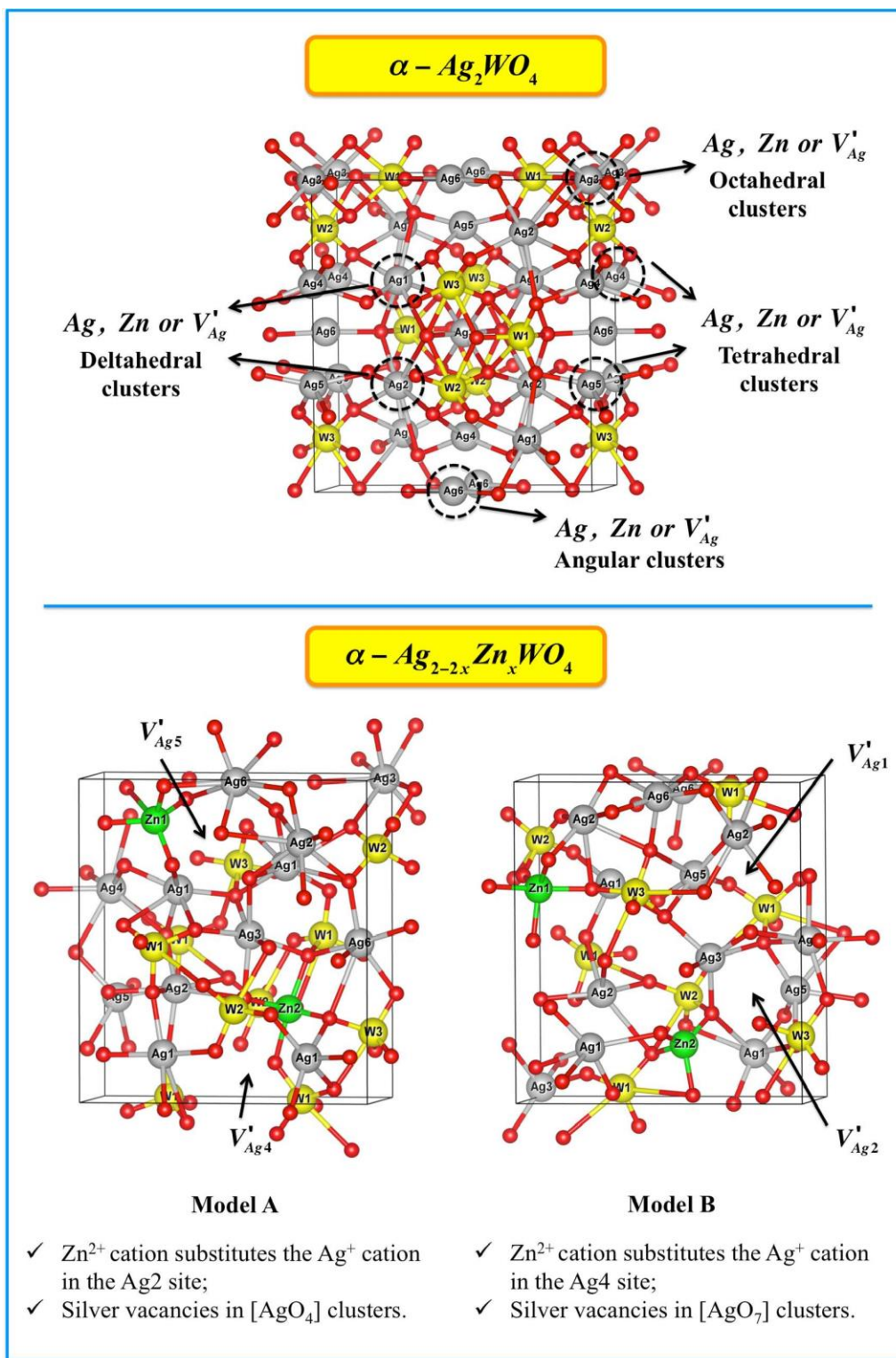


Figure SI-4. Theoretical models of $\alpha - Ag_{2-2x}Zn_xWO_4$ with 25 % of Zn^{2+} .

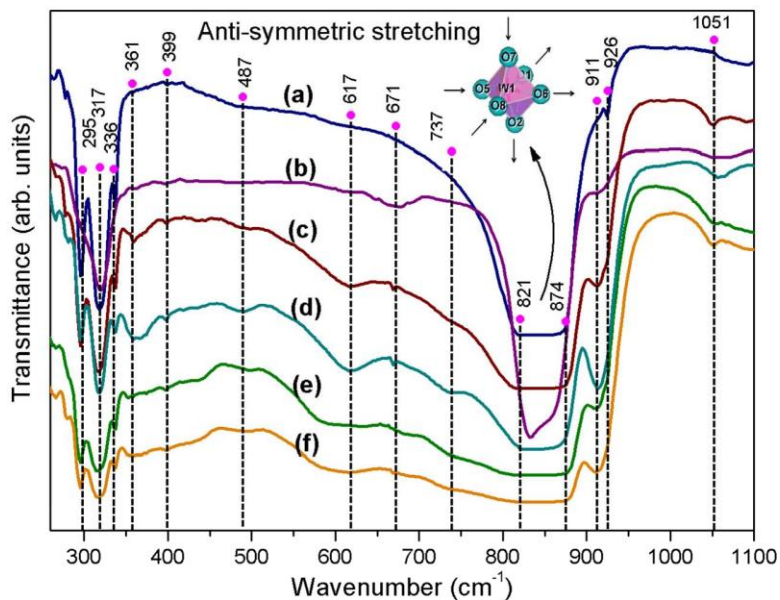


Figure SI-5. FT-IR spectra of the $\alpha\text{-Ag}_{2-2x}\text{Zn}_x\text{WO}_4$ ($x =$ (a) 0, (b) 0.05, (c) 0.10, (d) 0.15, (e) 0.20 and (f) 0.25) microcrystals obtained by the CP method at 80 °C for 30 min.

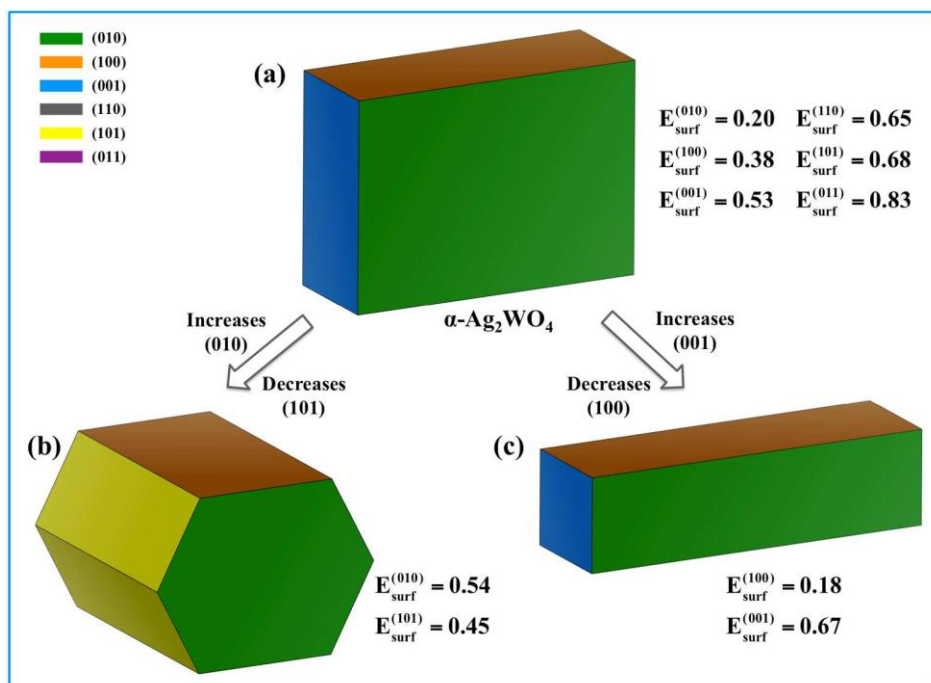


Figure SI-6. Map of morphologies of $\alpha\text{-Ag}_2\text{WO}_4$ with (010), (100), (001) (110), (101), and (011) surfaces. Surface energy is expressed in J m^{-2} .

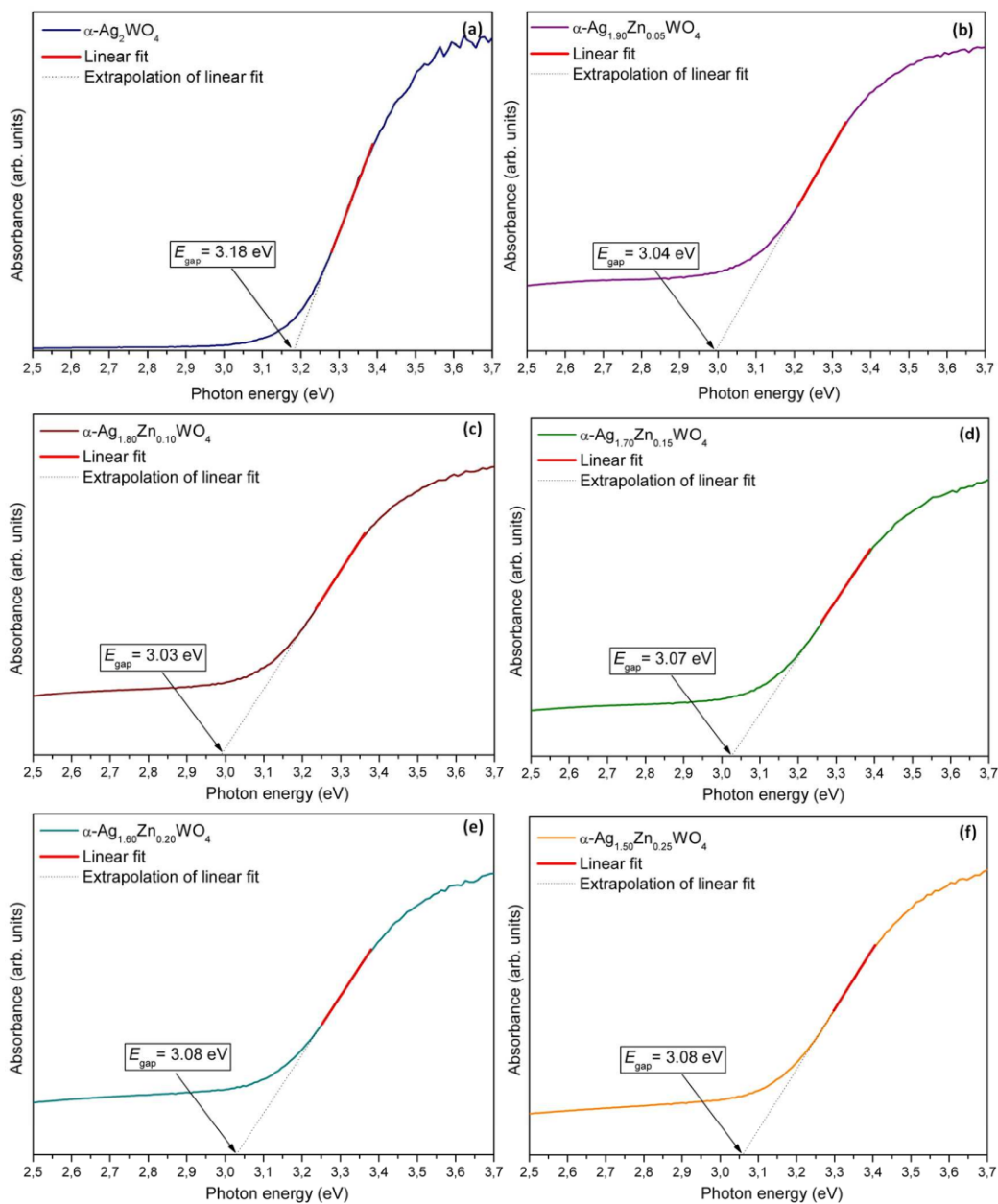


Figure SI-7. UV-Vis spectra for $\alpha\text{-Ag}_{2-2x}\text{Zn}_x\text{WO}_4$ synthesized by the CP method at 80 °C for 30 min: (a) $x = 0$, (b) $x = 0.05$, (c) $x = 0.10$, (d) $x = 0.15$, (e) $x = 0.20$, and (f) $x = 0.25$

References

- (1) da Silva, L. F.; Catto, A. C.; Avansi, W.; Cavalcante, L. S.; Mastelaro, V. R.; Andres, J.; Aguir, K.; Longo, E. Acetone gas sensor based on alpha-Ag₂WO₄ nanorods obtained via a microwave-assisted hydrothermal route. *J. Alloys Compd.* 2016, 683, 186–190.
- (2) Amouzegar, Z.; Naghizadeh, R.; Rezaie, H. R.; Ghahari, M.; Aminzare, M. Cubic ZnWO₄ nano-photocatalysts synthesized by the microwave-assisted precipitation technique. *Ceram. Int.* 2015, 41, 1743–1747.
- (3) Cavalcante, L. S.; Almeida, M. A.; Avansi, W., Jr.; Tranquilin, R. L.; Longo, E.; Batista, N. C.; Mastelaro, V. R.; Li, M. S. Cluster coordination and photoluminescence properties of alpha-Ag₂WO₄ microcrystals. *Inorg. Chem.* 2012, 51, 10675–87.
- (4) Chen, H.; Xu, Y. Photoactivity and stability of Ag₂WO₄ for organic degradation in aqueous suspensions. *Appl. Surf. Sci.* 2014, 319, 319–323.
- (5) Longo, V. M.; De Foggi, C. C.; Ferrer, M. M.; Gouveia, A. F.; Andre, R. S.; Avansi, W.; Vergani, C. E.; Machado, A. L.; Andres, J.; Cavalcante, L. S.; Hernandez, A. C.; Longo, E. Potentiated Electron Transference in alpha-Ag₂WO₄ Microcrystals with Ag Nanofilaments as Microbial Agent. *J. Phys. Chem. A* 2014, 118, 5769–5778.
- (6) Bian, T.; Shang, L.; Yu, H. J.; Perez, M. T.; Wu, L. Z.; Tung, C. H.; Nie, Z. H.; Tang, Z. Y.; Zhang, T. R. Spontaneous Organization of Inorganic Nanoparticles into Nanovesicles Triggered by UV Light. *Adv. Mater.* 2014, 26, 5613–5618.
- (7) Niu, L. Y.; Li, Z. P.; Xu, Y.; Sun, J. F.; Hong, W.; Liu, X. H.; Wang, J. Q.; Yang, S. R. Simple Synthesis of Amorphous NiWO₄ Nanostructure and Its Application as a Novel Cathode Material for Asymmetric Supercapacitors. *ACS Appl. Mater. Interfaces* 2013, 5, 8044–8052.
- (8) Pourmortazavi, S. M.; Rahimi-Nasrabadi, M.; KhalilianShalamzari, M.; Zahedi, M. M.; Hajimirsadeghi, S. S.; Omrani, I. Synthesis, structure characterization and catalytic activity of nickel tungstate nanoparticles. *Appl. Surf. Sci.* 2012, 263, 745–752.
- (9) Shang, L.; Zhou, C.; Bian, T.; Yu, H. J.; Wu, L. Z.; Tung, C. H.; Zhang, T. R. Facile synthesis of hierarchical ZnIn₂S₄ submicrospheres composed of ultrathin mesoporous nanosheets as a highly efficient visible-light-driven photocatalyst for H₂ production. *J. Mater. Chem. A* 2013, 1, 4552–4558.
- (10) Wei, H. G.; Ding, D. W.; Yan, X. R.; Guo, J.; Shao, L.; Chen, H. R.; Sun, L. Y.; Colorado, H. A.; Wei, S. Y.; Guo, Z. H. Tungsten Trioxide/Zinc Tungstate Bilayers:

Electrochromic Behaviors, Energy Storage and Electron Transfer. *Electrochim. Acta* 2014, 132, 58–66.

(11) Yourey, J. E.; Pyper, K. J.; Kurtz, J. B.; Bartlett, B. M. Chemical Stability of CuWO_4 for Photoelectrochemical Water Oxidation. *J. Phys. Chem. C* 2013, 117, 8708–8718.

(12) Zhang, D. H.; Zhou, C.; Sun, Z. H.; Wu, L. Z.; Tung, C. H.; Zhang, T. R. Magnetically recyclable nanocatalysts (MRNCs): a versatile integration of high catalytic activity and facile recovery. *Nanoscale* 2012, 4, 6244–6255.

(13) Ramezani, M.; Pourmortazavi, S. M.; Sadeghpur, M.; Yazdani, A.; Kohsari, I. Silver tungstate nanostructures: electrochemical synthesis and its statistical optimization. *J. Mater. Sci.: Mater. Electron.* 2015, 26, 3861–3867.

(14) Dutta, D. P.; Singh, A.; Ballal, A.; Tyagi, A. K. High Adsorption Capacity for Cationic Dye Removal and Antibacterial Properties of Sonochemically Synthesized Ag_2WO_4 Nanorods. *Eur. J. Inorg. Chem.* 2014, 2014, 5724–5732.

(15) Wang, Q. P.; Guo, X. X.; Wu, W. H.; Liu, S. X. Preparation of Fine Ag_2WO_4 Antibacterial Powders and Its Application in the Sanitary Ceramics. *Adv. Mater. Res.* 2011, 284-286, 1321–1325.

(16) De Santana, Y. V. B.; Gomes, J. E. C.; Matos, L.; Cruvinel, G. H.; Perrin, A.; Perrin, C.; Andres, J.; Varela, J. A.; Longo, E. Silver Molybdate and Silver Tungstate Nanocomposites with Enhanced Photoluminescence. *Nanomater. Nanotechnol.* 2014, 4, 22.

(17) Roca, R. A.; Sczancoski, J. C.; Nogueira, I. C.; Fabbro, M. T.; Alves, H. C.; Gracia, L.; Santos, L. P. S.; de Sousa, C. P.; Andres, J.; Luz, G. E., Jr.; Longo, E.; Cavalcante, L. S. Facet-dependent photocatalytic and antibacterial properties of alpha- Ag_2WO_4 crystals: combining experimental data and theoretical insights. *Catal. Sci. Technol.* 2015, 5, 4091–4107.

(18) Zhang, R.; Cui, H.; Yang, X.; Liu, H.; Tang, H.; Li, Y. Facile hydrothermal synthesis and photocatalytic activity of rod-like nanosized silver tungstate. *Micro Nano Lett.* 2012, 7, 1285–1288.

(19) da Silva, L. F.; Catto, A. C.; Avansi, W., Jr.; Cavalcante, L. S.; Andres, J.; Aguir, K.; Mastelaro, V. R.; Longo, E. A novel ozone gas sensor based on one-dimensional (1D) alpha- Ag_2WO_4 nanostructures. *Nanoscale* 2014, 6, 4058–4062.

(20) Longo, E.; Cavalcante, L. S.; Volanti, D. P.; Gouveia, A. F.; Longo, V. M.; Varela, J. A.; Orlandi, M. O.; Andres, J. Direct in situ observation of the electron-driven synthesis of Ag filaments on alpha- Ag_2WO_4 crystals. *Sci. Rep.* 2013, 3, 1676.

- (21) Cui, X. J.; Yu, S. H.; Li, L. L.; Biao, L.; Li, H. B.; Mo, M. S.; Liu, X. M. Selective synthesis and characterization of single-crystal silver molybdate/tungstate nanowires by a hydrothermal process. *Chem. Eur. J.* 2004, 10, 218–223.
- (22) Sreedevi, A.; Priyanka, K. P.; Babitha, K. K.; Aloysius Sabu, N.; Anu, T. S.; Varghese, T. Chemical synthesis, structural characterization and optical properties of nanophase α -Ag₂WO₄. *Indian J. Phys.* 2015, 89, 889–897.
- (23) Pinatti, I. M.; Nogueira, I. C.; Pereira, W. S.; Pereira, P. F. S.; Gonçalves, R. F.; Varela, J. A.; Longo, E.; Rosa, I. L. V. Structural and Photoluminescence Properties of Eu³⁺ Doped α -Ag₂WO₄ Synthesized by the Green Coprecipitation Methodology. *Dalton Trans.* 2015, 44, 17673–17685.
- (24) Vafaezadeh, M.; Hashemi, M. M. One pot oxidative cleavage of cyclohexene to adipic acid using silver tungstate nano-rods in a Bronsted acidic ionic liquid. *RSC Adv.* 2015, 5, 31298–31302.
- (25) Pan, L.; Li, L.; Chen, Y. Synthesis and electrocatalytic properties of micro-sized Ag₂WO₄ and nanoscaled MWO₄ (M = Co, Mn). *J. SolGel Sci. Technol.* 2013, 66, 330–336.
- (26) Li, J.; Yu, C.; Zheng, C.; Etogo, A.; Xie, Y.; Zhong, Y.; Hu, Y. Facile formation of Ag₂WO₄/AgX (X= Cl, Br, I) hybrid nanorods with enhanced visible-light-driven photoelectrochemical properties. *Mater. Res. Bull.* 2015, 61, 315–320.
- (27) Wang, X.; Fu, C.; Wang, P.; Yu, H.; Yu, J. Hierarchically porous metastable beta-Ag₂WO₄ hollow nanospheres: controlled synthesis and high photocatalytic activity. *Nanotechnology* 2013, 24, 165602.
- (28) Pereira, W. d. S.; Andres, J.; Gracia, L.; San-Miguel, M. A.; da Silva, E. Z.; Longo, E.; Longo, V. M. Elucidating the real-time Ag nanoparticle growth on alpha-Ag₂WO₄ during electron beam irradiation: experimental evidence and theoretical insights. *Phys. Chem. Chem. Phys.* 2015, 17, 5352–5359.
- (29) George, T.; Joseph, S.; Mathew, S. Synthesis and characterization of nanophased silver tungstate. *Pramana* 2005, 65, 793–799.
- (30) Zhu, J.; Fan, H.; Sun, J.; Ai, S. Anion-exchange precipitation synthesis of α -Ag₂WO₄/Zn–Cr layered double hydroxides composite with enhanced visible-light-driven photocatalytic activity. *Sep. Purif. Technol.* 2013, 120, 134–140.
- (31) Ng, C. H. B.; Fan, W. Y. Preparation of highly uniform 1dimensional alpha-Ag₂WO₄ nanostructures with controllable aspect ratio and study of the growth mechanism. *CrystEngComm* 2016, 18, 8010–8019.
- (32) Song, Q.-W.; Yu, B.; Li, X.-D.; Ma, R.; Diao, Z.-F.; Li, R.-G.; Li, W.; He, L.-N.

Efficient chemical fixation of CO₂ promoted by a bifunctional Ag₂WO₄/Ph₃P system. *Green Chem.* 2014, 16, 1633.

(33) Guo, C.-X.; Yu, B.; Xie, J.-N.; He, L.-N. Silver tungstate: a single-component bifunctional catalyst for carboxylation of terminal alkynes with CO₂ in ambient conditions. *Green Chem.* 2015, 17, 474–479.

(34) Lin, Z.; Li, J.; Zheng, Z.; Yan, J.; Liu, P.; Wang, C.; Yang, G. Electronic Reconstruction of alpha-Ag₂WO₄ Nanorods for VisibleLight Photocatalysis. *ACS Nano* 2015, 9, 7256–7265.

(35) Cheng, L.; Shao, Q.; Shao, M.; Wei, X.; Wu, Z. Photoswitches of One-Dimensional Ag₂MO₄ (M = Cr, Mo, and W). *J. Phys. Chem. C* 2009, 113, 1764–1768.

(36) Hallaoui, A.; Taoufyq, A.; Arab, M.; Bakiz, B.; Benhachemi, A.; Bazzi, L.; Villain, S.; Valmalette, J. C.; Guinneton, F.; Gavarri, J. R. Influence of chemical substitution on the photoluminescence of Sr_(1-x)Pb_xWO₄ solid solution. *J. Solid State Chem.* 2015, 227, 186–195.

(37) Culver, S. P.; Greaney, M. J.; Tinoco, A.; Brutchey, R. L. Lowtemperature synthesis of homogeneous solid solutions of scheelitestructured Ca_{1-x}Sr_xWO₄ and Sr_{1-x}Ba_xWO₄ nanocrystals. *Dalton Trans.* 2015, 44, 15042–15048.

(38) Priya, A.; Sinha, E.; Rout, S. K. Structural, optical and microwave dielectric properties of Ba_{1-x}Sr_xWO₄ ceramics prepared by solid state reaction route. *Solid State Sci.* 2013, 20, 40–45.

(39) Porto, S. L.; Longo, E.; Pizani, P. S.; Boschi, T. M.; Simoes, L. G. P.; Lima, S. J. G.; Ferreira, J. M.; Soledade, L. E. B.; Espinoza, J. W. M.; Cassia-Santos, M. R.; Maurera, M.; Paskocimas, C. A.; Santos, I. M. G.; Souza, A. G. Photoluminescence in the CaXSr_{1-x}WO₄ system at room temperature. *J. Solid State Chem.* 2008, 181, 1876–1881.

(40) Taoufyq, A.; Mauroy, V.; Guinneton, F.; Bakiz, B.; Villain, S.; Hallaoui, A.; Benhachemi, A.; Nolibe, G.; Lyoussi, A.; Gavarri, J. R. Role of the chemical substitution on the luminescence properties of solid solutions Ca_(1-x)Cd_(x)WO₄ (0 ≤ x ≤ 1). *Mater. Res. Bull.* 2015, 70, 40–46.

(41) Huang, H. W.; Liu, L. Y.; Tian, N.; Zhang, Y. H. Structure, optical properties, and magnetism of Zn_{1-x}Ni_xWO₄ (0 ≤ x ≤ 1) solid solution. *J. Alloys Compd.* 2015, 637, 471–475.

(42) Patureau, P.; Josse, M.; Dessapt, R.; Mevellec, J. Y.; Porcher, F.; Maglione, M.; Deniard, P.; Payen, C. Incorporation of Jahn-Teller Cu²⁺ Ions into Magnetoelectric Multiferroic MnWO₄: Structural, Magnetic, and Dielectric Permittivity Properties of

Mn_{1-x}Cu_xWO₄ ($x \leq 0.25$). *Inorg. Chem.* 2015, 54, 10623–10631.

(43) Zhang, J. F.; Pan, J. G.; Yin, J.; Wang, J.; Pan, J. G.; Chen, H. B.; Mao, R. H. Structural investigation and scintillation properties of Cd_{1-x}Zn_xWO₄ solid solution single crystals. *CrystEngComm* 2015, 17, 3503–3508.

(44) Siritanon, T.; Jiamprasertboon, A.; Yong, N. Structure and optical properties of Ni_{1-x}CoxWO₄ solid solutions. *Mater. Lett.* 2015, 145, 316–320.

(45) Yourey, J. E.; Kurtz, J. B.; Bartlett, B. M. Structure, Optical Properties, and Magnetism of the Full Zn_{1-x}Cu_xWO₄ ($0 \leq x \leq 1$) Composition Range. *Inorg. Chem.* 2012, 51, 10394–10401.

(46) Han, S. L.; Xiao, K.; Liu, L. Y.; Huang, H. W. Zn_{1-x}CoxWO₄ ($0 \leq x \leq 1$) full range solid solution: Structure, optical properties, and magnetism. *Mater. Res. Bull.* 2016, 74, 436–440.

(47) Pereira, W. d. S.; Ferrer, M. M.; Botelho, G.; Gracia, L.; Nogueira, I. C.; Pinatti, I. M.; Rosa, I. L. V.; La Porta, F. d. A.; Andrés, J.; Longo, E. Effects of chemical substitution on the structural and optical properties of α -Ag_{2-2x}Ni_xWO₄ ($0 \leq x \leq 0.08$) solid solutions. *Phys. Chem. Chem. Phys.* 2016, 18, 21966–21975.

(48) Andres, J.; Gracia, L.; Gonzalez-Navarrete, P.; Longo, V. M.; Avansi, W., Jr.; Volanti, D. P.; Ferrer, M. M.; Lemos, P. S.; La Porta, F. A.; Hernandez, A. C.; Longo, E. Structural and electronic analysis of the atomic scale nucleation of Ag on α -Ag₂WO₄ induced by electron irradiation. *Sci. Rep.* 2015, 4, 5391.

(49) Schofield, P. F.; Knight, K. S.; Cressey, G. Neutron powder diffraction study of the scintillator material ZnWO₄. *J. Mater. Sci.* 1996, 31, 2873–2877.

(50) Dovesi, R.; Saunders, V. R.; Roetti, C.; Orlando, R.; ZicovichWilson, C. M.; Pascale, F.; Civalieri, B.; Doll, K.; Harrison, N. M.; Bush, I. J.; D'Arco, P.; Llunel, M.; Causà, M.; Noël, Y. *CRYSTAL14 User's Manual*; Theoretical Chemistry Group: University of Turin: Italy, 2014.

(51) Becke, A. D. Density-Functional Thermochemistry 0.3. The Role of Exact Exchange. *J. Chem. Phys.* 1993, 98, 5648–5652.

(52) Lee, C. T.; Yang, W. T.; Parr, R. G. Development of the ColleSalvetti Correlation-Energy Formula into a Functional of the ElectronDensity. *Phys. Rev. B: Condens. Matter Mater. Phys.* 1988, 37, 785–789.

(53) Crystal, Basis Sets Library. <http://www.crystal.unito.it/basissets.php>.

(54) Andrés, J.; Gracia, L.; Gouveia, A. F.; Ferrer, M. M.; Longo, E. Effects of surface stability on the morphological transformation of metals and metal oxides as investigated by first-principles calculations. *Nanotechnology* 2015, 26,

405703–405713.

(55) Skarstad, P. M.; Geller, S. W4016)8- Polyion in the high temperature modification of silver tungstate. *Mater. Res. Bull.* 1975, 10, 791–800.

(56) Turkovic, A.; Fox, D. L.; Scott, J. F.; Geller, S.; Ruse, G. F. High temperature raman spectroscopy of silver tetratungstate, Ag₈W₄O₁₆. *Mater. Res. Bull.* 1977, 12, 189–196.

(57) Gouveia, A. F.; Sczancoski, J. C.; Ferrer, M. M.; Lima, A. S.; Santos, M. R.; Li, M. S.; Santos, R. S.; Longo, E.; Cavalcante, L. S. Experimental and theoretical investigations of electronic structure and photoluminescence properties of beta-Ag₂MoO₄ microcrystals. *Inorg. Chem.* 2014, 53, 5589–99.

(58) Larson, A. C.; Von Dreele, R. B. GSAS. *Gem. Struc. Anal. Syst.* 2004, 1–224.

(59) Rietveld, H. M. A profile refinement method for nuclear and magnetic structures. *J. Appl. Crystallogr.* 1969, 2, 65–71.

(60) Thompson, P.; Cox, D. E.; Hastings, J. B. Rietveld Refinement of Debye-Scherrer Synchrotron X-ray Data from Al₂O₃. *J. Appl. Crystallogr.* 1987, 20, 79–83.

(61) Finger, L. W.; Cox, D. E.; Jephcoat, A. P. A correction for powder diffraction peak asymmetry due to axial divergence. *J. Appl. Crystallogr.* 1994, 27, 892–900.

(62) Stephens, P. W. Phenomenological model of anisotropic peak broadening in powder diffraction. *J. Appl. Crystallogr.* 1999, 32, 281–289.

(63) Momma, K.; Izumi, F. VESTA 3 for three-dimensional visualization of crystal, volumetric and morphology data. *J. Appl. Crystallogr.* 2011, 44, 1272–1276.

(64) Cavalcante, L. S.; Sczancoski, J. C.; Espinosa, J. W. M.; Varela, J. A.; Pizani, P. S.; Longo, E. Photoluminescent behavior of BaWO₄ powders processed in microwave-hydrothermal. *J. Alloys Compd.* 2009, 474, 195–200.

(65) Guo, C.; Chen, T.; Luan, L.; Zhang, W.; Huang, D. Luminescent properties of R₂(MoO₄)₃:Eu³⁺ (R = La, Y, Gd) phosphors prepared by sol-gel process. *J. Phys. Chem. Solids* 2008, 69, 1905–1911.

(66) Cavalcante, L. S.; Sczancoski, J. C.; Albarici, V. C.; Matos, J. M. E.; Varela, J. A.; Longo, E. Synthesis, characterization, structural refinement and optical absorption behavior of PbWO₄ powders. *Mater. Sci. Eng., B* 2008, 150, 18–25.

(67) Pereira, P. F. S.; de Moura, A. P.; Nogueira, I. C.; Lima, M. V. S.; Longo, E.; de Sousa Filho, P. C.; Serra, O. A.; Nassar, E. J.; Rosa, I. L. V. Study of the annealing temperature effect on the structural and luminescent properties of SrWO₄:Eu phosphors prepared by a nonhydrolytic sol-gel process. *J. Alloys Compd.* 2012, 526, 11–21.

- (68) Longo, E.; Volanti, D. P.; Longo, V. M.; Gracia, L.; Nogueira, I. C.; Almeida, M. A. P.; Pinheiro, A. N.; Ferrer, M. M.; Cavalcante, L. S.; Andres, J. Toward an Understanding of the Growth of Ag Filaments on α -Ag₂WO₄ and Their Photoluminescent Properties: A Combined Experimental and Theoretical Study. *J. Phys. Chem. C* 2014, 118, 1229–1239.
- (69) Sczancoski, J. C.; Cavalcante, L. S.; Joya, M. R.; Espinosa, J. W.; Pizani, P. S.; Varela, J. A.; Longo, E. Synthesis, growth process and photoluminescence properties of SrWO₄ powders. *J. Colloid Interface Sci.* 2009, 330, 227–36.
- (70) Keereeta, Y.; Thongtem, S.; Thongtem, T. Enhanced photocatalytic degradation of methylene blue by WO₃/ZnWO₄ composites synthesized by a combination of microwave-solvothermal method and incipient wetness procedure. *Powder Technol.* 2015, 284, 85–94.
- (71) Gouveia, A. F.; Ferrer, M. M.; Sambrano, J. R.; Andres, J.; Longo, E. Modeling the atomic-scale structure, stability, and morphological transformations in the tetragonal phase of LaVO₄. *Chem. Phys. Lett.* 2016, 660, 87–92.
- (72) Ferrer, M. M.; Gouveia, A. F.; Gracia, L.; Longo, E.; Andres, J. A 3D platform for the morphology modulation of materials: First principles calculations on the thermodynamic stability and surface structure of metal oxides: Co₃O₄, α -Fe₂O₃, and In₂O₃. *Modell. Simul. Mater. Sci. Eng.* 2016, 24, 025007–025016.
- (73) de Sousa Filho, P. C.; Serra, O. A. Liquid phase synthesis methodologies for the obtainment of rare earth-based inorganic nanomaterials. *Quim. Nova* 2015, 38, 679–U259.
- (74) Wood, D. L.; Tauc, J. Weak Absorption Tails in Amorphous Semiconductors. *Phys. Rev. B* 1972, 5, 3144–3151.
- (75) Kubelka, P.; Munk, F. Ein Beitrag Zur Optik Der Farbanstriche. *Zeit. Fur. Technol. Physik* 1931, 12, 593–601.
- (76) Pereira, P. F. S.; Nogueira, I. C.; Longo, E.; Nassar, E. J.; Rosa, I. L. V.; Cavalcante, L. S. Rietveld refinement and optical properties of SrWO₄:Eu³⁺ powders prepared by the non-hydrolytic sol-gel method. *J. Rare Earths* 2015, 33, 113–128.
- (77) Tang, J. W.; Ye, J. H. Correlation of crystal structures and electronic structures and photocatalytic properties of the W-containing oxides. *J. Mater. Chem.* 2005, 15, 4246–4251.
- (78) Kim, D. W.; Cho, I.-S.; Lee, S.; Bae, S.-T.; Shin, S. S.; Han, G. S.; Jung, H. S.; Hong, K. S. Photophysical and Photocatalytic Properties of Ag₂M₂O₇ (M = Mo, W). *J. Am. Ceram. Soc.* 2010, 93, 3867–3872.

4. FINAL CONSIDERATION

According to Ag_3PO_4 and Ag_2WO_4 material characterization data, it is observed that the synthesis method was effective and that the current results allow us to better understand the phenomena of each material, allowing better control for future technological applications.

5. FUTURE PERSPECTIVE

- i. Construct a theoretical model for Ag_3PO_4 irradiated, by means of mechanical calculation in order to facilitate the understanding of the structural deformation effects in the electronic structure and the photoluminescent profile.
- ii. Development of others doping studies of Ag_3PO_4 , replacing the network former rare earth comparing optical, electronic, and structural properties.

GENERAL BIBLIOGRAPHY

- [1] H. Fukuoka, H. Matsunaga and S. Yamanaka, *Materials Research Bulletin*, 2003, 38, 991-1001.
- [2] K. V. Terebilenko, A. A. Kirichok, V. N. Baumer, M. Sereduk, N. S. Slobodyanik and P. Guetlich, *Journal of Solid State Chemistry*, 2010, 183, 1473-1476.
- [3] Y. Onodera, T. Iwasaki, A. Chatterjee, T. Ebina, T. Satoh, T. Suzuki and H. Mimura, *Applied Clay Science*, 2001, 18, 123-134.
- [4] Y. Liu, G. Zhu, J. Yang, A. Yuan and X. Shen, *Plos One*, 2014, 9.
- [5] I. Sadaba, S. Lima, A. A. Valente and M. Lopez Granados, *Carbohydrate Research*, 2011, 346, 2785-2791
- [6] B. V. Kumar and M. Vithal, *Physica B-Condensed Matter*, 2012, 407, 2094-2099.
- [7] G. Botelho, J. C. Sczancoski, J. Andres, L. Gracia and E. Longo, *Journal of Physical Chemistry C*, 2015, 119, 6293-6306.
- [8] M. J. Xu, L. X. Wang, D. Z. Jia, L. Liu, L. Zhang, Z. P. Guo and R. Sheng, *Journal of the American Ceramic Society*, 2013, 96, 1198-1202.
- [9] E. S. Takeuchi, C.-Y. Lee, P.-J. Cheng, M. C. Menard, A. C. Marschilok and K. J. Takeuchi, *Journal of Solid State Chemistry*, 2013, 200, 232-240.
- [10] M. Tamaru, S. C. Chung, D. Shimizu, S.-i. Nishimura and A. Yamada, *Chemistry of Materials*, 2013, 25, 2538-2543.
- [11] T. Sato, M. Saito, C. Sato and S. Yin, *Functional Materials Letters*, 2009, 2, 157-161.
- [12] S. M. Vieira Fontoura, R. C. Beber Vieira, C. Bayer, P. R. Ernani and R. P. de Moraes, *Revista Brasileira De Ciencia Do Solo*, 2010, 34, 1907-1914.
- [13] X. Chen, Y. Dai and X. Wang, *Journal of Alloys and Compounds*, 2015, 649, 910-932.
- [14] Y. Z. MA, F. CHENG, W. S. LIU, J. WANG and Y. WANG, *Transitions Nonferrous Metals Society China*, 2015, 25, 112-121.

- [15] S. Zhang, X. Gu, Y. Zhao and Y. Qiang, *Materials Science and Engineering*, 2015, 201, 57–65
- [16] R. Masse, I. Tordjman and A. Durif, *Kristallogr., Kristallgeom., Kristallphys., Kristallchem*, 1976, 144, 76–81.
- [17] X. Ma, B. Lu, D. Li, R. Shi, C. Pan and Y. Zhu, *Journal of Physical Chemistry C*, 2011, 115(11), 4680–4687.
- [18] MASSE R, TORDJMAN I, DURIF A. *Zeitschrift für Kristallographie*, 1976, 144(1–6), 76–81.
- [19] NG H, CALVO C, FAGGIANI R, *Acta Crystallographica Section B: Structural Crystallography and Crystal Chemistry*, 1978, 34(3), 898–899..
- [20] C. Dong, K.-L. Wu, M.-R. Li, L. Liu and X.-W. Wei, *Catalysis Communications*, 2014, 46, 32-35.
- [21] J. Li, Z. Guo, Z. Liu, M. Cui and Z. Zhu, *Physica Status Solidi a-Applications and Materials Science*, 2215, 212, 459-466.
- [22] C. Piccirillo, R. A. Pinto, D. M. Tobaldi, R. C. Pullar, J. A. Labrincha, M. M. E. Pintado and P. M. L. Castro, *Journal of Photochemistry and Photobiology a-Chemistry*, 2015, 296, 40-47.
- [23] J. Wan, E. Liu, J. Fan, X. Hu, L. Sun, C. Tang, Y. Yin, H. Li and Y. Hu, *Ceramics International*, 2015, 41, 6933-6940.
- [24] Y. Yan, H. Guan, S. Liu and R. Jiang, *Ceramics International*, 2014, 40, 9095-9100.
- [25] 26. Amornpitoksuk, P. and Suwanboon, S., *Advanced Powder Technology*, 2014, 25, 1026-1030
- [26] Bi, Y. S. Ouyang, J. Cao and J. Ye, *Physical Chemistry Chemical Physics*, 2011, 13, 10071-10075.
- [27] He, Y.; Zhang, L.; Teng, B. and Fan, M., *Environmental Science & Technology*, 2015, 49, 649-656.
- [28] Cao-Thang, D.; Thanh-Dinh, N.; Kleitz, F.; Trong-On, D., *Chem. Commun.* 2011, 47, 7797-7799.
- [29] Wu, A.; Tian, C.; Chang, W.; Hong, Y.; Zhang, Q.; Qu, Y.; Fu, H., *Mater. Res. Bull.* 2013, 48, 3043-3048.
- [30] Liu, J.-K.; Luo, C.-X.; Wang, J.-D.; Yang, X.-H.; Zhong, X.-H., *Crystengcomm* 2012, 14, 8714-8721.
- [31] Que, R., *Front. Optoelectron.* 2011, 4, 176-180
- [32] Trench, A.B.; Machado, T. R.; Gouveia, A. F.; Assis, M.; Trindade, L. G.; Santos, C.; Perrin, A.; Perrin, C.; Oliva, M.; Andrés, J.; Longo, E. *Applied Catalysis B-Environmental*, v. 238, p. 198-211, 2018.
- [33] Andres, J., Gracia, L., Gonzalez-Navarrete, P., Longo, V. M., Avansi, W., Jr., Volanti, D. P., Ferrer, M. M., Lemos, P. S., La Porta, F. A., Hernandez, A. C., Longo, E. *Scientific reports*, 4: 2014.
- [34] You, B. S. H., Liu, B., Mo, M. S., Huang, J. H., Liu, X. M., Qian, Y. T. *Advanced Functional Materials*, 2003 (8): 2003.
- [35] Longo, V. M., De Foggi, C. C., Ferrer, M. M., Gouveia, A. F., Andre, R. S., Avansi, W., Vergani, C. E., Machado, A. L., Andres, J., Cavalcante, L. S., Hernandez, A. C., Longo, E. *The journal of physical chemistry. A*, 118 (31): 2014.
- [36] SREEDEVI, A., PRIYANKA, K. P., BABITHA, K. K., ALOYSIUS SABU, N., ANU, T. S., VARGHESE, T. "Chemical synthesis, structural characterization and optical properties of nanophase α -Ag₂WO₄". *Indian Journal of Physics*, 89 (9): 2015.
- [37] ROCA, R. A., SCZANCOSKI, J. C., NOGUEIRA, I. C., FABBRO, M. T., ALVES, H. C., GRACIA, L., SANTOS, L. P. S., DE SOUSA, C. P., ANDRÉS, J., LUZ, G. E., LONGO, E., CAVALCANTE, L. S. "Facet-dependent photocatalytic and antibacterial properties of α -Ag₂WO₄ crystals: combining experimental data and theoretical

- insights". *Catal. Sci. Technol.*, 5 (8): 2015.
- [38] LIN, Z., LI, J., ZHENG, Z., YAN, J., LIU, P., WANG, C., YANG, G. "Electronic Reconstruction of \square -Ag₂WO₄ Nanorods for Visible-Light Photocatalysis". *ACS NANO*, 9 (7): 2015.
- [39] M. Assis, E. Cordoncillo, R. Torres-Mendieta, H. Beltrán-Mir, G. Mínguez-Vega, R.C. Oliveira, E.R. Leite, C.C. Foggi, C.E. Vergani, E. Longo, J. Andrés, *Sci Rep.* 2018, 8, 1.
- [40] V. M. Longo, C. C. De Foggi, M. M. Ferrer, A. F. Gouveia, R. S. André, W. Avansi, C. E. Vergani, A. L. Machado, J. Andrés, L. S. Cavalcante, A. C. Hernandez, E. Longo, *J. Phys. Chem. A.* 2014, 118, 5769.
- [41] CAVALCANTE, L. S., ALMEIDA, M. A., AVANSI, W., JR., TRANQUILIN, R. L., LONGO, E., BATISTA, N. C., MASTELARO, V. R., LI, M. S. "Cluster coordination and photoluminescence properties of \square -Ag₂WO₄ microcrystals". *Inorganic chemistry*, 51 (20): 2012.

